

Biomimetics in micro- and nano-photonics

Structural and material aspects

Dissertation

Marie-Christin Heep

Vom Fachbereich Physik der Technischen Universität Kaiserslautern zur
Verleihung des akademischen Grades „Doktor der Naturwissenschaften“
genehmigte Dissertation

Betreuer: Prof. Dr. Georg von Freymann
Zweitgutachter: Prof. Dr. Cordt Zollfrank

Datum der wissenschaftlichen Aussprache:
8.09.2021

D 386

Abstract

There are a lot of photonic micro- and nano-structures in nature that consist of materials with a low refractive index and that can keep up with artificial structures concerning optical properties like scattering or coloration. This work aims to understand the photonic structures in the silver ant *Cataglyphis bombycina*, the blue butterfly of genus *Morpho*, the beetle *Entimus imperialis*, which shows polarization-dependent reflection, and the white beetle *Cyphochilus insulanus*. Furthermore, corresponding micro- and nano-structures are fabricated.

Bioinspired models with the same optical properties as the investigated structures are developed and analyzed using geometric optics and finite-difference time-domain calculations. These models are qualitatively and quantitatively compared regarding their optical properties with the original structures and fabricated by direct laser writing. To mimic potential effects of material-based disorder of the natural photonic structures, a cellulose-based resist for direct laser writing is developed and examined.

Conventional resists in direct laser writing can be replaced by a resist containing cellulose derivatives. Here, different combinations of cellulose derivatives, initiators, and solvents are examined. The best performance is observed for a combination of methacrylated cellulose acetate (MACA500), 2-Isopropyl-9H-thioxanthen-9-one (ITX), and dimethyl sulfoxide (DMSO). These resists allow for a reproducible structuring at affordable laser powers ($\ll 50$ mW). By adjusting the exact composition and the writing parameters, a feature size down to 130 nm and a resolution of the features down to 600 nm in the lateral direction, perpendicular to the beam propagation, and 2.1 μm in the axial direction is attained. The achieved cross-linking enables stable three-dimensional structures and, together with the possible resolution, allows to fabricate the model inspired by the white beetle *Cyphochilus insulanus* in the cellulose-based resist.

The silver appearance of the *Cataglyphis bombycina* can be completely explained with geometric optics in the prism-shaped hairs that cover its body. The more complex structures of the other three insects use photonic crystal-like material arrangements with a varying amount of disorder. The polarization dependence of the *Entimus imperialis* arises from a diamond structure inside the scales of the beetle and can be mimicked with a photonic woodpile crystal. The blue butterfly of the genus *Morpho* and the white beetle *Cyphochilus insulanus* both can be reduced to disordered Bragg stacks, in which the exact properties are achieved by introducing different amounts of disorder. For *Cataglyphis bombycina*,

Abstract

Entimus imperialis, and *Cyphochilus insulanus*, the developed bioinspired models are fabricated using conventional resists in direct laser writing. All models show a qualitative correspondence to the optical properties of the original structures.

The cellulose-based resists enable the use of polysaccharides in direct laser writing and the concepts can be transferred to other polysaccharides, like chitin. The analysis of the different natural photonic structures and the developed bioinspired models reveal a material independence of the structures that allows the fabrication of these models in different transparent materials.

Zusammenfassung

Es gibt verschiedenste Mikro- und Nano-Strukturen in der Natur, die aus Materialien mit niedrigem Brechungsindex bestehen und die in ihren optischen Eigenschaften, wie Streuung oder Farbgebung, mit künstlichen Strukturen vergleichbar sind. Ziel dieser Arbeit ist es, die Strukturen der Silberameise *Cataglyphis bombycina*, des blauen Schmetterlings der Gattung *Morpho*, des Käfers *Entimus imperialis*, der eine polarisationsabhängige Reflexion zeigt, und des weißen Käfers *Cyphochilus insulanus* zu verstehen. Entsprechende bioinspirierte Strukturen sollen hergestellt werden.

Die bioinspirierten Modelle der Strukturen werden entwickelt und mithilfe geometrischer Optik und Finite-Differenzen-Methoden im Zeitbereich analysiert. Die Modelle werden qualitativ und quantitativ in ihren optischen Eigenschaften mit den Originalstrukturen verglichen und mit direktem Laserschreiben hergestellt. Um eventuelle materialbedingte Unordnung der biologischen, photonischen Strukturen nachzuahmen, wird ein neuer cellulosebasierter Lack für das direkte Laserschreiben entwickelt und untersucht.

Die herkömmlichen Lacke für das direkte Laserschreiben lassen sich durch Lacke mit Cellulosederivaten ersetzen. Dabei werden Kombinationen von unterschiedlichen Cellulosederivaten, Photoinitiatoren und Lösungsmitteln untersucht. Die besten Ergebnisse werden mit einer Kombination aus einem methacrylierten Celluloseacetat (MACA500), 2-Isopropyl-9H-thioxanthen-9-one (ITX) und Dimethylsulfoxid (DMSO) erzielt. Diese Kombination erlaubt eine reproduzierbare Strukturierung bei erschwinglichen Laserleistungen ($\ll 50$ mW). Durch eine Anpassung der Mischungsverhältnisse und der Prozessparameter können Strukturgrößen von wenigen Hundert Nanometern (130 nm) und eine Auflösung der verschiedenen Strukturen bis zu 600 nm in lateraler Richtung, senkrecht zum Laserstrahl, und bis 2,1 μm in axialer Richtung erreicht werden. Die erzielte Vernetzung ermöglicht stabile Strukturen und, mit der erreichten Auflösung, auch die Fertigung biomimetischer Strukturmodelle, wie der Modellstruktur, die durch den weißen Käfer *Cyphochilus insulanus* inspiriert ist, in cellulosebasierten Photolacken.

Das silberne Aussehen der *Cataglyphis bombycina* kann vollständig durch geometrische Optik an den prismenförmigen Haaren der Ameise erklärt werden. Die komplizierteren Strukturen der anderen Insekten basieren auf photonischen Kristallen, die ein unterschiedliches Maß an Unordnung aufweisen. Die polarisationsabhängige Reflexion des Käfers *Entimus imperialis* rührt von einer Diamantstruktur im Inneren der Schuppen des Käfers her und kann durch sogenannte photonische Woodpile-Strukturen imitiert werden.

Zusammenfassung

Der blaue Schmetterling der Gattung *Morpho* und der weiße Käfer *Cyphochilus insulanus* basieren beide auf ungeordneten Bragg-Spiegeln. Die exakten Eigenschaften der Strukturen werden dabei allein durch das Maß an Unordnung bestimmt. Für die *Cataglyphis bombycina*, den *Entimus imperialis* und den *Cyphochilus insulanus* werden die bioinspirierten Modellstrukturen in herkömmlichen Photolacken mit direktem Laserschreiben hergestellt. Alle Modellstrukturen entsprechen in ihren optischen Eigenschaften qualitativ den Originalstrukturen.

Die Verwendung cellulosebasierter Lacke stellt den Einzug der Polysaccharide in das direkte Laserschreiben dar und die Ergebnisse lassen sich auf andere Polysaccharide, wie Chitin, übertragen. Die Untersuchung der verschiedenen natürlichen photonischen Strukturen und die entwickelten bioinspirierten Modelle haben eine Materialunabhängigkeit der Strukturen gezeigt, die eine Fertigung der Modelle in verschiedensten transparenten Materialien ermöglicht.

Contents

1	Introduction	1
2	Theoretical background	5
2.1	Nonabsorptive light-matter interaction	6
2.1.1	Interference	7
2.1.2	Refraction	8
2.1.3	Scattering	11
2.2	Periodic and nonperiodic arrangements	13
2.2.1	Photonic crystals	13
2.2.2	Disordered structures	15
2.3	Finite-difference time-domain method	16
2.3.1	Working principle	16
2.3.2	Boundary conditions	18
2.3.3	Advantages and disadvantages of FDTD	19
3	Methods	21
3.1	Structuring biomaterials	21
3.2	Direct Laser Writing	22
3.2.1	Technical realization	23
3.2.2	Physical process	25
3.2.3	Chemical process	27
3.2.4	Optimization	29
4	Direct laser writing in a bioinspired material	31
4.1	Cellulose - a short profile	31
4.2	Components of a bio-resist	33
4.2.1	Cellulose-based monomers	33
4.2.2	Initializing the polymerization	41
4.2.3	Enabling the handling	44
4.3	Properties of cellulose-based resists	46
4.3.1	Polymerization threshold	46
4.3.2	Chemical stability	49
4.3.3	Resolution in 2D and 3D	50
4.3.4	Further properties	53

4.3.5	Summary	54
4.4	Outlook: Bioinspired structures in a bioinspired photoresist	54
5	Investigated biological systems	57
5.1	<i>Cataglyphis bombycina</i> – the silver ant	58
5.1.1	The underlying concept of the hairs of <i>Cataglyphis bombycina</i>	59
5.1.2	Fabrication of prism-shaped hairs with DLW	63
5.2	Genus <i>Morpho</i> – the blue butterflies	66
5.3	<i>Entimus imperialis</i> – polarization effects	68
5.3.1	The underlying concept of the reflection at <i>Entimus imperialis</i>	69
5.3.2	Fabrication of polarization-dependent structures with DLW	72
5.4	<i>Cyphochilus insulanus</i> – the white beetle	74
5.4.1	The underlying concept in the scales of <i>Cyphochilus insulanus</i>	75
5.4.2	Fabrication of white, disordered structures with DLW	79
6	Conclusions	81
A	The operator $\hat{\Theta}$	85
A.1	A linear operator	85
A.2	A Hermitian operator	86
B	Introduction to the notation in crystallography	89
	Publications	105
	Curriculum vitae	107

Formula symbols and abbreviations

List of formula symbols

\vec{x} is the symbol for a vector, while \overleftrightarrow{x} marks a tensor. Single components of a vector are marked with an index that indicates the direction: x_j is the component of \vec{x} along the j direction. Functions of a certain coordinate x which do not need to be specified are marked with $f(x)$. Temporal derivations of a quantity are marked with \dot{f} .

Formula symbol	Unit	Physical quantity
Lowercase letters		
\vec{a}_j with $ \vec{a}_j = a_j$	m	grid vector and grid periodicity in j direction
c_0	$\frac{\text{m}}{\text{s}}$	vacuum speed of light
d	m	size of a particle
d_j	m	thickness of a layer indicated by index
\vec{e}_j		unit vector in j direction
f	Hz	repetition rate
\vec{g}_j with $ \vec{g}_j = g_j$	$\frac{1}{\text{m}}$	reciprocal grid vector and lattice constant in j direction
g		line shape function of a transition
$\hbar = \frac{h}{2\pi}$	Js	Planck constant
\vec{j}	$\frac{\text{A}}{\text{m}^2}$	current density
\vec{k} with $ \vec{k} = \frac{2\pi}{\lambda}$	$\frac{1}{\text{m}}$	wave vector
l_a	m	absorption length
l_s	m	scattering mean free path
l_{tr}	m	transport mean free path
m	kg	mass
$n_j(\nu)$ with $n_j^2 = \epsilon_{rj}\mu_{rj}$		refractive index of a material j
q	C	charge

Formula symbols and abbreviations

Formula symbol	Unit	Physical quantity
r		reflectance coefficient
t	s	time or temporal coordinate
$\vec{u}_k(\vec{x})$		periodic function
$v_{j\text{ph}}(\nu) = \frac{c_0}{n_j(\nu)}$	$\frac{\text{m}}{\text{s}}$	phase velocity of light in a material j
v_w	$\frac{\text{m}}{\text{s}}$	writing speed
$\vec{x} = \begin{pmatrix} x \\ y \\ z \end{pmatrix}$	m	spatial coordinate
Capital letters		
A		amplitude of an oscillation
$\vec{B} = \mu_0(\vec{H} + \vec{M})$	T	magnetic flux density
D	$\frac{\text{W}^2\text{s}}{\text{m}}$	laser dose
$\vec{D} = \epsilon_0\vec{E} + \vec{P}$	$\frac{\text{As}}{\text{m}^2}$	electric displacement
DP		degree of polymerization
DS		degree of substitution
\vec{E}	$\frac{\text{V}}{\text{m}}$	electric field strength
\mathcal{E}	$\frac{\text{V}}{\text{m}}$	scalar amplitudes of the electric field strength
\vec{H}	$\frac{\text{A}}{\text{m}}$	magnetic field strength
\mathcal{H}		Hamilton operator in solid state physics
I	$\frac{\text{W}}{\text{m}^2}$	intensity
\vec{M}	$\frac{\text{A}}{\text{m}}$	magnetization
NA		numerical aperture
P	W	power
P_{th}	W	Schwarzschild threshold
\vec{P}	$\frac{\text{As}}{\text{m}^2}$	polarization
R^2		coefficient of determination
T		transmission
$\overleftrightarrow{T}_{G \rightarrow E}$		transition tensor
$V(\vec{x})$		potential in solid state physics
W	J	energy
Z	Ω	impedance

Formula symbol	Unit	Physical quantity
Greek letters		
$\alpha, \beta, \zeta, \theta, \iota, \phi, \psi$		angles
γ	$\frac{1}{s}$	damping constant
ϵ_0	$\frac{As}{Vm}$	vacuum permittivity
$\overleftrightarrow{\epsilon}_r = 1 + \overleftrightarrow{\chi}$		relative permittivity
$\hat{\Theta}$		operator for photonic crystals
κ	$\frac{kg}{s^2}$	spring constant
$\lambda = \frac{v_{ph}}{\nu}$	m	wavelength
μ_0	$\frac{Vs}{Am}$	vacuum permeability
$\overleftrightarrow{\mu}_r = 1 + \overleftrightarrow{\chi}_m$		relative permeability
ν	Hz	frequency of a electromagnetic wave
ρ	$\frac{C}{m^3}$	charge density
σ_{2PA}	GM	two-photon absorption cross section
τ	s	pulse duration
$\overleftrightarrow{\chi}$		electric susceptibility
$\overleftrightarrow{\chi}_m$		magnetic susceptibility
Ψ		electron wave function in solid state physics
$\omega = 2\pi\nu$	$\frac{1}{s}$	angular frequency

List of abbreviations

Abbreviation	Explanation
1D	one-dimensional
2D	two-dimensional
3D	three-dimensional
1PA	one-photon absorption
2PA	two-photon absorption
A	acetate group
ABC	absorbing boundary conditions
AOM	acousto-optical modulator
D-structure	diamond structure
DETC	7-Diethylamino-3-thenoylcoumarin
DLW	direct laser writing
DMAc	dimethylacetamide
DMSO	dimethyl sulfoxide
FDTD	finite-difference time-domain

Formula symbols and abbreviations

Abbreviation	Explanation
FIB	focused ion beam
FTIR	Fourier-transform infrared
ITX	2-Isopropyl-9H-thioxanthen-9-one
I2959	2-Hydroxy-4'-hydroxyethoxy-2-methylpropiophenone (Irgacure 2959)
I369	2-Benzyl-2-(dimethylamino)-4'-morpholinobutyrophenone (Irgacure 369)
I651	2,2-Dimethoxy-2-phenylacetophenone (Irgacure 651)
MA	methacrylic group
MACA	methacrylated cellulose acetate
MATC	methacrylated tosylcellulose
PC	photonic crystal
PML	perfectly matched layer
SEM	scanning electron microscope
STED	stimulated emission depletion
T	tosyl group
TIR	total internal reflection

Chapter 1

Introduction

Nature has always been a great inspiration for science and engineering, a source of ideas and a template for solutions. Some examples are included in our daily life and well known like the Velcro® fastening [1] inspired by the burdock, or the hang glider inspired by the gliding of birds. Even in sophisticated aircraft construction, sharkskin-like surface texturing has been tested to reduce air resistance [2].

These are macroscopic examples, but there are also microscopic structures. The bioinspired structures span many different fields of application. At the micro- and nanometer length scale, there are more, prominent examples, like the lotus effect. Here, the lotus leaf uses micro-pillars to minimize contact surfaces and, hence, allows water and dirt to roll off [3, 4]. Other examples are implemented in our daily life, but less known, while they fascinate scientists all around the world, like the gecko feet leading to a nonchemical adhesive tape [5]. At the gecko's feet, hundreds of tiny hairs allow the gecko to walk overhead by dry adhesion [6, 7].

More examples of biological micro- and nano-structures exist in the field of optics and photonics [5]. Some of these structures can be explained by using simple geometric optics, like in the *Cataglyphis bombycina* – the silver ant [8, 9]. Others represent photonic crystals (short: PCs) [5, 10, 11] with high periodicity. They exhibit interesting optical properties, like a frequency-dependent reflection in the blue butterflies of genus *Morpho* [12] or even polarization-dependency as in the beetle *Entimus imperialis* [13].

The above mentioned PCs [14–18] achieve high reflectivity, high transmission or serve as waveguides (with designed defects) due to their periodicity and order, but they are limited to a certain spectral or angular range. In nature these limitations are a disadvantage, e.g., if a color has a signaling effect on possible mates or predators, it needs to be seen from everywhere and not only from a certain direction. In case of disorder, the affected wavelength range widens and the efficiency suffers. Through evolution, nature has found the perfect amount of disorder to broaden the desired effect in the spectral [19] or angular range [20] and keep the necessary functionality of the structure.

For structures that show similar concepts in their composition, the amount of disorder defines the exact properties of the structure. For example, a layered structure may lead

1. Introduction

to brilliant blue coloration like in the blue butterflies of genus *Morpho* [12], to a silver appearance like in different fishes [19, 21–23] or to a brilliant whiteness like in the beetle *Cyphochilus insulanus* [24–27].

The structure of white beetle achieves a maximum reflection and scattering for biomaterials with a low refractive index. Only a material with a very high refractive index, such as TiO_2 , improves the performance of the structure [27]. The beetle's structure has been mimicked by a foam-like polymer film [28], but this mimicry cannot explain the underlying concept of the structure and the source of the disorder.

The disorder of these structures can have two different causes. One possibility is that the theoretical structure already shows deviations from an ideal periodic structure that are sufficient to explain the optical effects. The other possibility is that the material provides the necessary disorder, e.g., by an additional self-assembling of the material in an ordered arrangement.

Many of the natural photonic structures consist of cellulose or chitin. The molecules of these polysaccharides are capable of self-assembling. A material-related disorder that produces the optical properties is therefore not excluded. Absorption and nonlinear effects often are not responsible for the optical properties of the structures as pure cellulose or chitin show negligible absorption and nonlinearity.

To structure a material in a tailored disordered way or to structure a material in an ordered way and allow material disorder, an arbitrary structuring has to be possible, e.g., by lithography methods. Lithography methods allow to fabricate versatile structures on the micrometer and nanometer length scale. To enable the fabrication of nearly arbitrary three-dimensional (3D) structures, direct laser writing (DLW) can be used. DLW is a lithography method that uses nonlinearities, like two-photon absorption, to change the solubility of a material, e.g., by polymerization. This allows structuring in 3D [29, 30]. Hence, it is often referred to as 3D microprinting [31].

Lithographic patterning of biomaterials, like cellulose or chitin, has been limited to two dimensions so far [32, 33], but there is a variety of other processing methods and materials. A famous biomaterial with many applications in the food industry is, e.g., cellophane. It is extracted from cellulose and can be glued or welded. Without any coatings, it is compostable [34]. Further biopolymers have similar properties and fields of application [35]. These biomaterials are often processed as thermoplastics or pressed. Also extrusion 3D printing, a more flexible structuring method, is possible [36]. On smaller length scales technologically more complex methods are applied, e.g., self-assembling. This has been applied on proteins [37], especially DNA [38, 39] strands, as well as on polymers [40] and biopolymers [41]. Self-assembling allows only a limited degree of freedom in the design of the structures.

However, the versatile DLW method does not exclude the potential applications of biomaterials as no harsh conditions, e.g., high temperature or reactive atmosphere, are needed. DLW also allows introducing a material-dependent disorder into the structures to examine their optical properties.

The structural and material aspects of the disorder have been worked on simultaneously in this project. Therefore, a suitable biomaterial-based photoresist for DLW is developed and the structures of the different natural photonic systems are analyzed.

To understand and identify suitable structures and the features that are responsible for the optical properties, different methods are applied. Some structures can be explained with fundamental optical concepts like geometric optics and refraction. More complex periodic structures can be explained with PCs. When disorder is introduced most analytic methods come up against limiting factors. Here the numerical method of finite-difference time-domain (short: FDTD) calculations can help. These methods and concepts are explained in Chapter 2.

Chapter 3 shortly introduces different methods for the structuring of biomaterials, before the versatile DLW method is explained in detail. These details incorporate a typical setup for DLW, the physical and chemical processes involved as well as a short prospect of optimization of DLW.

After the theoretical and technical background is given, the synthesis of the first known photoresist for DLW based on a polysaccharide as well as its properties are introduced in Chapter 4. Therefore, cellulose as the chosen polysaccharide is presented as well as the necessary modifications of the cellulose to enable DLW. For all components of the resist a selection of possibilities is discussed, before the chemical stability as well as the achieved resolution and feature size are classified. In the end, the first realization of a bioinspired structure in a biomimetic material is presented.

In the end, the investigated biological systems are described in more detail in Chapter 5. The underlying concepts of the silver ant (*Cataglyphis bombycina*), the blue butterflies of genus *Morpho*, the polarization-dependent beetle (*Entimus imperialis*), and the brilliant white beetle (*Cyphochilus insulanus*) are presented. The developed bioinspired models are fabricated with DLW and also presented in Chapter 5.

Contributions

This work is part of the project **Tailoring disorder in functional optical materials using a combined materials engineering and bioinspiration approach** in the priority program **Tailored disorder** and includes close cooperation with the chair for biogenic polymers from the Technical University Munich at the Science Center Straubing lead by Prof. Dr. Cordt Zollfrank. Especially, the synthesis of the cellulose derivatives has been done by Maximilian Rothammer from the Technical University Munich.

Furthermore, I supervised four students during their theses [42–45]. The corresponding results of our close cooperation are presented. In the corresponding sections, the references to the respective theses are given.

1. Introduction

Chapter 2

Theoretical background

To understand the optical properties of different structures found in nature the general interaction of light with a material has to be understood and described. The interaction between light and material can be distinguished between absorptive interaction and nonabsorptive interaction.

Absorption is a widespread concept for coloration in nature as well as in our everyday life. People get familiar with this concept already in primary school when they use watercolors. Absorptive light-matter interaction and coloration, where the different spectral parts of light are absorbed by different pigments, yields the concept of subtractive coloration. With subtractive coloration all colors mixed up result in black, in theory. In reality, it mostly yields a shade of brown. With this concept, or generally speaking with absorption, white coloration cannot be realized, as long as no fluorescent processes are included.

On the other hand, there is nonabsorptive light-matter interaction, which is present in the biological structures introduced in Chapter 5. This interaction can lead to brilliant coloration, too. In short, for this concept of coloration, light of a certain wavelength range is redirected towards the observer to obtain coloration. The theoretical background given in this chapter clarifies the different concepts of redirecting light in detail.

Therefore, the Section 2.1 starts with basic physical concepts of nonabsorptive light-matter interaction. These concepts are interference, refraction, and scattering. Section 2.2 introduces concepts to explain highly ordered photonic crystals (short: PCs) and disordered structures.

PCs reflect or transmit light of a certain wavelength or a small wavelength range due to non-absorptive light-matter interaction, in particular, due to interference. The periodicity of the PCs simplifies the explanation compared to nonperiodic arrangements. Especially disordered, but also periodic, arrangements can become too complicated to be solved analytically. Therefore, the last section of this chapter, Section 2.3, briefly introduces a method for simulating light propagation through PCs as well as through disordered structures, the finite-difference time-domain (short: FDTD) method.

2.1 Nonabsorptive light-matter interaction

Light is an electromagnetic wave. The temporal and spatial evolution of its electric and magnetic fields is described by Maxwell's equations:

$$\begin{aligned}\nabla \cdot \vec{D}(\vec{x}, t) &= \rho(\vec{x}, t), \\ \nabla \cdot \vec{B}(\vec{x}, t) &= 0, \\ \nabla \times \vec{H}(\vec{x}, t) &= \frac{\partial \vec{D}(\vec{x}, t)}{\partial t} + \vec{j}(\vec{x}, t), \\ \nabla \times \vec{E}(\vec{x}, t) &= -\frac{\partial \vec{B}(\vec{x}, t)}{\partial t},\end{aligned}\tag{2.1}$$

with the electric displacement \vec{D} , the electric field strength \vec{E} , the magnetic flux density \vec{B} , the magnetic field strength \vec{H} , the free charge density ρ , and the free current density \vec{j} .

The interaction of these electric and magnetic fields with a material is expressed by

$$\begin{aligned}\vec{D} &= \epsilon_0 \vec{E} + \vec{P}, \\ \vec{B} &= \mu_0 (\vec{H} + \vec{M})\end{aligned}\tag{2.2}$$

and includes the polarization \vec{P} , the magnetization \vec{M} , the vacuum permittivity ϵ_0 and the vacuum permeability μ_0 . The polarization and magnetization depend on the electric or magnetic field strength. These dependencies can include higher orders of the fields:

$$\begin{aligned}\vec{P} &= \epsilon_0 \sum_j \overleftrightarrow{\chi}^{(j)} \vec{E}^j, \\ \vec{M} &= \sum_j \overleftrightarrow{\chi}_m^{(j)} \vec{H}^j\end{aligned}\tag{2.3}$$

with the electric susceptibility $\overleftrightarrow{\chi}^{(j)}$ and the magnetic susceptibility $\overleftrightarrow{\chi}_m^{(j)}$ of the j th order which are in general tensors to take directional dependencies into account.

For this chapter only isotropic, linear materials ($\overleftrightarrow{\chi}^{(j)} = \overleftrightarrow{1} \chi^{(j)}$ with $\chi^{(j)} = 0$ for $j > 1$ and analogously for $\overleftrightarrow{\chi}_m^{(j)}$) are considered without any free charges ($\rho(\vec{x}, t) = 0$) or currents ($\vec{j}(\vec{x}, t) = 0$). This allows to express the electric displacement \vec{D} with the relative permittivity ϵ_r and the electric field strength \vec{E} as well as the magnetic flux density \vec{B} with the relative permeability μ_r and the magnetic field strength \vec{H} :

$$\begin{aligned}\vec{D} &= \epsilon_0 (1 + \chi) \vec{E} = \epsilon_0 \epsilon_r \vec{E}, \\ \vec{B} &= \mu_0 (1 + \chi_m) \vec{H} = \mu_0 \mu_r \vec{H}.\end{aligned}\tag{2.4}$$

With these assumptions, Maxwell's equations can be transformed into the wave equation:

$$\begin{aligned}\Delta \vec{E}(\vec{x}, t) &= \epsilon_0 \epsilon_r \mu_0 \mu_r \frac{\partial^2 \vec{E}(\vec{x}, t)}{\partial t^2} \\ &= \frac{1}{v_{\text{ph}}^2} \frac{\partial^2 \vec{E}(\vec{x}, t)}{\partial t^2} \\ &= \frac{n^2}{c_0^2} \frac{\partial^2 \vec{E}(\vec{x}, t)}{\partial t^2},\end{aligned}\tag{2.5}$$

with the phase velocity $v_{\text{ph}} = c_0/n$, the vacuum speed of light $c_0 = 1/\sqrt{\epsilon_0\mu_0}$, and the refractive index $n^2 = \epsilon_r\mu_r$. The definition of the refractive index allows negative and imaginary values. Here, only materials with positive relative permeability and positive relative permittivity are considered, which is the case for most materials [46].

All solutions of the wave equation can be written as a sum of solutions of the form:

$$\begin{aligned}\vec{E}(\vec{x}, t) &= \vec{E}_0 \exp\left[i(\vec{k} \cdot \vec{x} - \omega t)\right], \\ \vec{B}(\vec{x}, t) &= \vec{B}_0 \exp\left[i(\vec{k} \cdot \vec{x} - \omega t)\right],\end{aligned}\tag{2.6}$$

with the amplitude of the electric field strength \vec{E}_0 and the magnetic flux density \vec{B}_0 , the wave vector \vec{k} , and the angular frequency ω . The wave vector and the angular frequency correlate to the wavelength λ and the frequency ν according to:

$$\begin{aligned}|\vec{k}| &= \frac{2\pi}{\lambda}, \\ \omega &= 2\pi\nu,\end{aligned}\tag{2.7}$$

respectively, with $\nu\lambda = v_{\text{ph}}$.

By substituting the solution of the wave equations given in Equation 2.6 into the Maxwell's equation and subsequent Fourier transformation, the following relation between the amplitudes of the magnetic flux density and the electric field strength results:

$$\vec{B}_0 = \frac{1}{2\pi\nu} \vec{k} \times \vec{E}_0,\tag{2.8}$$

Equation 2.6 and 2.8 define a plane transversal wave. Using this plane transversal wave different aspects of light-matter interaction are explained in the different subsections namely: interference, refraction, and scattering. The subsections contain a brief reminder of the basic principles, which can be supplemented by reading text books like [47–50].

2.1.1 Interference

An important phenomenon in optics is the interference of electromagnetic waves. Interference describes the superposition of two waves in a point in time and space. The resulting electric field is the sum of the two fields concerning the phase and amplitude of the different waves and not the sum of their intensities. Interference occurs between electromagnetic waves with different as well as with the same frequencies. A wave can even interfere with its own reflection.

The resulting electric field \vec{E}_{res} of the interference of two plane waves \vec{E}_1 and \vec{E}_2 (with amplitudes \vec{E}_{0j} , wave vectors \vec{k}_j , and angular frequencies ω_j ; cf. Eq. 2.6) at a certain point in space \vec{x} and time t is mathematically described as:

$$\begin{aligned}\vec{E}_{\text{res}}(\vec{x}, t) &= \vec{E}_1(\vec{x}, t) + \vec{E}_2(\vec{x}, t) \\ &= \vec{E}_{01} \exp\left[i(\vec{k}_1 \cdot \vec{x} - \omega_1 t)\right] + \vec{E}_{02} \exp\left[i(\vec{k}_2 \cdot \vec{x} - \omega_2 t)\right].\end{aligned}\tag{2.9}$$

2. Theoretical background

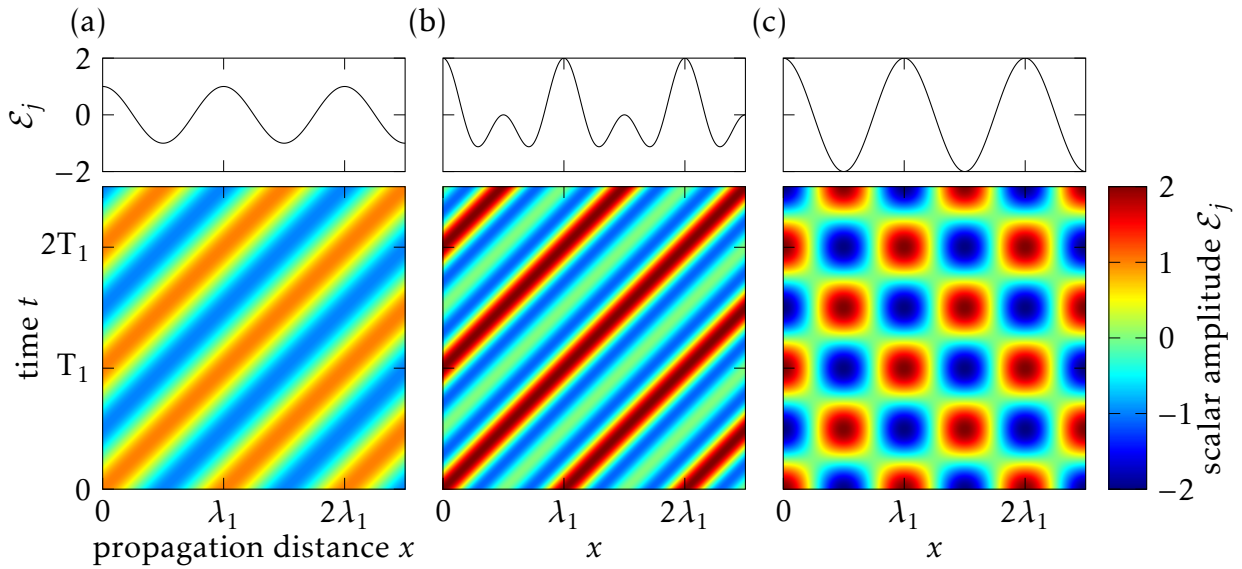


Figure 2.1: The electric field of one-dimensional waves with the same amplitude over space and time normalized to the maximum of a single wave: (a) of a single wave, (b) of two waves with $|\vec{k}_2| = 2|\vec{k}_1|$ leading to a beat, and (c) with $\vec{k}_2 = -\vec{k}_1$ leading to a standing wave.

With the assumption $\vec{E}_{01} = \vec{E}_{02} = \vec{E}_0$, the representation of the imaginary exponential function as $\exp(i\alpha) = \cos(\alpha) + i\sin(\alpha)$, and addition theorems, a transformation of Equation 2.9 leads to:

$$\vec{E}_{\text{res}}(\vec{x}, t) = 2\vec{E}_0 \cos\left[\frac{(\vec{k}_1 - \vec{k}_2) \cdot \vec{x} - (\omega_1 - \omega_2)t}{2}\right] \exp\left[i\frac{(\vec{k}_1 + \vec{k}_2) \cdot \vec{x} - (\omega_1 + \omega_2)t}{2}\right]. \quad (2.10)$$

The first part of Equation 2.10 describes the behavior of the maximum amplitude or the envelope, the so-called beat, which is modulated with the difference of the frequencies and wave vectors. The second term characterizes the modulation under the envelope.

For one-dimensional (short: 1D) waves $\vec{E}_j(\vec{x}, t) = \mathcal{E}_j(x, t)\vec{e}$ with \mathcal{E}_j the scalar amplitude and \vec{e} the unit vector in the direction of the field (cf. Fig. 2.1 (a)), two different cases of interference are shown in Figure 2.1: the more general case of a beat with $|\vec{k}_2| = 2|\vec{k}_1|$ (cf. Fig. 2.1 (b)) and the case of a standing wave with $\vec{k}_2 = -\vec{k}_1$ (cf. Fig. 2.1 (c)).

If more waves with different frequencies or directions are involved, the interference pattern in space and time becomes more complicated, but often also more useful, as in the case of short pulses or PCs (see Sec. 2.2) [15, 51]. The interference of waves is used to explain the refraction in the following section.

2.1.2 Refraction

Refraction describes the effect of the presence of an interface between bulk materials on the propagation of light. In the different materials, the phase velocity changes with the refractive index of the material. As a consequence of the changed phase velocity, light

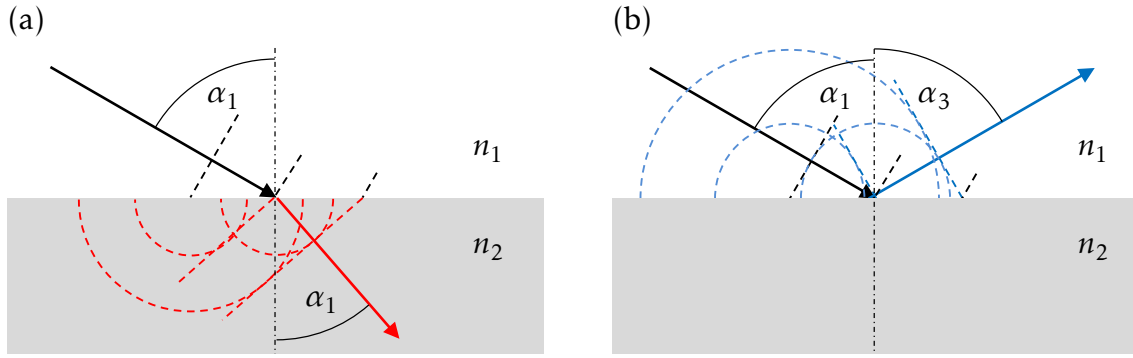


Figure 2.2: (a) Transmission and (b) reflection at an interface of two different materials with different refractive indices n_1 and n_2 and hence different phase velocities. The dashed circles and lines indicate points with a constant phase.

that is propagating towards an interface between two materials (n_1 and n_2) with an angle of incidence α_1 (cf. Fig. 2.2) is refracted at the interface as described by Snell's law:

$$n_1 \sin(\alpha_1) = n_2 \sin(\alpha_2), \quad (2.11)$$

with an angle of propagation α_2 in the second medium.

Snell's law can be explained by considering a plane wave with a phase front perpendicular to the propagation direction as sketched in Figure 2.2 (a) and (b) in black. A phase front includes neighboring points in space with a constant phase. These phase fronts are marked in Figure 2.2 with dashed lines.

This plane wave is incident on an interface. At every point at the interface the plane wave excites spherical waves, whose phase fronts are marked with dashed half circles in Figure 2.2. In transmission (cf. Fig. 2.2 (a) red) and in reflection (cf. Fig. 2.2 (b) blue), these spherical waves interfere to form plane waves again. In the different materials the spherical waves have propagated by a different amount in space, therefore, the radii of the indicated phase fronts in Figure 2.2 (a) and (b) are different and the resulting plane waves propagate at different angles. In transmission, the propagation direction of the resulting plane wave corresponds to the prediction of Snell's law α_2 , while in reflection, the angle α_3 coincides with the angle of incidence α_1 .

This observed refraction of light is induced by the reactions of atoms and molecules to the electric and magnetic field of the wave. These reactions are expressed by the polarization \vec{P} and magnetization \vec{M} that depend on the electric and magnetic field strength as described in Equation 2.3.

At the atomic level, the polarization can be understood as a displacement of the electrons (mass m_e , charge q) relative to the positive core [47]. In the model system of the Lorentz oscillator, the Coulomb interaction between the electrons and the core is simplified as a spring (spring constant κ) with damping (γ). The electron is then deflected from its rest position by the periodic electric field of the wave. Hence, this represents a driven damped harmonic oscillator, where the position of the electron is given by the linear differential

2. Theoretical background

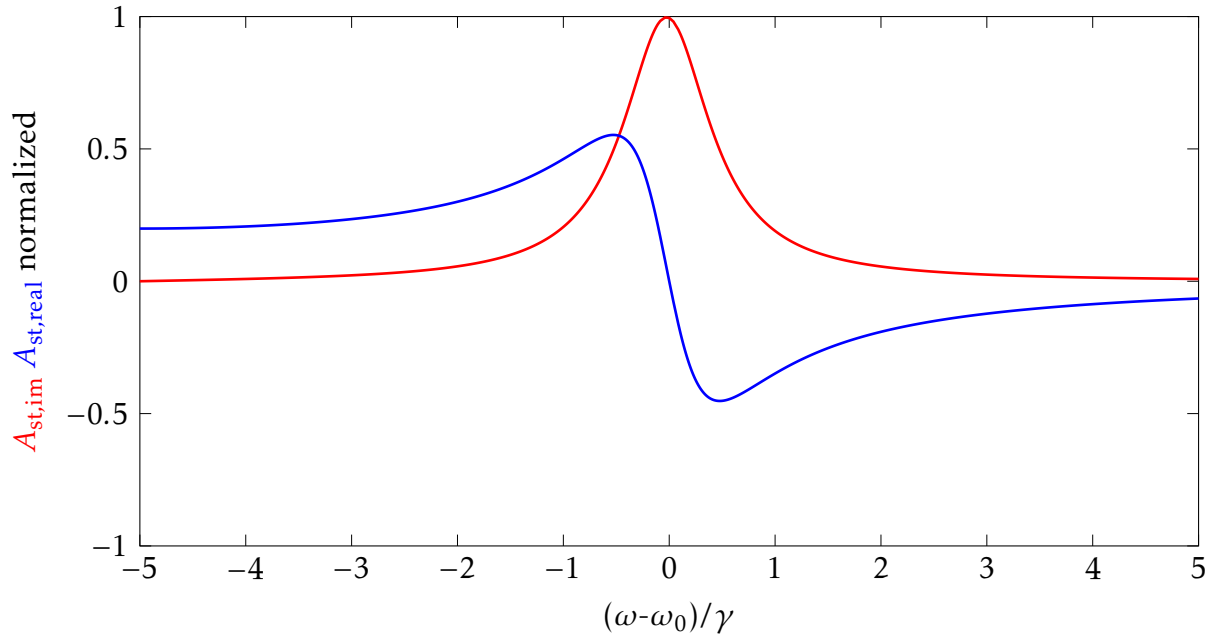


Figure 2.3: Trend of the real (blue) and imaginary (red) part of the amplitude of a forced oscillation, which corresponds to the qualitative behavior of the susceptibility χ near a resonance.

equation:

$$\begin{aligned}
 m_e \ddot{\vec{x}}(t) &= -\kappa \vec{x}(t) - \gamma m_e \dot{\vec{x}}(t) + q \vec{E}(t), \\
 \ddot{\vec{x}}(t) + \gamma \dot{\vec{x}}(t) + \frac{\kappa}{m_e} \vec{x}(t) &= \frac{q}{m_e} \vec{E}_0 \exp(-i\omega t), \\
 \ddot{\vec{x}}(t) + \gamma \dot{\vec{x}}(t) + \omega_0^2 \vec{x}(t) &= \frac{q}{m_e} \vec{E}_0 \exp(-i\omega t),
 \end{aligned} \tag{2.12}$$

with $\omega_0^2 = \frac{\kappa}{m_e}$. Possible solutions are linear combinations of solutions of the homogeneous linear differential equation

$$\vec{x}(t) = \exp\left(-\frac{\gamma}{2}t\right) \left[\vec{A}_1 \exp\left(-i\sqrt{\omega_0^2 - \frac{\gamma^2}{4}}t\right) + \vec{A}_2 \exp\left(i\sqrt{\omega_0^2 - \frac{\gamma^2}{4}}t\right) \right], \tag{2.13}$$

and the stationary solution

$$\vec{x}(t) = \frac{q}{m} \frac{\vec{E}_0}{\omega_0^2 - i\gamma\omega - \omega^2} \exp(-i\omega t). \tag{2.14}$$

The amplitude

$$\vec{A}_{\text{st}} = \frac{q}{m} \frac{\vec{E}_0}{\omega_0^2 - i\gamma\omega - \omega^2} \tag{2.15}$$

of the stationary solution includes an imaginary part $A_{\text{st},\text{im}}$ (red curve in Fig. 2.3) that represents the damping of the oscillation and a real part $A_{\text{st},\text{real}}$ (blue curve in Fig. 2.3) that describes the deflection of the electron from its rest position.

This deflection of the electron $\vec{x}(t)$ leads to an atomic polarization that contributes to the macroscopic polarization and, thus, to the electrical susceptibility χ (cf. Eq. 2.3). There-

fore, the qualitative course of the deflection corresponds to the course of the susceptibility χ near a resonance and, hence, the relative electric permittivity ϵ_r .

The relative electric permittivity ϵ_r , on the other hand, relates to the refractive index in isotropic diamagnetic ($\mu_r \approx 1$) materials according to: $n(\nu) = \sqrt{\epsilon_r(\nu)}$. The qualitative course of the refractive index thus also corresponds to the course of the deflection of the electron shown in Figure 2.3.

This implies, that the refractive index exhibits an imaginary part and a real part. The large imaginary part near a resonance corresponds to a strong absorption of the wave. The real part, representing the change of the phase velocity, approaches $n = 1$ for frequencies much smaller or larger than the resonance because of the correlation with the susceptibility $n = \sqrt{\epsilon_r} = \sqrt{1 + \chi}$.

In a solid or a molecule, many different resonances build a far more complex progression of the refractive index, but the principle can be understood with the model of the Lorentz oscillator described above: Electromagnetic waves with frequencies near a resonance frequency experience high absorption, while the refractive index changes greatly near a resonance.

The dependence of the refractive index on the frequency $\frac{dn}{d\omega}$ is termed dispersion. It is distinguished between normal dispersion, where $\frac{dn}{d\omega} > 0$, and anomalous dispersion ($\frac{dn}{d\omega} < 0$) for frequencies ω near a resonance ω_0 :

$$(\omega_0^2 - \omega^2)^2 < \gamma^2 \omega_0^2. \quad (2.16)$$

For frequencies outside the interval given in Equation 2.16, normal dispersion occurs that results in a higher refractive index for larger frequencies or smaller wavelengths. Dispersion results in the splitting of polychromatic light in the material, like the divergence of an optical pulse or the fanning out of white light in a prism.

To observe refraction, the spherical waves that originate at the interface must interfere. This interference requires a correlation between the molecules and atoms of the material that emit these spherical waves, otherwise light will be scattered, as discussed in the next section.

2.1.3 Scattering

Scattering describes the deflection of light out of the original direction due to an interaction of the atoms or molecules with the electromagnetic field of the light, like the above mentioned forced oscillations of electrons.

In general, during a scattering process, atoms or molecules in a medium are excited by the electromagnetic wave as described in Section 2.1.2, which again leads to the emission of electromagnetic radiation. This emission spreads in all directions and, thus, also out of the original direction.

2. Theoretical background

A first differentiation between the types of scattering concerns the phase relation between the individual emitted wave and the other emitted waves and the exciting wave. For coherent scattering, there is a fixed phase relation between the different scattered waves (spatially coherent) and between the scattered wave and the exciting wave (temporally coherent) [47, 51].

The fixed phase relation between the different scattered waves is achieved by a high spatial correlation of the scattering centers, as in a crystal. Due to the fixed phase relation, the scattered intensity results from the interference of the different waves leading to a maximum intensity that is proportional to the squared number of scattering centers. This may lead to refraction (cf. Sec. 2.1.2) or diffraction as a result of the coherent scattering of coherent waves [47]. To preserve the phase correlation between the exciting wave and the scattered wave, there may not be any statistic retardation of the emission like in absorption and emission. The scattering has to be elastic [52].

If there is no fixed phase relation between the scattered light and the exciting wave, for example, if the light is first absorbed and shortly afterwards emitted, the scattering is temporally incoherent. Spatially incoherent scattering is due to missing spatial correlation between the different scattering centers, like in a powder. The scattered intensity is then only proportional to the number of scattering centers.

Often only one type of phase relation is considered to differentiate between coherent and incoherent scattering, either between the incoming wave and the scattered one or between the different scattered waves. This may lead to confusion, as the scattering of the wave at a single particle may be temporally coherent, while the overall scattering at the different particles is spatially incoherent.

If temporally coherent scattering at a single particle is considered, there is another differentiation between types of scattering. It can be classified by the proportion of the particle size d and the wavelength λ . For particles with a cross-section $d \ll \lambda$, such as molecules in the atmosphere, so-called Rayleigh scattering occurs. The small particles build oscillating dipoles, which emit their intensity in all directions except the direction of the dipole moment. The scattered intensity I then depends on the amplitude of the incoming wave \mathcal{E} and the frequency ν

$$I \propto \mathcal{E}^2 \nu^4, \quad (2.17)$$

for frequencies much smaller than the resonance. This leads to the blue appearance of the sky as the higher, blue frequencies are scattered more strongly than the smaller red ones. A large amount of the blue light is scattered from its original direction, resulting in blue ambient illumination in the atmosphere.

If the particle dimensions are of the order of the wavelength, mainly forward scattering and backscattering take place [53]. This regime is called Mie scattering. These larger particles have spatially correlated scattering centers. Therefore, parts of the waves interfere destructively in the direction perpendicular to the original one.

The exact intensity distribution for large, irregular scattering centers can only be calculated numerically with methods like FDTD calculations (cf. Sec. 2.3).

2.2 Periodic and nonperiodic arrangements

The concepts in Section 2.1 are used to explain the propagation of light through a material system. As the size and complexity of these systems increase, the analytical prediction of light propagation using the above concepts becomes more complicated. Here, other concepts help to describe the propagation of light in these complex material systems. This section presents two different classes of material systems and corresponding ways to describe the optics of these systems: Photonic crystals have a strict periodicity and therefore a high degree of order (cf. Sec. 2.2.1), while disordered structures have no periodicity and no order, but there are also some useful concepts for their description (cf. Sec. 2.2.2).

2.2.1 Photonic crystals

The periodic arrangement of materials with different refractive indices in optics is called a photonic crystal (short: PC). The periodicity may concern one (short: 1D), two (short: 2D) or even three dimensions (short: 3D), correspondingly speaking of a one, two, or three-dimensional PC. The interference between partial waves inside the PC inhibits the propagation of light with certain frequencies in certain directions. Electromagnetic waves with other frequencies or directions can propagate through the material. To find these possible solutions of Maxwell's equations inside a PC, the periodicity of the structure is considered.

How appropriate solutions are found is outlined here. For this purpose, isotropic, time-independent, linear materials that show negligible magnetic effects ($\mu_r \approx 1$) without free charges or currents are assumed. The periodic refractive index profile thus originates from the periodic relative permittivity. Furthermore, only harmonic solutions are considered in this approach as they build all other solutions by Fourier analysis. They exhibit a periodic time dependence $\exp(-i\omega t)$ as well as spatial solutions $\vec{E}(\vec{x})$ and $\vec{H}(\vec{x})$:

$$\vec{E}(\vec{x}, t) = \vec{E}(\vec{x}) \exp(-i\omega t) \quad (2.18)$$

and

$$\vec{H}(\vec{x}, t) = \vec{H}(\vec{x}) \exp(-i\omega t). \quad (2.19)$$

With Equation 2.18 and Equation 2.19 and the materials dependencies expressed in Equation 2.4 the third and fourth of Maxwell's equations (cf. Eq. 2.1) lead to the master equation for PC:

$$\begin{aligned} \nabla \times \left[\frac{1}{\epsilon_r(\vec{x})} \nabla \times \vec{H}(\vec{x}) \right] &= \left(\frac{\omega}{c_0} \right)^2 \vec{H}(\vec{x}) \\ \hat{\Theta} \vec{H}(\vec{x}) &= \left(\frac{\omega}{c_0} \right)^2 \vec{H}(\vec{x}), \end{aligned} \quad (2.20)$$

2. Theoretical background

with the linear Hermitian operator $\hat{\Theta}$ [15]. Appendix A contains a proof of the hermiticity and linearity of the operator.

The term crystal already reveals a certain similarity to crystals in solid state physics, which are described by the Schrödinger's equation [54]:

$$\begin{aligned} \mathcal{H}\Psi(\vec{x}) &= E\Psi(\vec{x}) \\ \left[-\frac{\hbar^2}{2m}\nabla^2 + V(\vec{x}) \right] \Psi(\vec{x}) &= E\Psi(\vec{x}). \end{aligned} \quad (2.21)$$

In both cases, the solutions for either the magnetic field $\vec{H}(\vec{x})$ or the electron wave function $\Psi(\vec{x})$ are solutions of an eigenvalue problem. This eigenvalue problem contains a linear operator $\hat{\Theta}$ or \mathcal{H} , respectively, and a periodic potential. This periodic potential is either the relative permittivity $\epsilon_r(\vec{x} + \vec{a}_j) = \epsilon_r(\vec{x})$ (cf. Eq. 2.20) or the atomic potential $V(\vec{x} + \vec{a}_j) = V(\vec{x})$ (cf. Eq. 2.21). The lattice vector \vec{a}_j describes the periodicity of these potentials in a certain direction j .

Due to the rotation in the linear operator $\hat{\Theta}$ (cf. Eq. 2.20), the different components of the magnetic field H_x , H_y , and H_z are in general not separable [15]. Therefore, analytic solutions can only be found for simple systems.

The possible solutions of these eigenvalue problems with periodic potentials, the so-called Bloch waves ([15, 54, 55]), show the same periodic spatial dependency as the potential landscapes:

$$\vec{H}_{\vec{k}}(\vec{x}) = \vec{u}_{\vec{k}}(\vec{x}) \exp(i\vec{k} \cdot \vec{x}) \text{ with } \vec{u}_{\vec{k}}(\vec{x} + \vec{a}_j) = \vec{u}_{\vec{k}}(\vec{x}). \quad (2.22)$$

The Bloch waves build a system of possible solutions. Here, solutions with wave vectors \vec{k}_1 and $\vec{k}_2 = \vec{k}_1 + \vec{g}_j$, where \vec{g}_j is a reciprocal lattice vector, are equal due to the translation invariance. Therefore, the system of solutions can be reduced to solutions with wave vectors in the first Brillouin zone. The first Brillouin zone is the unit cell of the reciprocal space and corresponds to the Wigner-Seitz cell in real-space. The first Brillouin zone is limited by the reciprocal lattice vectors, such that all wave vectors $\vec{k} \cdot \vec{e}_j \leq \frac{1}{2}|\vec{g}_j|$ with a unit vector $\vec{e}_j \parallel \vec{g}_j$ are part of the first Brillouin zone.

The assignment of wave vectors and allowed frequencies leads to a band structure. In some cases there are no possible wave vectors for particular directions or even for all directions for certain frequencies. These frequencies then lie in a bandgap or, correspondingly, in a complete bandgap.

The size of the bandgap is determined by an energy difference of the electromagnetic waves above and below the bandgap. This energy difference is caused by the different permittivities at the nodes and anti-nodes of the two waves in real-space [15]. The differences of the relative permittivities correlate with the refractive index contrast of the different materials used in this structure. For a 1D PC with a layer thickness of $\frac{a_j}{2}$ and a refractive index of $n_1 = 1$ for one layer and $n_2 = 1$, $n_2 = 1.5$, or $n_2 = 3$ for the second layer,

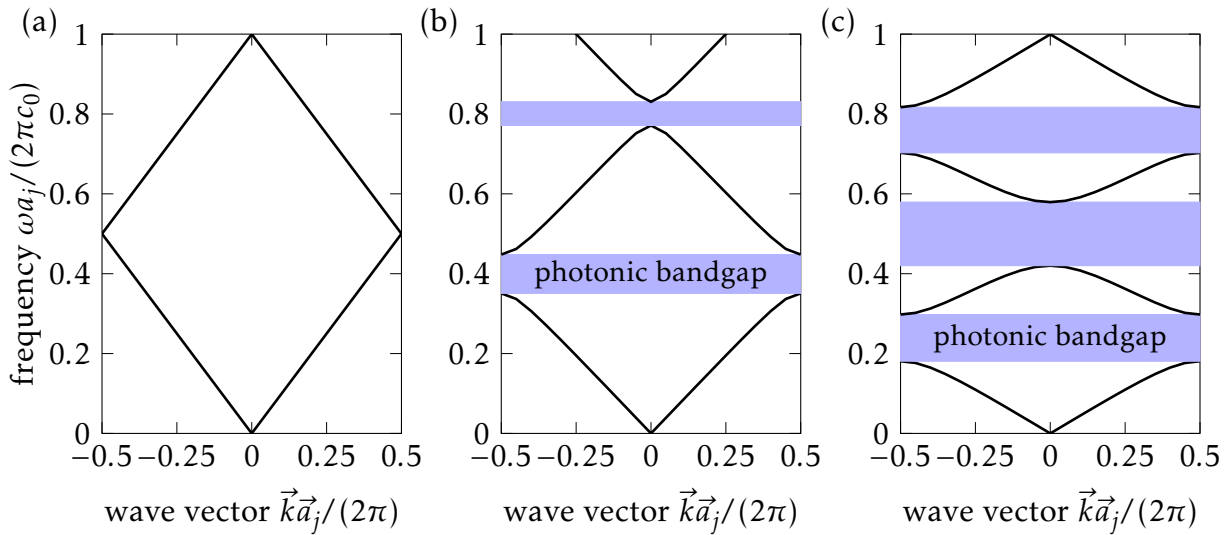


Figure 2.4: Photonic bandstructure of a 1D PC with refractive index contrast of (a) $n_2 - n_1 = 0$, (b) $n_2 - n_1 = 0.5$, and (c) $n_2 - n_1 = 2$. Bandgaps are marked in blue.

the resulting band structures of wave vectors and frequencies are illustrated in Figure 2.4. With increasing contrast of the refractive indices, the bandgap opens further.

A fabricated layered structure exhibits such a bandgap only for light propagating exactly perpendicularly to the layers. Strictly speaking, the band structures shown in Figure 2.4 (b) and (c) are only a section of the band structure of a real structure. The complete band structure includes all directions and is far more complicated.

For 2D and 3D PCs the band structure may exhibit different bandgaps for different directions. Only few structures exhibit so-called complete bandgaps, where a bandgap exists at a certain frequency for all directions. Structures that show a complete bandgap at a sufficiently large refractive index contrast are, e.g., so-called Yablonovite structures [56] and woodpile structures [57]. Further information about PCs can be found in books like [15].

2.2.2 Disordered structures

Besides the ordered and periodic PC, there are structures with neither periodicity nor order. A prominent example of these disordered structures is biological tissue [58]. Due to the missing order of these materials, their optical behavior is characterized by spatially incoherent scattering (cf. Sec. 2.1.3). Therefore, an analytic description with an exact solution of Maxwell's equations is impossible within the scope of today's computing capacities.

However, a useful characterization of the optical properties of these disordered materials is achieved by introducing the absorption length l_a , the scattering mean free path l_s , and the transport mean free path l_{tr} . The absorption length l_a describes the average length a photon propagates inside a material before it is absorbed, while the scattering mean free path l_s is the average distance between two scattering events. Finally, the transport mean free path l_{tr} describes after which length light propagation becomes randomized in its

2. Theoretical background

direction. This means, that for light that has spread in a material more than the transport mean free path l_{tr} , it is impossible to tell where it came from. [24, 59, 60]

For multiple scattering events ($l_a \gg l_{tr}$), the optics of these materials can be described with diffusion theory [24, 59]. Then the transport mean free path is linked to the lifetime of a short optical pulse inside the disordered structure or material. Therefore, it can be experimentally identified. For these time-of-flight measurements, a short optical pulse is sent through the structure. Its original shape and its shape after passing the material are compared. The broadening of the pulse due to multiple scattering reveals the photon lifetime in the structure. [24]

The results of these measurements can be used to adapt and compare the scattering properties to simulations done with the Monte Carlo method. This method is an alternative to diffusion theory if there is low-order scattering instead of multiple scattering [59]. The Monte Carlo method is a simulation method for statistical processes, like particle transport in a medium or neutron diffusion through a wall [61]. In photonics and optics Monte Carlo methods are used to simulate light propagation in disordered media like biological tissue [25, 58]. Thereby, the wave character of light is neglected. Monte Carlo simulations consider the mean propagation length between scattering events l_s and the statistic deflection of the photons due to a scattering event, which is expressed by the relation between the scattering mean free path l_s and the transport mean free path l_{tr} [24, 59]. With this information, random walks of the photons are calculated through a material leading to an overall intensity distribution in the end.

If the information needed for the Monte Carlo simulations can not be obtained from measurements, they may be a result of FDTD calculations. FDTD calculations enable a numerical solution of Maxwell's equations even for disordered media as described in the next section.

2.3 Finite-difference time-domain method

The finite-difference time-domain (short: FDTD) method is a method to numerically solve Maxwell's equations for electromagnetism on a discrete grid in time and space. This enables the solution for complex and aperiodic structures. It is also called Yee-algorithm after its inventor Kane Yee [62].

The intention of this chapter is to summarize the main ideas of different aspects of the FDTD method needed to understand this work. Additional information can be found in literature [63, 64].

2.3.1 Working principle

The FDTD method approximates the derivatives in Maxwell's equations (cf. Eq. 2.1) by difference quotients of the field components at neighboring grid points in time and space.

The general formalism can be understood using the special case of a plane wave ($D_j = 0$ with $j \in \{y, z\}$ and $B_j = 0$ with $j \in \{x, z\}$) traveling in the z direction in free space ($\rho = 0$, $\vec{j} = \vec{0}$, and $n = 1$). Maxwell's equations (cf. Eq. 2.1), then, can be reduced to two equations:

$$\begin{aligned} (\nabla \times \vec{E})_y &= \frac{\partial E_x}{\partial z} = -\frac{\partial B_y}{\partial t}, \\ (\nabla \times \vec{H})_x &= -\frac{\partial H_y}{\partial z} = \frac{\partial D_x}{\partial t}. \end{aligned} \quad (2.23)$$

With the difference quotients, these equations discretize to:

$$\begin{aligned} \frac{E_x(z_0 + \Delta z, t_0) - E_x(z_0 - \Delta z, t_0)}{2\Delta z} &= -\frac{B_y(z_0, t_0 + \Delta t) - B_y(z_0, t_0 - \Delta t)}{2\Delta t}, \\ \frac{H_y(z_0 + \Delta z, t_0) - H_y(z_0 - \Delta z, t_0)}{2\Delta z} &= \frac{D_x(z_0, t_0 + \Delta t) - D_x(z_0, t_0 - \Delta t)}{2\Delta t}. \end{aligned} \quad (2.24)$$

These discretizations allow to express the magnetic field of a future time step by the magnetic field at the same point in space a time step earlier and the electric fields of the neighboring points in space at the current time step, and vice versa:

$$\begin{aligned} B_y(z_0, t_0 + \Delta t) &= B_y(z_0, t_0 - \Delta t) - 2\Delta t \frac{E_x(z_0 + \Delta z, t_0) - E_x(z_0 - \Delta z, t_0)}{2\Delta z}, \\ D_x(z_0, t_0 + \Delta t) &= D_x(z_0, t_0 - \Delta t) - 2\Delta t \frac{H_y(z_0 + \Delta z, t_0) - H_y(z_0 - \Delta z, t_0)}{2\Delta z}. \end{aligned} \quad (2.25)$$

By considering the difference quotients of the other spatial coordinates, the method is expanded to three dimensions. For materials, the tensor of the relative permittivity $\overleftrightarrow{\epsilon}_r$ and the tensor of the permeability $\overleftrightarrow{\mu}_r$, as well as charges and currents, have to be regarded. A potential spatial dependency of the permittivity and the permeability are included in Equation 2.23 by considering \vec{E} and \vec{B} as well as \vec{D} and \vec{H} . Here, also nonlinear effects can be considered [65, 66].

The approximation of the differentials with the difference quotients becomes more precise if the electric and magnetic fields are calculated at different points in time and space, so that the corresponding points of the electric field are shifted by half an increment towards the corresponding points of the magnetic field in space and time. Then, Δz and Δt in Equation 2.25 are replaced by $\Delta z/2$ and $\Delta t/2$ which leads to a more precise approximation of the derivations.

The field variations between two points have to be small to allow a good and precise approximation of the differentials. Therefore, all increments have to be chosen in a way that the relative phase of the electric and magnetic fields between neighboring points in time and space is small. Hence, the distances between two neighboring points, the spatial increments Δx , Δy , and Δz , have to be small compared to the wavelength and compared to spatial features of the structure [62, 67]. All spatial increments can (but do not have to) be chosen identical:

$$\Delta x = \Delta y = \Delta z \ll \lambda. \quad (2.26)$$

2. Theoretical background

Furthermore, the time increment Δt has to be chosen in a way that the phase difference between two neighboring points in space at consecutive time steps is still small [67]:

$$\Delta t \ll \frac{1}{v_{\text{ph}}} \left[\frac{1}{(\Delta x)^2} + \frac{1}{(\Delta y)^2} + \frac{1}{(\Delta z)^2} \right]^{-\frac{1}{2}}. \quad (2.27)$$

The grid pattern may change over the simulation volume. This is useful to adapt to certain structural features, e.g., the corresponding spatial increments can be smaller in areas of very fine features and larger in free space. Furthermore, it can be chosen in a non-orthogonal way to adapt to curved surfaces. [68]

The simulation accuracy increases with smaller increments as the difference quotients approach the derivatives. However, the computation time as well as the memory requirements increase as well, as the electric and magnetic fields have to be calculated and stored for at least two time steps for every grid point in space. Hence, the selection of the simulation grid is a trade-off between accuracy and computational power.

2.3.2 Boundary conditions

As the necessary computational power scales with the number of grid points and hence with the volume, the volume has to be terminated. The boundaries of the volume must not influence the results of the simulation. This requires an adaptation of the boundary conditions to the investigated problem.

In his first paper [62], Yee described the boundaries of the simulation volume as perfectly conducting surfaces, where the tangential electric and the normal magnetic field components are simply set to 0 at the boundary. These boundaries are easily implemented in the algorithm but far from reality, as only very few problems occur in a volume, which is incorporated in a perfectly conducting box.

Still relatively easy to simulate, but far more realistic, is the case of a periodic problem, like the vertical incidence of a plane wave on a periodic structure. At the boundaries, $x = 0 \cdot \Delta x$ and $x = j \Delta x$ perpendicular to the propagation of the wave, the electric and magnetic fields are calculated regarding the fields at the opposite boundary

$$\vec{B} \begin{pmatrix} 0 \cdot \Delta x \\ y_0 \\ z_0 \\ t_0 + \Delta t \end{pmatrix} = \vec{B} \begin{pmatrix} 0 \\ y_0 \\ z_0 \\ t_0 - \Delta t \end{pmatrix} + f \left[\vec{E} \begin{pmatrix} j \Delta x \\ y_0 \\ z_0 \\ t_0 \end{pmatrix} \right]. \quad (2.28)$$

Here $f \left[\vec{E}(j \Delta x, y_0, z_0, t_0) \right]$ includes the difference quotients of the electric field build with the points $x = 1 \cdot \Delta x$ and $x = j \cdot \Delta x$. The boundaries in the direction of propagation or the boundaries of aperiodic problems remain challenging.

In contrast to “hard” boundary conditions (i.e., perfectly conducting surfaces), “soft” boundary conditions are needed. They result in absorption or leakage of the outgoing

wave without any reflection [67]. Two concepts exist for those absorbing boundary conditions (short: ABC). One concept uses the differential equations and modifies the algorithm at the boundaries to only allow waves that leak out of the simulation volume. The second concept uses an additional material at the boundary which absorbs the wave without reflection [68].

One example for the first kind of ABC couples the field amplitude outside the boundary ($z_0 + \Delta z$) to the amplitude inside the simulation volume at a former time step [67], while it neglects the other points outside the boundary. The spatial distance and the temporal distance are thereby correlated to describe the propagation of a wave in vacuum

$$D_x(z_0 + \Delta z, t_0 + \Delta t) = D_x(z_0, t_0), \quad (2.29)$$

with $\Delta z = c\Delta t$.

This boundary condition provides exact results in one dimension. For two and three dimensions, there are discrepancies due to waves with different angles of incidence relative to the boundary. There are possible adaptations like averaging over different points, but there is still some reflectance from the boundary inside the simulation volume. [67]

The most promising ABC is a material-based concept presented by Berenger in 1994: the concept of the perfectly matched layer (short: PML) [69]. The PML is a layer of a simulated absorbing material, which has the same impedance $Z = \sqrt{\frac{\mu_0\mu_r}{\epsilon_0\epsilon_r}}$ as the area inside the actual simulation volume. Due to the correlation of the impedance and the reflectance coefficient

$$r = \frac{Z_1 - Z_2}{Z_1 + Z_2}, \quad (2.30)$$

there is no reflectance at an interface between two materials with the same impedance [63]. This correlation describes the reflectance coefficient for normal incident light. Thus, there may be some reflectance for light under other angles of incidence on the boundary that can be reduced if the PML is considered anisotropic [70]. With the imaginary parts of the relative permittivity ϵ_r and relative permeability μ_r the absorption can be adapted inside the PML. The PML layer has to be enclosed by a “hard” boundary after a sufficiently thick absorbing PML.

The “soft” boundaries need additional resources for computation. Hence, a clever selection of the boundary conditions and the simulation geometry can reduce computation time and resources.

2.3.3 Advantages and disadvantages of FDTD

Besides FDTD, frequency-domain methods are a popular tool for solving optical problems. For the sake of completeness, FDTD will be briefly compared with these methods with respect to the corresponding advantages and disadvantages.

Frequency-domain methods use a Fourier decomposition of a signal and regard the propagation of the different frequencies. Therefore, the propagation of a wave with a certain

2. Theoretical background

frequency is described with a matrix solving the problem for this single frequency. For a signal or a frequency range, the problem has to be solved for all frequencies before a global solution can be calculated via a Fourier composition. The adaptation of the formalism to certain frequencies and geometries is complicated. In contrast, in FDTD only the material properties at the different grid points have to be adapted [67].

With the exact matrices for each problem, the frequency-domain methods are more accurate than FDTD and need less calculation time. On the other hand, these matrices need a lot of computational storage due to their size, whereas FDTD only needs to store the fields of two time steps for every grid point. [67]

With frequency-domain methods, frequency-dependent processes (e.g., dispersion in a material) are easy to implement as the material properties are adjusted for the single frequencies. If it comes to nonlinearities, however, FDTD is at an advantage. In FDTD the total intensity is directly given and the material properties at the different grid points are easily adapted to the field amplitudes at the time steps.

For disordered structures and calculations for a spectral range instead of a single frequency, the complicated adaptation of the different investigated structures to the frequency-domain method makes FDTD advisable.

Chapter 3

Methods

Biomimetics in 3D micro- and nano-structuring contains different aspects. On the one hand it concentrates on the use of biomimetic materials, materials derived from naturally occurring materials, or uses these biomaterials themselves, and on the other hand it involves the fabrication of biomimetic structures, like those described in Chapter 5, in conventional materials.

From the material point of view biomimetics uses biomaterials like proteins or polysaccharides to generate structures. Some known methods to structure these materials are introduced in the first section of this chapter (cf. Sec. 3.1). These methods and, especially, the self assembling have a limited freedom of design. Therefore, it is impossible to fabricate arbitrary 3D structures.

In contrast, the method of direct laser writing (short: DLW) allows for fabrication of nearly arbitrary structures. But currently, there is no way to use biopolymers for DLW. The processing conditions of DLW, however, allow the use of biomaterials, as no harsh conditions, e.g., high temperature or reactive atmosphere, are needed. To give the reader an understanding of the requirements on a resist that should be patternable with DLW, the method is described in Section 3.2.

3.1 Structuring biomaterials

In the context of this work, biomaterials are materials that exist in nature like polysaccharides, proteins or peptides. They often tend to organize themselves in larger clusters in nature, i.e., they self-assemble. This assembling is dictated by weak non-covalent interactions between the single molecules or within a molecule [37, 71].

The corresponding molecules exhibit a chemical structure that allows a weak association between different functional groups of the molecules. For cellulose, the responsible interactions are hydrogen bonds (cf. Sec. 4.1). For other molecules, it can be ionic bonds, van der Waals interactions, or hydrophobic interactions [37, 71]. If the interactions occur between different parts of a single molecule, they lead to a folding of the molecules. If they

3. Methods

occur intermolecularly they lead to an assembling. Self-assembling allows the molecules to respond with different configurations to external stimuli, like the pH change [37]. Often these self-assembling molecules were discovered by chance [37].

Nowadays, scientist use self-assembling to build regular nanofibers or structures with certain functions like channels through a lipid bilayer, which build cell membranes [71]. If the assembling mechanisms are understood, there are two concepts to obtain a structure with a certain functionality. Either molecules with the wanted function are modified such that they self-assemble in the desired way, or molecules that already assemble in the desired way are modified with groups to adapt the functionality [37].

However, the versatility of this method is limited as especially the variety of structures is restricted by the assembling mechanisms. Furthermore, the resulting structure of modified molecules is difficult to predict [37]. Other methods allow a high freedom of design but work on a macroscopic length scale like 3D extrusion printing of cellulose acetate [36,72], or they only allow indirect structuring by adding the desired material to a structure out of conventional material. Such scaffolds are often fabricated by photolithography methods that allow a high freedom of design and small feature sizes.

A direct processing of some biomaterials with light is possible in 2D. For example, with very short UV laser pulses a biomaterial is transferred to a substrate [32]. Here, the biomaterial is ablated from one substrate and deposited onto another substrate. Another possibility in 2D is a light induced radical polymerization reaction that is possible with corresponding substitution reactions and initiators [33]. The substitution reactions replace functional groups by groups that enable the radical polymerization, like methacrylic groups (cf. Sec. 4.2). Afterwards, these molecules can be cross-linked in a reaction with an initiator. These initiators may be biological initiators, like coumarin [33].

These methods are yet limited to 2D patterning. However, the radical polymerization process is suitable for direct laser writing (see next section), which allows an expansion to 3D structuring.

3.2 Direct Laser Writing

Direct laser writing (short: DLW) is a lithography method in which a change in the material properties is induced by a multiphoton absorption process, often a two-photon absorption (2PA). Due to the often used 2PA, it is also called two-photon lithography. It allows fabrication of nearly arbitrary 3D structures. The size of the features of these structures ranges from several micrometers down to the nanometer length scale [73]. Therefore, it is entitled with 3D microprinting, too. The first realization of DLW succeeded in the 90s [29,30].

The exact mechanisms and different details of DLW are explained in this section step by step. Section 3.2.1 allows the reader to get an idea of a typical setup for DLW. Afterwards, the physical (Sec. 3.2.2) and chemical mechanisms (Sec. 3.2.3) are explained, and in the end some possibilities for optimization (Sec. 3.2.4) are introduced briefly.

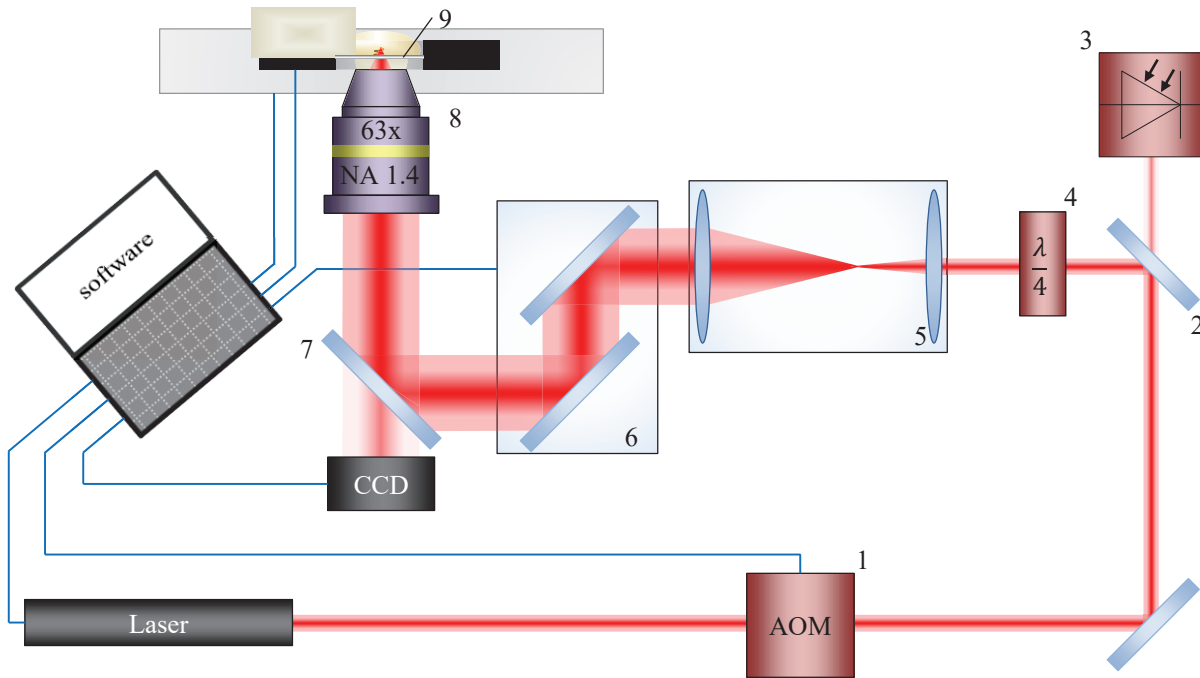


Figure 3.1: Setup for direct laser writing: The power of the laser beam is modulated with an acousto-optical modulator (1) and calibrated with a photodiode (3) behind a partially transparent mirror (2). The linearly polarized laser light is converted into circularly polarized light by a quarter wave plate (4). The expanded beam (5) can be deflected by a pair of galvanometric mirrors (6) before it is coupled with an dichroic mirror (7) into an inverse microscope. Here, an objective (8) focuses the beam into the resist on a substrate (9). After [78,79].

3.2.1 Technical realization

A schematic DLW setup is presented in Figure 3.1. The scheme outlines the setting of a commercial system from Nanoscribe GmbH, which is used for the work presented later on. There are other possible realizations, for example with other laser wavelengths [74, 75] or with additional beam control [76,77], which may lead to finer features and higher resolution (cf. Sec. 3.2.4).

Here, a laser with a central wavelength of $\lambda = 780\text{nm}$, a pulse duration of $\tau = 100\text{fs}$ and a repetition rate of $f = 80\text{MHz}$ is used [80]. An acousto-optical modulator (short: AOM; (1) in Fig. 3.1) adjusts the power by refracting part of the light out of the original direction. The intensity change is calibrated to the voltage applied at the AOM before the actual writing process with a photo detector ((3) in Fig. 3.1) behind a partially transparent mirror (2). A $\lambda/4$ -waveplate ((4) in Fig. 3.1) converts the linearly polarized light into circularly polarized light to achieve a symmetric lateral beam profile in the focal point.

After the beam is circularly polarized, it is expanded by a telescope ((5) in Fig. 3.1) before it passes a pair of galvanometric mirrors ((6) in Fig. 3.1). These mirrors can be used to move the beam through the resist, for further information, see below. By a dichroic mirror (7), light is guided into an inverted microscope. The inverted microscope contains

3. Methods

a focusing objective with a high numerical aperture ($NA = 1.4$; (8) in Fig. 3.1) and a substrate (9) with the resist. Through the objective, light is guided into the resist.

During the writing process, the refractive index of the resist may change. Therefore, the transmittance of light from a light source in the inverted microscope changes. The transmitted light is collected with the objective ((8) in Fig. 3.1) and transmitted through the dichroic mirror (7) onto a CCD camera. Thus, the changes in the transmitted light and, therefore, the writing process can be observed, if the refractive index change is large enough.

There are different printing modes that differ in the medium the objective is in contact with. In the air configuration the resist is either on top or bottom of the glass substrate but not in contact with the objective. This method leads to spherical aberrations which depend on the axial position of the focal point and change with the position of the focal point in the resist. The air configuration limits the height of the structures due to the working distance of the objective and is limited to objectives with a low numerical aperture ($NA \approx 0.5$). [80]

To use objectives with a higher numerical aperture, an immersion oil can be used. The immersion oil has the same refractive index as the objective and the glass substrate. The resist is dropped on top of the glass substrate. This method is called oil immersion configuration or conventional DLW. The size of the structures is limited by the difference between the working distance of the objective and the thickness of the substrate. The aberrations still increase with the axial distance of the focus from the glass substrate inside the resist and, especially, with a beam propagation through processed material. [80]

Constant and only small spherical aberrations are achieved with the so-called dip-in configuration. Here, the resist is applied to the bottom of the substrate and the objective is directly dipped into the resist that has a refractive index matching to that of the objective lens. This also allows to fabricate very tall structures, since the objective can be moved away from the substrate without the limitation of the objective's working distance. In addition to the matching refractive index, only resists that do not damage the objective should be selected. [80]

For resists that contain solvents that may damage the objective, like the resists presented in Chapter 4, the oil immersion configuration is advisable. In all printing configurations, clean glass substrates are needed that are perfectly plane parallel or with minimal irregularities, such that a horizontal layer of the printed material will end up completely connected to the substrate. A pre-treatment of the glass substrates may further improve the performance, e.g., by depositing an adhesive layer between glass and resist.

As mentioned above, the galvanometric mirrors can be used to move the focus through the resist. A shift of the focus point is achieved by tilting the galvanometer mirrors and hence, deflecting the beam. A relative movement between the focus and the resist can be achieved by moving the substrate with the resist itself, too. Therefore, either the microscope stage or a piezoelectric stage on top of the microscope stage are used. Hence, there

are three modes to move substrate and beam relatively to each other: the “galvo-scan-mode”, the “stage-scan-mode”, and the “piezo-scan-mode”. In all cases, the piezoelectric stage provides the axial movement of the sample.

The piezo actuator achieves the highest accuracy, while the galvanometric mirrors allow the highest writing speeds and the microscope stage enables the largest writing area without further steps [80].

The processes happening inside the resist during DLW are explained in the following two sections.

3.2.2 Physical process

In common photolithography the chemical process described in Section 3.2.3 starts with a molecule absorbing one photon with high energy (mainly UV light). This molecule is excited into a state E (cf. Fig. 3.2 (a) blue) and then becomes reactive through intersystem crossing, a radiationless transition between different states, and starts a chain reaction, e.g., a polymerization.

For lithography with one-photon absorption (1PA), the intensity decreases with increasing writing depth in the material due to absorption, resulting in non-uniform excitation along the beam. All along the trajectory of the laser beam through the resist the reaction takes place till the penetration depth is reached and the intensity is no longer sufficient to stimulate polymerization. To a limited amount, the axial feature size of the structures can be influenced by the precise control of the exposure dose and thus the penetration depth. This is done in the so-called gray scale lithography [81]. A proper limitation of the reactive volume exists only in the lateral direction perpendicular to the beam propagation.

In the case of DLW or two-photon lithography, the energy of one photon of the used wavelength does not suffice to excite a molecule into the excited state E (cf. Fig. 3.2 (a)). Hence, without scattering the resist is transparent for the used wavelength, this leads to a constant intensity independent of the writing depth. This means, at least two photons have to be absorbed at the “same” time for an excitation. This 2PA is a nonlinear process, which was first predicted by M. Göppert-Mayer [84] and later on experimentally proven by W. Kaiser [85].

A very descriptive explanation for the 2PA results from the Heisenberg uncertainty principle of time and energy [86]. Due to the uncertainty principle, there exists a virtual state between the actual states for a short time $\Delta t \geq \frac{1}{4\pi} \Delta \nu$ [86, 87]. A molecule can be excited to the real state using this virtual state by absorbing two photons within a time interval shorter than the lifetime of this imaginary state. The first photon excites the molecule to the virtual state and the second photon excites the molecule from the virtual state to the excited state E (cf. Fig. 3.2 (a)).

Furthermore, the 2PA process can be derived from perturbation theory [84, 88]. This, as well as the explanation with the Heisenberg uncertainty principle, results in a very

3. Methods

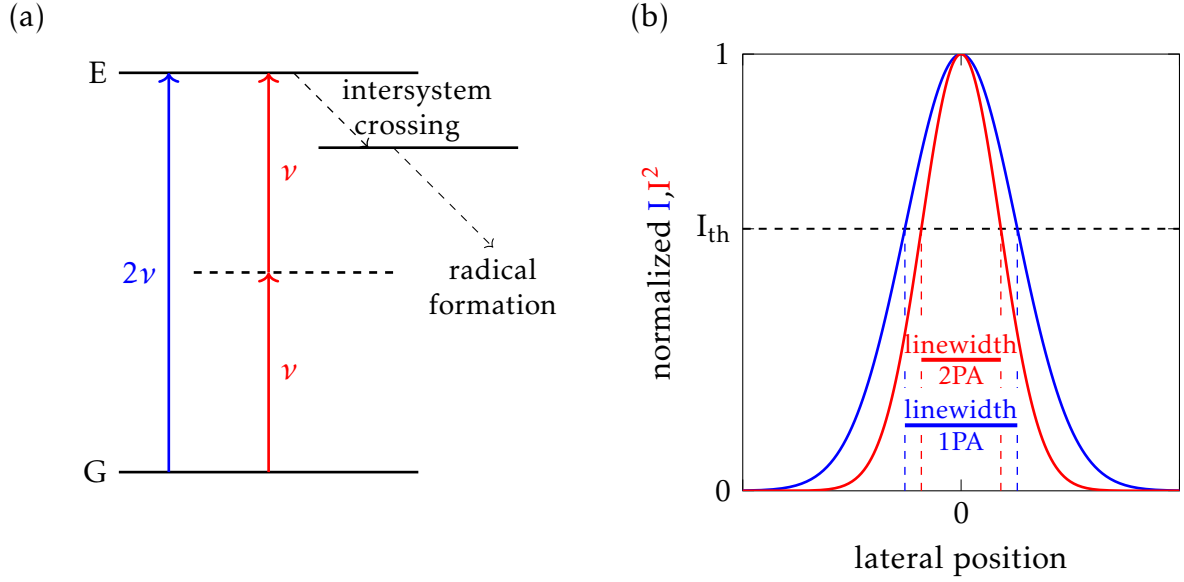


Figure 3.2: Schema of the two-photon absorption (2PA) process and the physical voxel: (a) The 2PA can be explained by the excitation first into an imaginary state (dashed line) and then to the excited state (E). If a direct excitation into the excited state with one-photon absorption (1PA) is possible, it requires light with double the energy (blue). (b) The resulting linewidth after 1PA (blue) and 2PA (red) due to the different dependencies on the electric field intensity with the threshold intensity I_{th} , which is necessary to start the polymerization. After [82, 83].

small probability for this process, which is expressed by the 2PA cross section. The 2PA cross section relates to the energy or the frequency of the used light source ω , the line shape function of the transition $g(2\hbar\omega)$, and the transition tensor $\overleftrightarrow{T}_{G \rightarrow E}$ describing the probability for such a 2PA at the molecular level [89, 90]

$$\sigma_{2PA} \propto (\hbar\omega)^2 g(2\hbar\omega) |\overleftrightarrow{T}_{G \rightarrow E}|. \quad (3.1)$$

The transition tensor $\overleftrightarrow{T}_{G \rightarrow E}$ considers a potential polarization-dependence. The values of the mean 2PA cross section are in the range of $10^{-58} \frac{\text{m}^4\text{s}}{\text{photon}} = 1 \text{ GP}$ (in words: one Göppert-Mayer) [88, 90–92].

In the macroscopic description, 2PA is a nonlinear process that is included in the dependence of the polarization \vec{P} from higher orders of the electric field \vec{E} :

$$\vec{P} = \epsilon_0 \sum_j \overleftrightarrow{\chi}^{(j)} \vec{E}^j, \quad (3.2)$$

with the linear and nonlinear susceptibilities $\overleftrightarrow{\chi}^{(j)}$ [88]. 2PA is a third order process, thus, the 2PA cross section, as an absorptive process, is part of the imaginary part of the third order susceptibility $\overleftrightarrow{\chi}^{(3)}$.

If the electric field induces a nonlinear polarization due to the third order susceptibility, the corresponding energy $W^{(3)}$ of the induced dipole in the electric field is:

$$\begin{aligned} W^{(3)} &= \vec{P}^{(3)} \vec{E} \\ &= \epsilon_0 \overleftrightarrow{\chi}^{(3)} \vec{E}^4. \end{aligned} \quad (3.3)$$

This energy is proportional to the fourth order of the electric field and, hence, to the second order of the intensity of the electromagnetic field.

Because of the small cross section values, 2PA mainly occurs in the focal volume of the beam, where the probability for 2PA is not negligible due to the high intensity. If scattering occurs in the used wavelength range, the intensity in the focal volume decreases and, hence, the probability for 2PA.

The focal volume is the smallest exposed volume element in the DLW process. In consideration of the chemical effects discussed in Section 3.2.3, which lead to a threshold for the reaction process, the focal volume leads to the smallest fabricable unit, the so-called volume pixel or voxel [17].

The lateral size of such a voxel is smaller than for a comparable 1PA process as indicated in Figure 3.2 (b). If a normalized intensity is considered with a threshold, for both 1PA and 2PA, at $I_{\text{th}} = 0.5$, then, due to the dependencies of the energy on either I or I^2 , the voxel size ($I > 0.5$ or $I^2 > 0.5$) is smaller for the 2PA (red bar in Fig. 3.2 (b)) than for 1PA.

Most of the materials that show 2PA can be excited with 1PA at a higher frequency as indicated in Figure 3.2 (a). In some cases 2PA allows the optical transition for a dipole forbidden transition, hence, there is no 1PA but there can be 2PA.

With the 2PA a chemical reaction is started that leads to a change in the solubility of the material. The resulting chemical process is discussed in the next section.

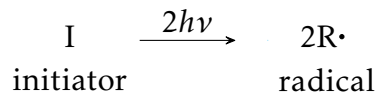
3.2.3 Chemical process

There are different kinds of reactions that allow a 3D structuring and are initiated by 2PA (see Sec. 3.2.2). A very common reaction mechanism is the radical polymerization, but also acid generation reactions are established [93, 94]. Furthermore, inorganic materials can be patterned with 2PA, e.g., metals [93, 95, 96], using other reaction mechanisms.

In the course of this work, methacrylated cellulose derivatives (cf. Sec. 4.1) are used and a radical polymerization addresses acrylic and methacrylic groups of monomers. Therefore, the explanation in this section focuses on the radical polymerization reaction.

A radical polymerization proceeds in three steps [29] that may look like:

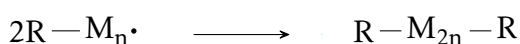
(i) the starting reaction:



(ii) the chain reaction:



(iii) the termination reaction:



3. Methods

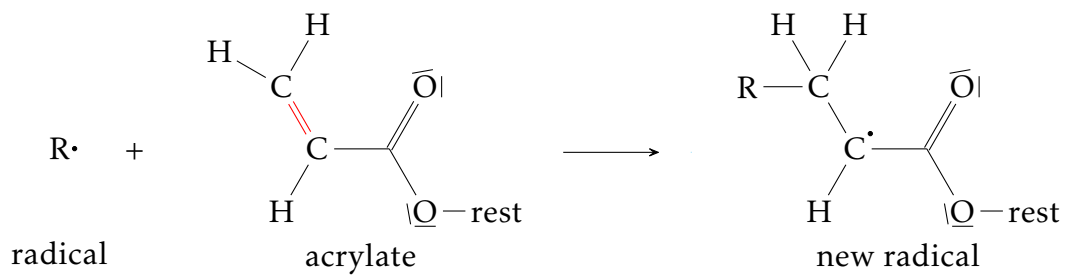


Figure 3.3: Polymerization reaction of an acrylate: The carbon double bond (red) is cracked open and the radical is attached to one carbon atom leaving the second carbon atom unsaturated.

During the starting reaction (i), an initiator is excited via 2PA. After the excitation, the process is the same as for one-photon polymerization: The initiator itself can become a reactive species or the energy can be transferred to another molecule, which is then included in the further reaction process. For resists without further energy transfer, the excited initiator molecule relaxes into the lowest vibrational state or the first singlet excited state within less than picoseconds. A further relaxation into the lowest triplet state via intersystem crossing is possible. From the singlet state or the triplet state the actual reaction starts (cf. Fig. 3.2 (a)). [93]

The excited initiator splits into two radicals via a photocleavage process, as in reaction (i), or the initiator becomes reactive due to the excitation and reacts with another molecule under hydrogen abstraction to build radicals [97]. In any case, as a result of the starting reaction, radicals occur in the illuminated focal volume. For the further reaction process (reactions (ii) and (iii)) no more light is needed, if there are no or at least only few interfering processes.

The second reaction step is the actual chain reaction (ii). Here, a radical reacts with a monomer. The result is a larger radical that includes the former radical and a monomer. This new radical starts the chain building reaction again. The exact reaction mechanism and resulting molecular structure depends on the monomer and the initiator. Therefore, not all possibilities are explained here.

For the used methacrylated cellulose derivatives, the reaction mechanism is similar to the mechanism involving acrylates, which are common types of monomers in photolithography [97]. The acrylic group exhibits a carbon double bond (red in Fig. 3.3). During the reaction with a radical this double bond is cracked open and the radical is attached to the carbon atom. This leaves the other carbon atom of the former double bond unsaturated as sketched in Figure 3.3 [97]. The properties of the final material are not influenced by these acrylic groups but by the polymer backbone of the material [97].

In principle, this chain reaction can proceed endlessly as long as there are acrylic groups, which can attach to the radical. In reality, there are different conditions and reactions that hinder a proceeding of the chain reaction, like the termination reaction (iii). In this termination reaction, a radical reacts with another radical by bonding the unsaturated atoms.

More frequently, the radical polymerization reaction is terminated by reactions with oxygen [74, 98]. Oxygen can already interfere during the starting reaction (i) by depopulating the excited states of the initiators. This means, the excited states of the initiators are quenched by oxygen [99]. Hence, no cleavage process occurs. Another possibility is a reaction of oxygen with the radicals. This scavenging hinders the radical polymerization, too [99].

The reactions with oxygen lead to a threshold for the necessary laser power analog to the Schwarzschild threshold in photography or 2D lithography [74, 99, 100]. The laser power must exceed a certain level to start an adequate number of chain reactions to achieve a satisfying polymerization.

The effect of oxygen is increased compared to UV lithography of large areas due to the diffusion of oxygen inside the excited volume from the surrounding resist. If large areas are excited with UV light, the oxygen is consumed in the whole area instead of only in a small volume. Besides the diffusion of oxygen into the excited volume, there is the diffusion of radicals out of the excited volume. This enlarges the polymerized volume.

This polymerized volume defines the voxel mentioned in Section 3.2.2. The difference between the excited volume and the actual voxel size is defined by the reaction kinetics and the mobility of the molecules in the resist. For fast reactions or low mobility the voxel will correspond to the excited volume.

The timescale of the diffusion of the radicals is noticeable longer than the excitation time [74]. If another feature is written in close proximity to the already excited area while there are still radicals, these radicals may lead to polymerization between neighboring features. This is called proximity effect as the features are written in temporal and spatial proximity to each other. Although this may smooth written structures, it is of disadvantage for high resolution and fine features. [101]

The proximity effect is reduced by increasing the temporal delay between neighboring features. Other obstacles in DLW may be overcome by some of the optimization steps presented in the next section.

3.2.4 Optimization

The above mentioned setup (cf. Sec. 3.2.1) already contains one element to improve the quality of the process: The $\lambda/4$ -plate leads to a symmetric intensity distribution in the focal volume and, hence, a symmetric voxel. There are more and often more complex methods to further improve the process of DLW that may be required to achieve high resolution or fast processing. Since we want to give a proof of principle of DLW with a new material class in this work these optimizations are not essential. Therefore, this section will only introduce very briefly a selection of methods for optimization.

A first method for optimization is inspired by the stimulated emission depletion (short: STED) microscopy [102], which was awarded with the Nobel prize in 2014. In STED assisted DLW, a second laser is used to deplete the excited molecules before they reach the

3. Methods

reactive state. To do so, the two laser beams are spatially overlaid. As for the microscopy method, a typical beam profile combination is the excitation with a Gaussian beam and the depletion with a so-called doughnut mode, which has zero intensity in the middle. By combining these two, the middle, where the maximum excitation takes place, stays excited and is not depleted, while the outer regions of the Gaussian beam are excited by the first laser and depleted by the STED laser.

Also similar to the microscopy method, the two lasers have to use different wavelength ranges, so the STED laser does not further excite the molecules in the photoresist. The STED laser has to work at a wavelength that enables a depletion process. This depends on the material system and the possible states that can be addressed for the depletion process. [82,103]

The above mentioned beam shapes that can be used for the STED assisted DLW are distorted due to aberrations. Therefore, a further optimization can be achieved if these aberrations are corrected [104]. This already improves the performance without STED [76] when applied for the excitation laser. The aberration correction can be achieved with a spatial light modulator (SLM). Phase and amplitude patterns loaded onto the SLM display diffract the beam such that the achieved beam profile is optimized. [105].

These are just examples for optimization of the DLW method. There are more possibilities already and research is still in progress to further improve DLW.

Chapter 4

Direct laser writing in a bioinspired material

While conventional photoresists for DLW use mineral oil-based monomers or polymers as their key component [106], the resists presented here use a natural polysaccharide as a raw material. With the focus of Chapter 5 on photonic structures in insects that use chitin as main material, chitin is of course highly interesting. However, substitution reactions of chitin are more complex than for example cellulose substitution reactions. Hence, to introduce polysaccharide-based photoresists in DLW cellulose is used. The monomers in conventional photoresists are replaced by derivatives of cellulose as the crucial component of the resists. The gained information can be transferred to chitin later on.

Therefore, the first section introduces cellulose as a promising material. The substitution reactions that are necessary to convert cellulose into a cross-linkable constituent of a photoresist are explained in Section 4.2 as well as the other constituents of a potential resist. In the subsequent Section 4.3, the properties of a cellulose-based resist are discussed before in Section 4.4 a first biomimetic structure is fabricated with a such a resist.

4.1 Cellulose - a short profile

Cellulose is the most abundant polysaccharide in the world [107]. It can be extracted out of cell walls in plants and it can be produced by some bacteria [107]. It is a renewable raw material with nearly inexhaustible occurrence in the world. Therefore, it is a cheap and sustainable material, which takes a major role in the development of green chemistry [108].

The use of cellulose is much older than its name (1839) and the knowledge of its molecular formula (1838). Mankind has always used cellulose, for example as building material, energy source or clothing. The use of cellulose, as a chemical raw material, started in the 19th century with the synthesis of Celluloid. [107]

4. Direct laser writing in a bioinspired material

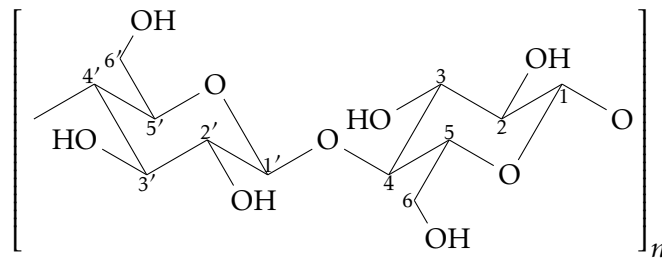


Figure 4.1: The cellobiose is the repeating unit of the cellulose. It consists of two β -D-glucose molecules linked via a $\beta(1,4)$ -glucosidic linkage.

Cellulose is biocompatible and, in its pure form, it is hydrophobic and insoluble in most organic solvents [107]. It is part of many natural composite materials in plants. These natural composite materials show a high tensile strength, which increases with an increasing amount of cellulose [109]. Concerning the tensile strength, these composites outperform some synthetic polymers. For example, pineapple leaf fibers have a tensile strength of up to 1627 MPa [109], while poly(methyl methacrylate) (PMMA), which is used for implants in dentistry [110] or as roofing material, has a tensile strength of less than 100 MPa [111].

The above mentioned properties of cellulose arise from the exact molecular structure of the cellulose. Cellulose consists of a chain of glucose molecules that are linked by a β -(1,4)-glycosidic bond. This means that two neighboring β -D-glucose molecules are linked via the first carbon atom of one glucose molecule and the fourth carbon atom of the neighboring molecule (see Fig. 4.1). This fundamental unit cell, the cellobiose, is around 1 nm long [112].

Each β -D-glucose molecule of the cellobiose exhibits three hydroxyl groups. These hydroxyl groups build hydrogen bonds, which determine the physical and chemical properties. Due to intramolecular hydrogen bonds, the cellulose molecules exhibit a linear structure [107] and due to intermolecular hydrogen bonds the cellulose is insoluble in common organic solvents and materials with a high cellulose amount have a high tensile strength.

If the molecular arrangement is changed, as in case of the amylose, an isomer of the cellulose and a constituent from starch [113], the chemical, physical and biological properties differ enormously. The amylose also consists of a chain of glucose molecules, which are linked by α -1,4-glycosidic bond [113].

Besides the exact arrangement, the so-called degree of polymerization DP , the total amount of fundamental units building a cellulose molecule, influences the exact properties. The degree of polymerization depends on the exact source of the material and varies between around $DP = 500$ to $DP = 5000$.

The properties of the cellulose can be adapted, if the molecules are for example shortened or if the hydroxyl groups are substituted with other functional groups. These functional groups are changed during substitution reactions and can enable solubility in common

organic solvents, like acetone, or certain reaction mechanisms, like radical polymerization. This allows DLW of a cellulose-based material. The composition of such a resist is explained in the following section, including the substitution reactions that enable DLW with a cellulose derivative.

4.2 Components of a bio-resist

For photolithography with a radical polymerization, a monomer has to be radicalized either by a direct excitation or by an excited initiator. Many photoresist for DLW contain a monomer and an initiator for the chain building reaction.

Here, different methacrylated cellulose derivatives are investigated as potential monomers. The cellulose derivatives are actually relatively short polymers and no monomers in the classic sense of a single unit cell. The different types of cellulose derivatives and their synthesis are explained in the first subsection. As the methacrylic group can not be excited by 2PA itself, an additional initiator is needed as in most common resists. Therefore, different initiators have been examined (cf. Sec. 4.2.2) for their suitability of starting the polymerization of the methacrylated cellulose derivatives after 2PA or other, higher nonlinear absorption processes.

The cellulose-based resists need a solvent as a third component, because the cellulose derivatives and the initiators are solids. Two possible solvents are compared in Section 4.2.3 and their advantages and disadvantages are discussed. Besides the two discussed solvents, there are a lot of other possibilities, as for the other components. Due to the amount of possible components, only a selection is presented.

The synthesis of the cellulose derivatives is done by M. Rothammer at Campus Straubing from Technical University Munich as well as the Fourier-transform infrared (short: FTIR) spectra in Section 4.2.1. Some investigation concerning the properties of the resists were done in close cooperation with A. Koerfer. In both cases, corresponding paragraphs are cited.

4.2.1 Cellulose-based monomers

Cellulose-based molecules are tested as monomers for a resist that is suitable for DLW. These short polymers are cross-linked to built larger units. To enable the corresponding reaction process, the cellulose is equipped with different functional groups replacing the hydroxyl groups during substitution reactions, at least partially. The number of hydroxyl groups that is replaced by a certain functional group at a single glucose unit defines the degree of substitution DS . If one hydroxyl group per glucose unit is replaced, the degree of substitution equals one ($DS = 1$).

Three kinds of cellulose-based polymers are examined. Their synthesis is done by our cooperation partners within the priority program Tailored Disorder and contains the work of M. Rothammer [114], as especially the substitution reactions of cellulose are

4. Direct laser writing in a bioinspired material

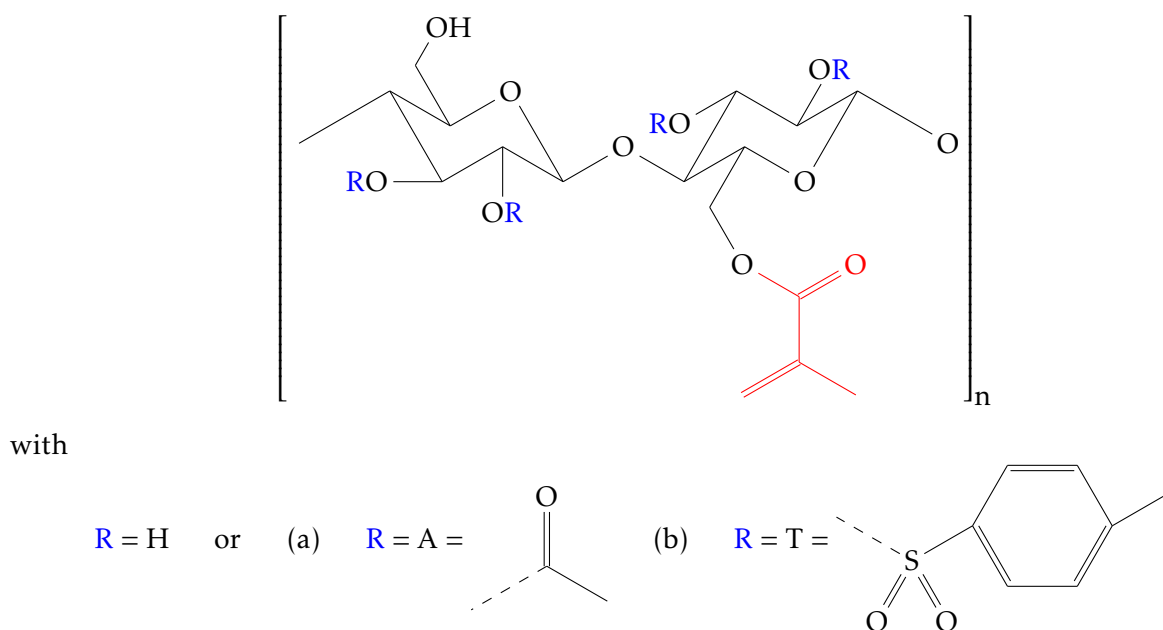


Figure 4.2: Chemical structure of (a) methacrylated cellulose acetate (MACA) and (b) methacrylated tosylcellulose (MATC): The methacrylic groups (MA) (red) enable cross-linking via radical polymerization, while the (a) acetate groups (A) or (b) tosyl groups (T) allow solving the cellulose derivatives in common organic solvents.

not yet completely understood [107] and an additional field of investigation. The cellulose derivatives differ in their kind and number of functional groups as well as in their molecular length, which influences the properties and capabilities of the resists.

To enable the radical polymerization of the material as described in Section 3.2.3 with an initiator, methacrylic groups (short: MA) (cf. Fig. 4.2 red) are used in all cases. Hence, some of the hydroxyl groups are replaced by methacrylic groups ($DS(MA) \leq 0.5$). The solubility in common organic solvents, like acetone and dimethyl sulfoxid (cf. Sec. 4.2.3), is enabled by two different functional groups. A first group of polymers uses acetate groups (short A; $DS(A) \leq 2.5$; cf. Fig. 4.2 (a)) to achieve solubility. The second approach enables the solubility with tosyl groups (short T; $DS(T) = 0.85$; cf. Fig. 4.2 (b)). The resulting repeating units of methacrylated cellulose acetate (MACA) and methacrylated tosylcellulose (MATC) are sketched in Figure 4.2.

Synthesis of the monomers

The synthesis of the first kind of MACA with 500 units of glucose (MACA500) is started with a commercially available pure cellulose diacetate ($DP = 500$, $DS(A) \leq 2.5$; by Carl Roth GmbH & Co. KG). Under permanent stirring the cellulose diacetate, which is in general the product of an esterification [107], is dissolved in dimethylformamide (by VWR International GmbH) and heated to 120°C . At this temperature methacrylic acid anhydride (by Sigma-Aldrich Chemie GmbH) and pyridine (by Alfa Aesar by Thermo Fisher GmbH) are added and during five hours of permanent stirring the substitution reaction takes place ($DS(MA) = 0.5$). In the end, the MACA500 is precipitated with the help of

Table 4.1: Degree of substitution (*DS*) for methacrylic (MA) and acetate (A) or tosyl (T) groups of the cellulose derivatives and their molecular mass and length. [115, 116]

	degree of substitution <i>DS</i>		molecular mass m_{mol}		length
	MA	A or T	in u	in $\frac{\text{kg}}{\text{mol}}$	in nm
MACA15	0.33	< 2	4030 ¹	4.03	7.5
MACA500	0.5	≤ 2.5	140000 ²	140	250
MATC15	unknown	< 0.85	4730 ³	4.73	7.5

ethanol (by Carl Roth GmbH & Co. KG) and, afterwards, washed. The final white, solid MACA500 is obtained after evaporation of the solvent. [115]

The second kind of MACA and the used MATC contain only around 15 units of glucose (MACA15 and MATC15, respectively). They are synthesized from micro crystalline cellulose ($DP = 230$ to $DP = 240$; by Merck KGaA), which is decomposed with phosphoric acid at room temperature over six weeks. For MACA15, the decomposed cellulose is then methacrylated, analogously to the MACA500, with methacrylic acid anhydride. Afterwards, the methacrylated cellulose is added to acetic acid (by Th. Geyer GmbH & Co. KG) and stirred at room temperature over one hour. Then, acetic anhydride (by Th. Geyer GmbH & Co. KG) and additional acetic acid are added. The mixture is stirred at 55 °C until everything is dissolved and the methacrylated cellulose is acetylated. It is not known, to which extent the acetate groups replace hydroxyl groups, nor, if they replace methacrylic groups. Our cooperation partners estimate the degree of substitution of the acetate groups to be $DS(A) < 2$ due to solubility properties and for the methacrylic groups $DS(MA) = 0.33$ (cf. Tab. 4.1). The processing is finished with a precipitation and washing of the derivative with ethanol, as for the MACA500. [116]

For the last cellulose derivative, the decomposed cellulose is dried and, afterwards, suspended in dimethylacetamide (short: DMAc; by Carl Roth GmbH & Co. KG). This suspension is flushed with Argon for ten minutes. Under elimination of air moisture the suspension is stirred at room temperature for two hours and further stirred at 100 °C for 45 min. After the addition of dried LiCl (by VWR International GmbH), the mixture is stirred for another ten minutes, before it is gradually cooled to room temperature. Then, triethylamine (by Acros Organics B.V.B.A.) solved in DMAc is added under stirring. The mixture is cooled down to 8 °C, before toluenesulfonic acid chloride (by Alfa Aesar by Thermo Fisher GmbH) solved in DMAc is added dropwise. After another 24h of stirring at 8 °C the processing is finished with a precipitation and washing of the derivative with ethanol. After the tosylation the cellulose derivative is methacrylated analogously to MACA15 and MACA500. [116]

¹Considering $DS(A) = 2$ and $DS(MA) = 0.33$.

²Considering $DS(A) = 2$ and $DS(MA) = 0.5$.

³Considering $DS(T) = 0.85$ and $DS(MA) = 0.33$.

4. Direct laser writing in a bioinspired material

For the MATC15 the degree of substitution of the tosyl groups is estimated to be, as for the pure tosylcellulose, $DS(T) < 0.85$ (cf. Tab. 4.1). The degree of substitution of the methacrylic groups is not known. [116]

Properties of the monomers

With the degree of substitution for the different functional groups, given in Table 4.1, and the assumption of a negligible mass loss due to the binding energy of the atoms, the mass of the different cellulose derivatives can be estimated (cf. Table 4.1). This is done by simply adding the atomic masses of the single atoms.

Besides the mass of the derivatives, an estimation of the molecular lengths of the derivatives is possible. With a length of around 0.5 nm of a single glucose unit the maximum length of the derivatives is given by their degree of polymerization and listed in Table 4.1. These theoretical lengths are only achieved, if the molecules remain in the linear form of a pure cellulose molecule. The theoretical length and the mass of the molecules are helpful to discuss the performance of the resists with the different derivatives or the viscosity of solutions with the cellulose derivatives later on.

The solubility of the different cellulose derivatives depends on the degree of substitution (cf. Tab. 4.1) of the acetate or tosyl groups [117]. The $DS(A)$ is highest for the MACA500. However, solutions with more than 25 wt% of MACA500 can not be processed because of their high viscosity.

For mixtures with identical mass proportions of MACA500, MACA15, and MATC15, the mixture with MACA500 has the highest viscosity due to the high molar mass of MACA500 [118, 119]. The viscosity of the mixtures with MACA15 and MATC15 with identical mass fractions are comparable.

These differences in the solubility and viscosity of the different cellulose derivatives and their solutions demand different proportions of the cellulose derivatives compared to the solvent for the further investigations and the use in DLW (cf. Tab. 4.2).

A first criterion for the suitability of the cellulose derivatives for DLW is their optical behavior in the visible spectral range. 1PA or strong scattering at the wavelength that is used for DLW hinders the fabrication of 3D structures. A 2PA absorption at this wavelength or more precisely the possibility for excitation of radicals with this wavelength would allow DLW without an initiator.

To look at the 1PA and scattering, 1PA spectra of the different cellulose derivatives are measured (cf. Fig. 4.3). Therefore, the spectra of the cellulose derivatives solved in dimethyl sulfoxide (short: DMSO) in a cuvette are measured and normalized to the spectrum of pure DMSO in a cuvette. The cuvettes are fabricated out of UV transmitting fused silica (Suprasil) and the spectra are measured with the spectrophotometer Evolution 220 (by Thermo Scientific Inc.), which is equipped with a xenon flash lamp [120].

None of the cellulose derivatives shows a sharp absorption edge. Such a sharp absorption edge is expected for a material that shows only absorption and no scattering. Character-

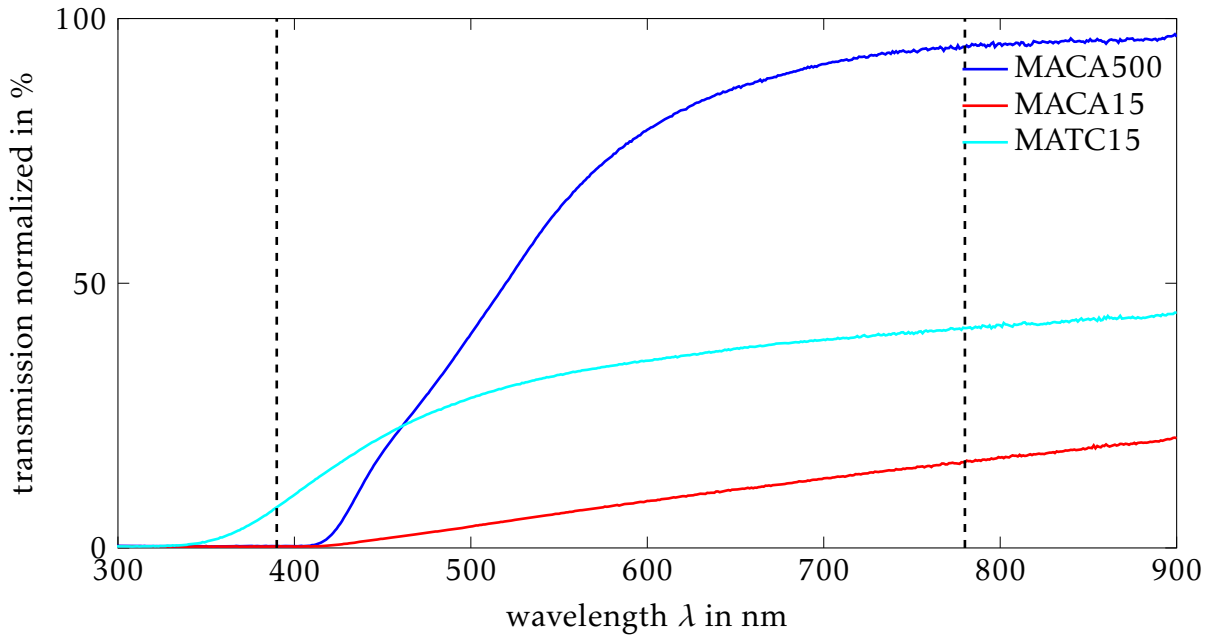


Figure 4.3: 1PA spectra of cellulose derivatives in DMSO with different mass proportions (MACA500 [44] 10.6 wt%, MACA15 [44] 16.7 wt%, and MATC15 9.1 wt%) normalized to pure DMSO.

istic for Rayleigh scattering (cf. Sec. 2.1.3) is a decreasing transmission with decreasing wavelength due to increasing scattering. This is observed for the cellulose derivatives. Here, the transmission increases for wavelength $\lambda \geq 350$ nm.

Only for MACA500 the scattering is negligible for the later used concentrations of cellulose in DMSO (cf. Sec. 4.3) as the transmission at 780 nm is $T \approx 0.94$. For MACA15 and MATC15 most of the light is scattered out of the original direction ($T \leq 0.42$). This is, as mentioned in Section 3.2, a drawback for the use in DLW. For MACA15 and MACA500 light up to a wavelength of 400 nm is absorbed, leaving the possibility for 2PA at 780 nm and a corresponding excitation. However, no 2PA absorption is observed in z-Scan measurements [121, 122]. This disables the use of the cellulose derivatives without initiator.

Beside the visible spectral range, the cellulose derivatives show characteristic spectra in the infrared range shown in Figure 4.4. The spectra of MACA15 (solid red line), MATC15 (solid blue line), and MACA500 (solid cyan line) exhibit characteristic absorption peaks in the transmittance. The peaks at 1634 cm^{-1} , 950 cm^{-1} , and 811 cm^{-1} (black, dotted lines) are assigned to the methacrylic group or more precisely to the stretching vibration and the deformation vibration of the $\text{C} = \text{CH}_2$ -bond of the methacrylic group [115].

For pure cellulose acetate without methacrylic groups, those peaks do not occur (black solid line). During the cross-linking reaction the number of $\text{C} = \text{CH}_2$ bonds is reduced, as they are cracked open, hence, these peaks are reduced or vanish after cross-linking with an initiator under UV exposure (dashed lines) [116]. Analog observations are possible for Raman spectra of direct laser written structures (cf. Sec. 4.3.1).

4. Direct laser writing in a bioinspired material

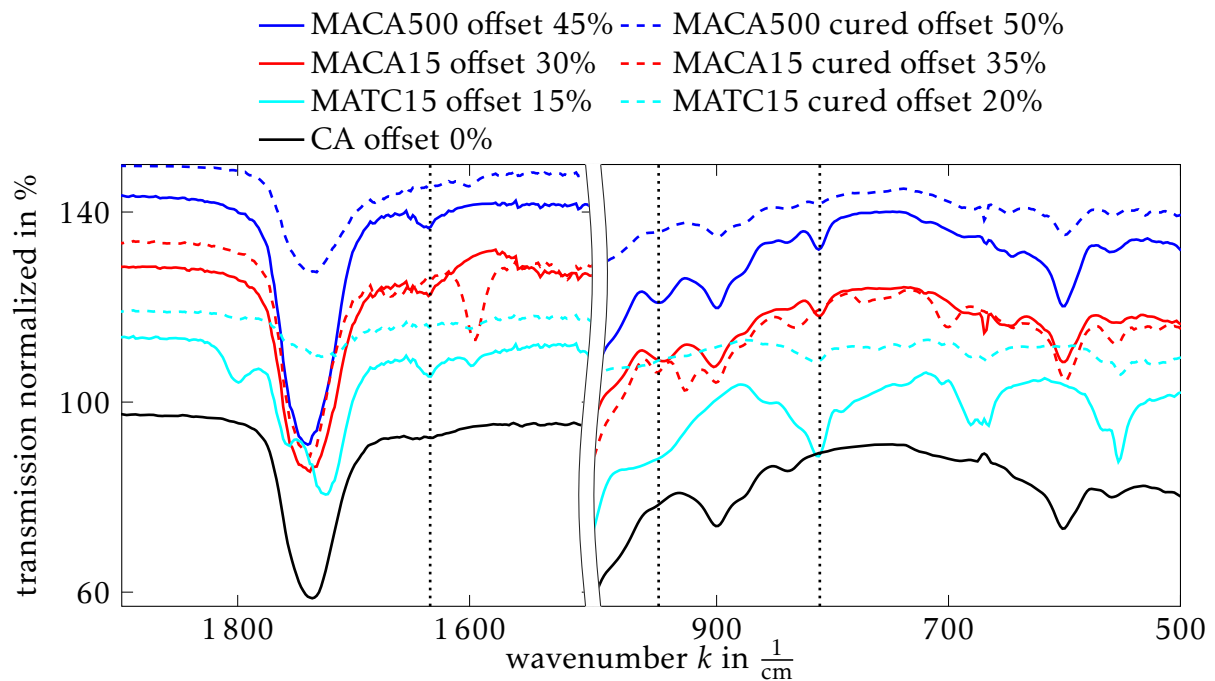


Figure 4.4: FTIR spectra of the uncured and cured MACA500 [115], MACA15 [116], and MATC15 [116] as well as the FTIR spectra of pure cellulose acetate [115]: The FTIR spectra show the characteristic fingerprint of the methacrylic group at 1634cm^{-1} , 950cm^{-1} , and 811cm^{-1} (dotted lines), which are reduced due to the cross-linking or even vanish completely.

With the different functional groups and the given 1PA spectra all three kinds of cellulose are still potential candidates for at least 2D structuring with DLW. As the derivatives do not show 2PA at 780 nm, an additional initiator has to be added to the solution of the different derivatives. Due to the different chemical and physical structure of the derivatives different necessary mixtures and different properties of the resists are expected.

DLW with different cellulose derivatives

Indeed, with all of the derivatives DLW is possible. Scanning electron microscope (SEM) images of fabricated structures are shown in Figure 4.5. These structures are written using different initiators and different mass proportions of the components which are given in Table 4.2.

The used mixtures contain different mass fractions due to the above mentioned solubility and viscosity aspects. Furthermore, they use different initiators as some combinations do not lead to a polymerization at all or show an inferior performance during DLW in comparison to the resists mentioned in Table 4.2. The differences occur mainly due to the different reactivity of the primary initiator radicals towards the cellulose derivatives [123]. The different initiators are discussed in Section 4.2.2.

In the upper row of Figure 4.5, the resolution of the structures achieved with the resists and the 3D performance of the different resists can be compared. For MACA15, a reso-

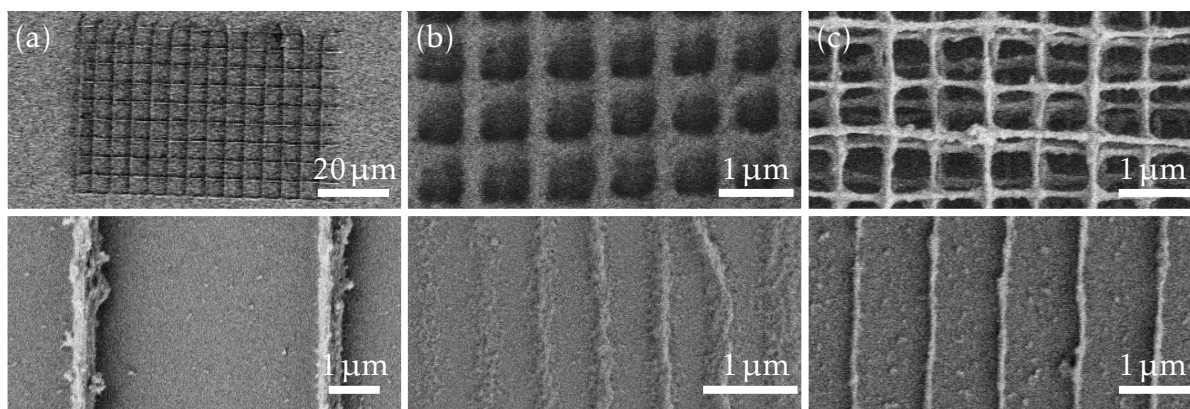


Figure 4.5: SEM images of structures written with (a) MACA15, (b) MATC15, and (c) MACA500: The structures shown in the upper row are intended to show a 3D performance, while the bottom row shows the line qualities. The achieved resolutions are at least $5\mu\text{m}$, $1\mu\text{m}$ and 750nm , respectively and the linewidth reaches down to at least 570nm , 200nm , and 150nm for the different derivatives.

lution of only $5\mu\text{m}$ is achieved and no 3D structuring is possible due to the strong scattering. For MATC15 at least a 2.5D structuring is possible allowing high 2D structures. Concerning the resolution, MATC15 and MACA500 outperform MACA15. Their resolutions are in the same order of magnitude $1\mu\text{m}$ and $0.75\mu\text{m}$ for MATC15 and MACA500, respectively. However, MACA500 enables a clear 3D structuring, while MATC15 only enables high 2D features without a separation of the features in the vertical direction.

Furthermore, the quality of the written structures differs. The bottom row of Figure 4.5 shows SEM images of fabricated lines. These lines are written with an increasing vertical offset to observe lines that are written with the broadest part of the elliptic voxel and not only with the narrow tip of the voxel. This may lead to a slight broadening of the lines, from left to right in the SEM images, with an increasing offset, but it reveals reliable feature sizes.

The lines written in a resist with MACA15 have a feature size of around 570nm (cf. Fig. 4.5 (a) bottom) with some irregularities. MATC15 enables features with a size of around 200nm but with lines that seem to be porous (cf. Fig. 4.5 (b) bottom). The resists with MACA500 exceed the other resists with short cellulose derivatives, if quality and feature size are concerned. The lines written in the resist with MACA500 (cf. Fig. 4.5 (c) bottom) have a features size of around 150nm , while they seem solid and smooth compared to the other structures.

Another criterion is the laser power at different writing speeds that is needed to achieve a polymerization. This power at the threshold is compared for resists that exhibit a initiator concentration that corresponds to 5% of the concentration of the cellulose derivatives in the resist. For a writing speed of $v_w = 10 \frac{\mu\text{m}}{\text{s}}$, MACA500 polymerizes with ITX at a power of only $P = 4.6\text{mW}$. MACA15 and MATC15 need higher laser powers to build stable structures and solid lines. For MATC15 a power of $P = 8.6\text{mW}$ is required and for MACA15 a power of $P = 16.8\text{mW}$ is needed.

4. Direct laser writing in a bioinspired material

Table 4.2: Mass fractions m and relative number of molecules N_{rel} in the different resists

Fig. 4.5 (a) upper row	MACA15	Irgacure369	DMSO
m in wt%	24.0	3.1	73.0
N_{rel}	1	1.4	157.2
Fig. 4.5 (a) bottom row	MACA15	Irgacure369	DMSO
m_{rel} in wt%	33.9	1.3	64.8
N_{rel}	1	0.4	98.8
Fig. 4.5 (b)	MATC15	ITX	DMSO
m_{rel} in wt%	26.3	1.3	72.4
N_{rel}	1	0.9	166.6
Fig. 4.5 (c) upper row	MACA500	ITX	DMSO
m_{rel} in wt%	10.5	1.1	88.4
N_{rel}	1	57.1	15 039.1
Fig. 4.5 (c) bottom row	MACA500	ITX	DMSO
m_{rel} in wt%	10.6	1.0	88.4
N_{rel}	1	51.1	14 912.6

These laser powers for small writing speeds are reached at the used setup for DLW, but higher writing speeds are disabled due to the required high laser powers. The small writing speeds result in disproportionately long fabrication times even for small structures.

A first reason for those required high laser doses is the scattering discussed above. Furthermore, MACA15 and MATC15 consist of much smaller molecules than MACA500. Hence, more MACA15 or MATC15 molecules need to be linked to achieve the same length than for MACA500. In the theoretical case of linear molecules and linear linkage, it needs more than 30 molecules of MACA15 or MATC15 to achieve the length of one MACA500 molecule (cf. Tab. 4.1).

If a statistical clustering of the molecules and a nonlinear cross-linking are considered, the situation is more complicated. In any case, for the MACA15 and MATC15, it needs more methacrylic groups to be radicalized and cross-linked than for MACA500 to achieve the same size of polymerized volume.

The mass fraction of the initiators is high compared to common resist in photolithography, if the fraction of the initiator and the monomer is considered (5 wt% for MACA500 to ≤ 2 wt%) [83,124]. This indicates, that the reaction constant is small and that the quantum yield of the reaction is poor. The molecular compositions of the resists (cf. Tab. 4.2) emphasizes this assumption.

In a common resist with, e.g., pentaerythritol triacrylate (PETA, 98 wt%) and 2-Benzyl-2-(dimethylamino)-4'-morpholinobutyrophenone (Irgacure 369, 2 wt%), there are around 50 monomer molecules on one initiator molecule. For the resist with MACA500 it is the other way around (cf. Tab. 4.2). Assuming that some of the initiator molecules are incorporated into the final polymer backbone, the high initiator content contradicts the

idea of a cellulose-based photoresist. For the resists with MACA15 and MATC15, the relative numbers of molecules N_{rel} are smaller than for resist with MACA500. Therefore, more initiator molecules can start a chain reaction with the MACA500, which leads to a better cross-linking compared to the resists with MACA15 and MATC15 molecules.

A comparably high number of initiator molecules in the resists with short cellulose derivatives compared to the resists with MACA500 leads to resists with a higher mass fraction of initiator than cellulose derivative. Therefore and due to a better performance concerning feature size and quality as well as the resolution, MACA500 is used in the course of this work.

4.2.2 Initializing the polymerization

As mentioned above, the methacrylates as monomers or short polymers do not allow direct excitation via 2PA at 780 nm to start a chain building reaction. Therefore, an initiator is needed (cf. Sec. 3.2.3). In photolithography, different initiators enable a radical polymerization of monomers that exhibit methacrylic groups [97]. For DLW the initiator has to be excitable via a nonlinear absorption process. As there are still a lot of different initiators, only a selection is discussed in the following considering different aspects. The discussed selection of initiators is presented in Table 4.3. All of them are known to cross-link methacrylic groups. The initiators are used without further processing or purification.

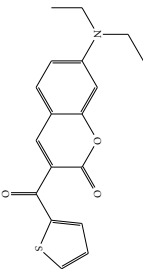
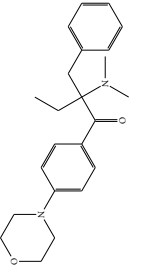
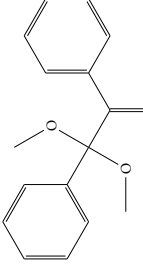
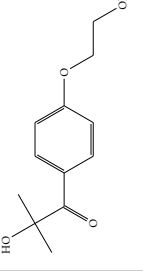
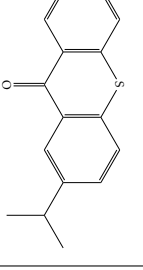
A first step, to see whether a photo-initiator is suitable for DLW, is its 1PA spectra. If 1PA occurs for wavelength $\lambda \leq \lambda_{1PA}$ the most efficient 2PA is expected at $\lambda_{2PA,\text{max}} = \frac{\lambda_{1PA}}{0.7}$ [131, 140], while it can occur for $\lambda_{2PA} \leq \frac{\lambda_{1PA}}{0.5}$, considering that both 1PA and 2PA are possible. Vice versa, if a wavelength of $\lambda = 780\text{ nm}$ is used for DLW and both 1PA and 2PA are possible, 1PA should occur for wavelength $\lambda \leq 0.7 \cdot 780\text{ nm} = 546\text{ nm}$ and it must occur for $\lambda \leq 0.5 \cdot 780\text{ nm} = 390\text{ nm}$. On the other hand, there must not be 1PA for $\lambda \geq 780\text{ nm}$ to avoid excitation with 1PA.

The 1PA spectra of the examined initiators are presented in Figure 4.6. All spectra are measured in the same way as those in Section 4.2.1. The initiators are solved in DMSO and a cuvette filled with DMSO acts as reference for the measurements with the spectrophotometer Evolution 220 (by Thermo Scientific Inc.) with a xenon flash lamp. I651 and I2959 show 1PA for wavelengths smaller than 390 nm, which indicates that there is no 2PA at 780 nm. DETC, I369, and ITX on the other hand show 1PA for wavelengths up to $\lambda = 400\text{ nm}$. Therefore, 2PA at 780 nm is possible.

Hence, a next step is to look directly at the 2PA of these three initiators with the Z-scan method [121, 122]. In a qualitative comparison between DETC, ITX, and I369, DETC shows the largest 2PA cross section and I369 the smallest. All three initiators show a reasonable 2PA cross section that allows DLW.

The highest 2PA cross section, however, does not necessarily correspond to the best performance in DLW, because the 2PA process is only the initial point. The initiator has to

Table 4.3: Examined initiators

name	DETC	Irgacure 369	Irgacure 651	Irgacure 2959	ITX
abbreviation		1369	1651	12959	
CAS number	77820-11-2	119313-12-1	24650-42-8	106797-53-9	5495-84-1
IUPAC name	7-Diethylamino-3-thienylcoumarin	2-Benzyl-2-(dimethylamino)-4'-morpholino-butyrphenone	2,2-Dimethoxy-2-phenylacetophenone	2-Hydroxy-4'-hydroxyethoxy-2-methylpropio-phenone	2-Isopropyl-9H-thioxanthen-9-one
chemical structure					
m_{mol}	327.4 [125]	366.5 [125,126]	256.3 [125,126]	224.3 [125,126]	254.3 [125,126]
mentioned in the context of DLW	[82, 83, 104, 127-129]	[82, 83, 90, 94, 97, 103, 127, 128, 130-136]	[94, 98, 104, 124, 128, 137]	[33, 95, 96, 128, 134, 138, 139]	[82, 83, 94, 103, 129]
purchased from	Acros Organics B.V.B.A.	TCI Deutschland GmbH	TCI Deutschland GmbH	TCI Deutschland GmbH	Sigma-Aldrich Chemie GmbH

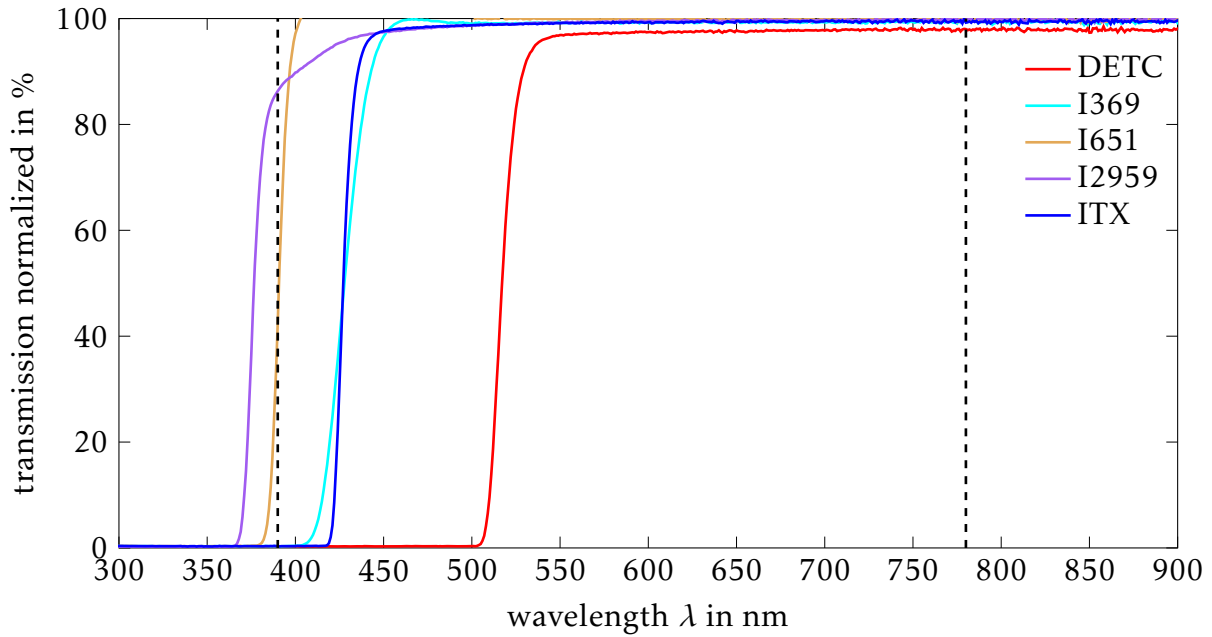


Figure 4.6: 1PA of different photo-initiators: The 1PA is measured for DETC (1.35 wt%), I369 (1.2 wt%), I651 (1.24 wt%), I2959 (2.43 wt%), and ITX (0.73 wt%) solved in DMSO and normalized to pure DMSO.

build a radical that, afterwards, has to react with the cellulose derivatives (cf Sec. 3.2.3). The reaction itself depends on the morphology of the molecules and the radicals.

Hence, DETC, I369, and ITX are tested with MACA500 (cf. Sec. 4.2.1) and DMSO (cf. Sec. 4.2.3) in the DLW process. All initiators enable the DLW process, but the resulting qualities of the structures differ, if resists with equivalent mass fractions (cf. Tab. 4.4) are used. SEM images of the fabricated structures with the best feature quality achieved with the corresponding resists with the different initiators are shown in Figure 4.7.

The structures written with MACA500 and DETC (cf. Fig. 4.7 (a)) are irregular with a lot of polymerized features at the periphery of each line. Spatially terminated structures are achieved with I369 (cf. Fig. 4.7 (b)) which are broad compared to those written with

Table 4.4: Mass fractions m_{rel} and relative number of molecules N_{mol} in the different resists

Fig. 4.7 (a)	MACA500	DETC	DMSO
m_{rel} in wt%	11.0	1.6	87.4
N_{mol}	1	64	14317
Fig. 4.7 (b)	MACA500	I369	DMSO
m_{rel} in wt%	10.5	2.1	87.4
N_{mol}	1	77	14931
Fig. 4.7 (c)	MACA500	ITX	DMSO
m_{rel} in wt%	10.6	1.0	88.4
N_{mol}	1	51	14913

4. Direct laser writing in a bioinspired material

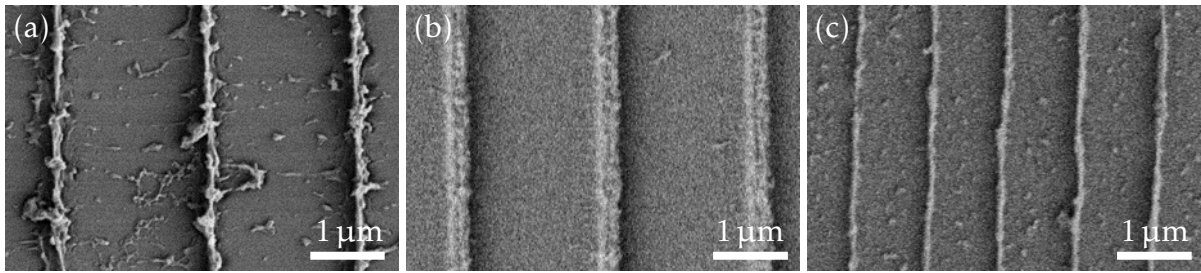


Figure 4.7: DLW with different initiators: SEM images of lines written in resist with MACA500 and (a) DETC, (b) I369 or (c) ITX.

ITX (cf. Fig. 4.7 (c))(linewidth around 370 nm and 210 nm, respectively). The structures written in a resist with ITX and MACA500 exhibit small feature sizes and solid lines without noteworthy polymerization towards the neighboring structures.

Besides the quality, the polymerization threshold is taken into account again. For resists with around 0.6 wt% initiator the resist with ITX polymerizes with the smallest power: for a writing speed of $10 \frac{\mu\text{m}}{\text{s}}$, the power at the threshold is 4.6 mW (cf. Sec. 4.3.1), 6.0 mW (cf. Sec. 4.3.1), and 38.4 mW [44] for resists with ITX, I369, and DETC, respectively.

This indicates that despite the high 2PA cross sections of DETC, ITX has the highest quantum efficiency for a radical polymerization with methacrylated cellulose acetates triggered by 2PA. Therefore, ITX is the preferred initiator for DLW with methacrylated cellulose acetate.

4.2.3 Enabling the handling

A suitable solvent is required to dissolve the cellulose derivative and the initiator, which react with each other in the radical polymerization. The solvent should not interfere during the reaction process nor should it show any absorption in the used wavelength range, to avoid heating up the resist. Furthermore, as a cellulose-based resist is predestinated for the fabrication of biocompatible or at least biodegradable structures, the solvent should not hinder this.

Due to their relatively low toxicity, acetone and dimethyl sulfoxide (DMSO) are considered, which are bio compatible according to [141, 142] and transparent in the visible spectral range. They are also not accessible for radical polymerization.

MACA500 is soluble in acetone and DMSO due to the high degree of substitution of the acetate groups. In contrast, MACA15 and MATC15 with a smaller degree of substitution of the acetate groups or the tosyl groups are not soluble in acetone, while they are soluble in DMSO.

The highly exhalable acetone has a vapor pressure of $2.4 \cdot 10^4$ Pa at normal circumstances ($T = 20^\circ\text{C}$) [143]. Its evaporation changes continuously the composition of the resist and, hence, influences the diffusivity of the molecules. After complete evaporation, the duration needed to develop the written structures increases in time as the components

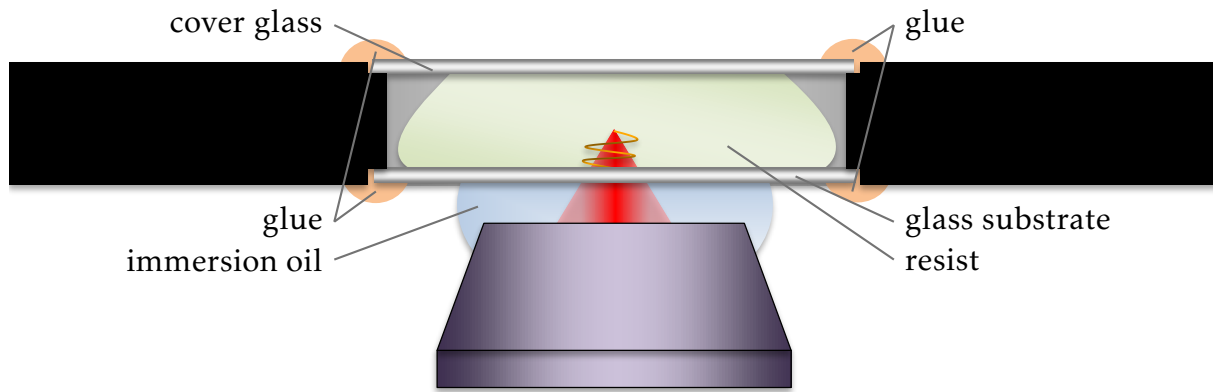


Figure 4.8: Modified setup for the DLW with cellulose-based resists. The cover glass reduces evaporation of the solvent and the absorption of water from humid air.

have to be solved completely again. The complete evaporation of acetone often leads to remaining particles on the substrate that contaminate the written structures.

To avoid the evaporation of the acetone, a processing chamber as in [144] can be used. As the vapor pressure is relatively high, the chamber has to stand either high pressure or the atmosphere has to be saturated with acetone to avoid evaporation. Both opportunities need a complex setup. A simple setup, using a cover glass on top of the glass substrate with the resist, reduces the evaporation but does not disable it completely. Such a simple setup is sketched in Figure 4.8. With the reduced evaporation, the stability of the processing parameters is improved to allow at least fabrication times of a few hours (1 h to 3 h).

DMSO has a vapor pressure of 55 Pa at normal circumstances ($T = 20^\circ\text{C}$) [145]. With the lower fugacity compared to acetone, the mass fractions of the DMSO resists remain nearly constant during the processing. However, DMSO is hygroscopic, which means it absorbs water from the air moisture. This small amount of water triggers a precipitation of the solid components. This again leads to a change in the processing parameters and unsolvable particle contamination on the structure in the end of the processing.

As for the evaporation of the acetone, this is reduced or avoided with a processing chamber [144] or the simple setup (cf. Fig. 4.8), but it is less critical, especially when there is a low humidity. If humidity is expected to be high, a protective gas can replace humid air, thus, avoiding a contact between resist and air. To improve the processing conditions in the simplified setup with a cover glass, the interspace between the glasses is flushed with nitrogen, as a protective gas, before attaching the cover glass. This minimizes the available air moisture and helps to avoid the precipitation of the initiator and the cellulose derivatives. Furthermore, the flushing with nitrogen possibly reduces the quenching and scavenging with oxygen, this may further reduce the power threshold needed for the polymerization.

Due to the lower fugacity and, thus, the more stable processing parameters, DMSO is recommended as a solvent for cellulose-based photoresists.

4. Direct laser writing in a bioinspired material

Of all combinations of these components, the combination of MACA500, ITX and DMSO performs best. For the discussion of the properties in the following section (Sec. 4.3) other combinations are considered, too. This is a result of the workflow and it highlights the advantages of the above mentioned combination of MACA500, ITX, and DMSO.

4.3 Properties of cellulose-based resists

In photolithography, different resists are optimized for different tasks that often contradict each other. For example, a resist that is optimized to create a smooth surface can make use of a high proximity effect (cf. Sec. 3.2.3). A high proximity effect, however, disables high resolution as the close proximity of the features induces a cross-polymerization between the features. The different specializations of the resists can be achieved with the same monomer by adjusting the other constituents. The same is true for MACA500. The properties of the cellulose-based resists with MACA500 differ depending on the adjustment of the other components and their proportions.

Nevertheless, the determination of some properties for resists containing MACA500 gives an estimation of the capabilities of these resists. Therefore, investigated properties are presented even though they are identified for resist with different mixtures. This allows an estimation of dependencies on the properties from the compositions of the resists.

To, first of all, enable DLW at different, affordable setups, the essential laser power that is necessary to achieve a cross-linking is considered in Section 4.3.1. Another important aspect to allow the reuse of the resist and the reproducibility of the written structures is the chemical stability of the resists (cf. Sec. 4.3.2). After these two define the general qualification, the field of application of the cellulose-based resists is determined by the achievable resolution (cf. Sec. 4.3.3) and other properties (cf. Sec. 4.3.4). In the end, a classification of these properties of the resists containing MACA500 is given in Section 4.3.5.

4.3.1 Polymerization threshold

An appropriate quantity to compare the performance of the different resists is the laser power, which correlates with the dose, needed for the polymerization. If these are very high, the resist can only be processed at DLW setups with high power lasers. This diminishes the usability of the resists extensively.

The necessary laser power P and the laser dose D depend on each other according to

$$D \propto (P - P_{th})^2 / v_w, \quad (4.1)$$

with the writing speed v_w and the Schwarzschild threshold P_{th} [75,146] for a cross-linking process that is initialized by a 2PA exclusively.

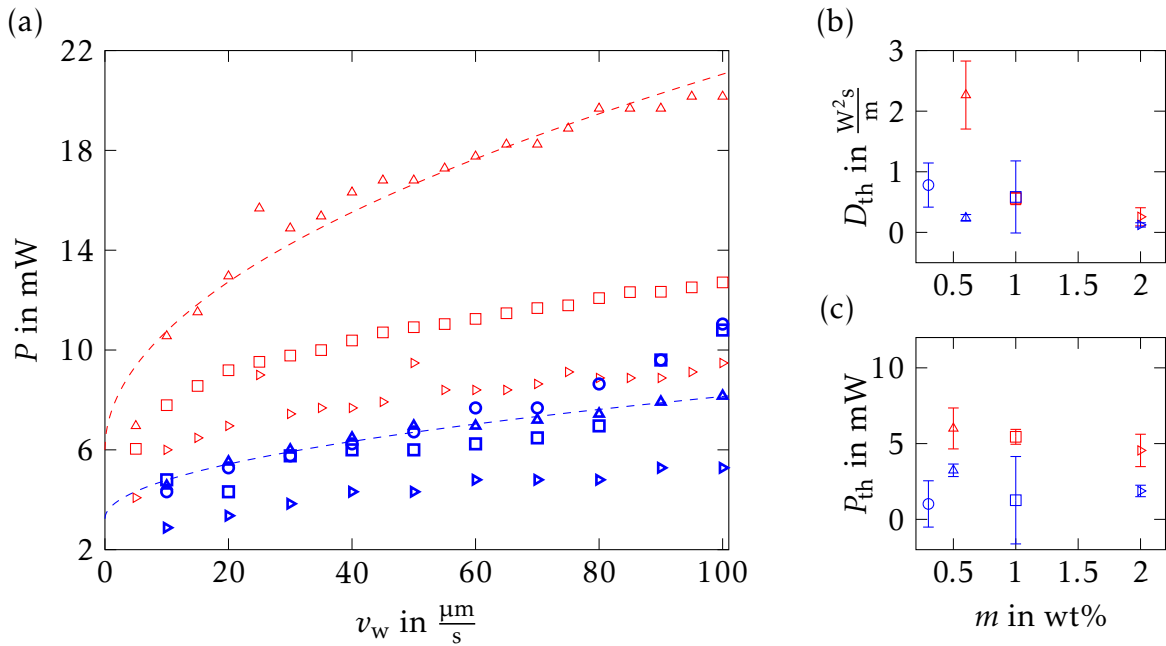


Figure 4.9: (a) The laser power at the polymerization threshold at different writing speeds: The resists contain I369 (red) or ITX (blue) at different concentrations ($\circ \hat{=} 0.3$ wt%, $\triangle \hat{=} 0.6$ wt%, $\square \hat{=} 1.1$ wt%, and $\triangleright \hat{=} 2.2$ wt%; errorbars are left out for clarity). Fitting of curves (dashed for $\triangle \hat{=} 0.6$ wt% as examples) yield (b) the threshold doses D_{th} and (c) the Schwarzschild thresholds P_{th} for the different initiators and their concentrations.

As the MACA500 cannot be excited itself, the threshold is mainly influenced by the initiator, by both its amount and its interaction with the MACA500. The laser power P at the polymerization threshold for different resists using I369 (red) and ITX (blue) is determined in dependence of the writing speed (cf. Fig. 4.9 (a)). The resists contain the same amount of DMSO compared to the mass of MACA500, while the amount of initiator is varied ($\circ \hat{=} 0.3$ wt%, $\triangle \hat{=} 0.6$ wt%, $\square \hat{=} 1.1$ wt%, and $\triangleright \hat{=} 2.2$ wt%). A trend expressed by:

$$P = \sqrt{D_{\text{th}} \cdot v_w} + P_{\text{th}} \quad (4.2)$$

is fitted to the data. For the resist with 0.6 wt% initiator, fitted curves are shown in Fig. 4.9 (a). All fitted parameters are summarized in Figure 4.9 (b) and (c).

The above mentioned dependence of the dose from the power and the writing speed (cf. Eq. 4.1) is a special case for pure 2PA. More general the dose D may depend on other orders of the power P . Especially for ITX, the dose depends on higher orders of the power [74, 147]. However, the courses with dependence on different orders of the power lead to negligible deviations in the observed writing speed range. Hence, to compare the different initiators, Equation 4.2 is applied to all results.

For both kinds of initiator, a decrease of the necessary laser power with increasing concentration of initiator is observed. The power decrease is induced by the decreasing threshold dose D_{th} (cf. Fig. 4.9 (b)). Especially for high writing speeds, the threshold dose has a larger impact on the laser power at the polymerization threshold than the

4. Direct laser writing in a bioinspired material

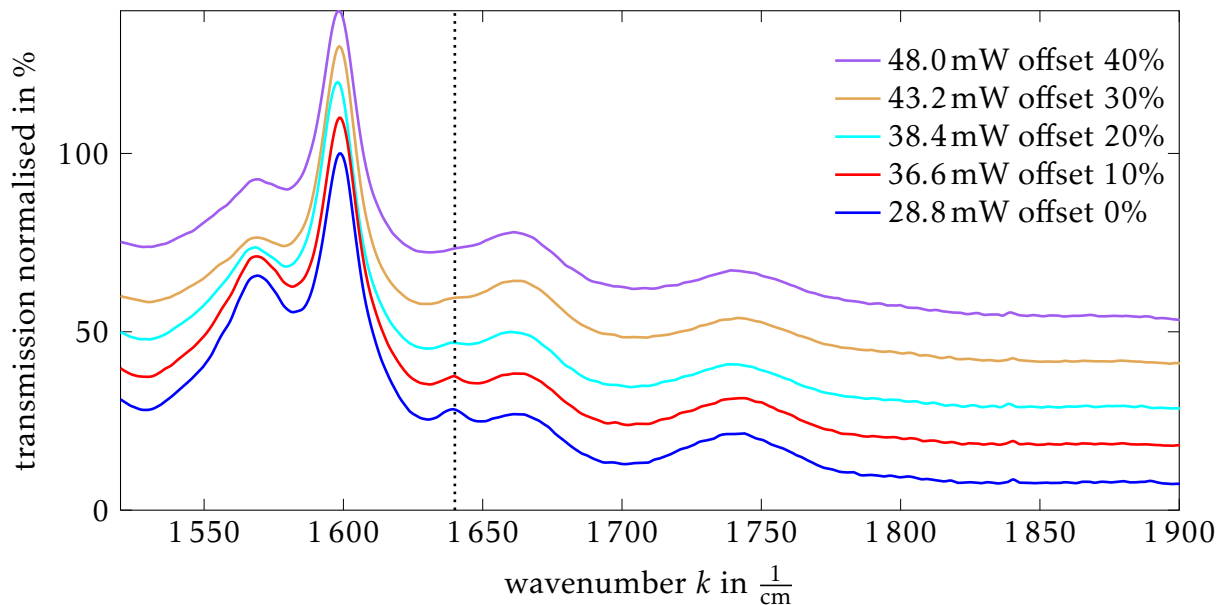


Figure 4.10: Raman-spectra of polymerized cellulose-based resist with an offset containing MACA500 (14.2 wt%), I369 (0.7 wt%), and DMSO (85.1 wt%) for different laser powers and a writing speed of $250 \frac{\mu\text{m}}{\text{s}}$. The characteristic peak of the carbon double bond of the methacrylic group is marked by the dashed line. After [44].

Schwarzschild threshold P_{th} (cf. Eq. 4.2). The Schwarzschild threshold is nearly constant for the different concentrations of initiator (cf. Fig. 4.9 (c)) leading to similar laser powers at the polymerization threshold for processes with very small writing speeds.

Due to the low writing speed, oxygen continues to diffuse into the excited volume and keeps the quenching rate constantly high. For shorter exposure times or higher writing speeds the diffusion of oxygen into the excited volume is too slow to hinder the reaction process. Although the amount of oxygen is reduced due to the setup presented in Section 4.2.3, there is still enough oxygen to quench the initiator molecules.

In general, resists with ITX require smaller laser powers to achieve a polymerization than resists with I369 as mentioned in Section 4.2.2. However, the above mentioned decrease in the laser power with increasing initiator concentration is more prominent for I369 than for ITX, because the decrease in the threshold dose is more prominent. For high concentrations of initiator, the threshold doses are similar while they differ for small concentrations. The resulting difference in the laser power at the polymerization threshold arises from the Schwarzschild threshold that differs by a factor of 3. Hence, the difference between the laser power at the threshold decreases with the writing speed (cf. Eq. 4.2): For an initiator concentration of 2.2 wt% at a writing speed of $10 \frac{\mu\text{m}}{\text{s}}$ the laser power for I369 is 208% of the laser power for ITX, while it is only 180% at a writing speed of $100 \frac{\mu\text{m}}{\text{s}}$. The above mentioned rate of quenching by oxygen is, therefore, higher for I369 than for ITX.

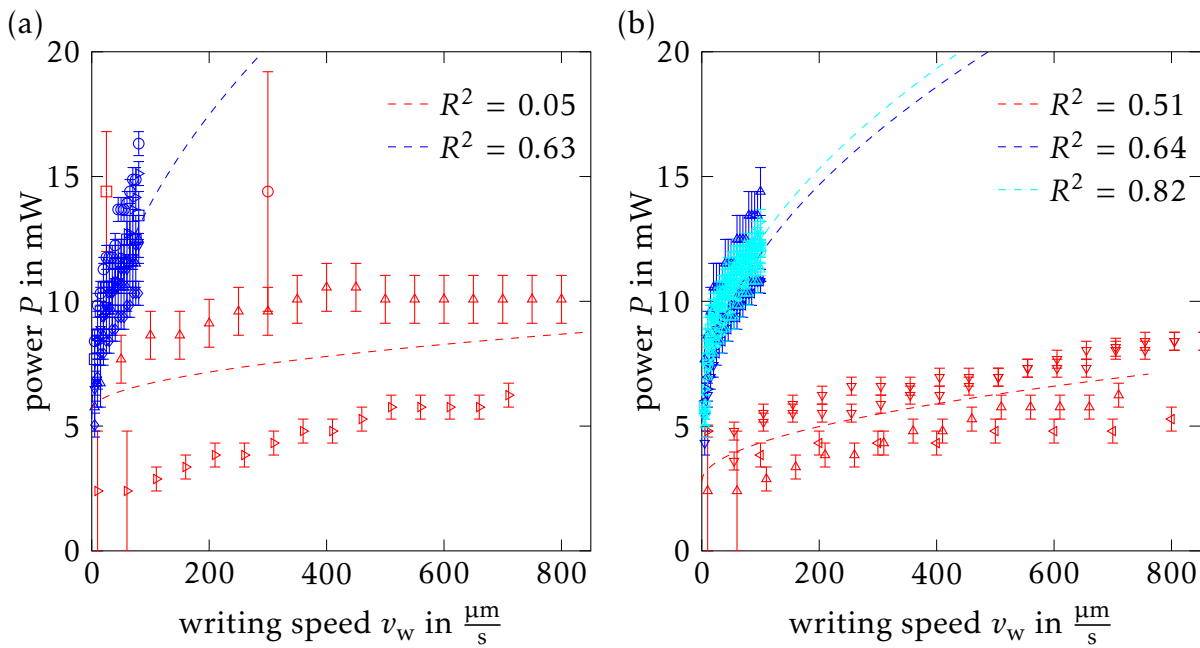


Figure 4.11: Threshold of different resists with different solvents: The resists contain acetone (red) or DMSO (blue, cyan) and are (a) at the same age but different preparations or (b) of different age (0d to 51 d) but same preparation. Related measurements are summarized in a single compensating curve, which should have a coefficient of determination of $R^2 = 1$ for an independence of time and preparation.

The discussed laser powers at the polymerization threshold lead to a cross-linking density that enables solid structures. However, at the threshold not all methacrylic groups are cross-linked. The degree of conversion is qualitatively regarded with Raman spectroscopy in relation to the laser power used for the writing process. These Raman spectra are shown in Figure 4.10. They show the characteristic peak of the methacrylic group at 1634 cm^{-1} , which was already shown and discussed in Section 4.2 (cf. Fig. 4.4). This peak decreases with increasing laser power. Hence, with increasing laser power the number of carbon double bonds is reduced and the cross-linking density increases. A qualitative analysis is disabled by the neighboring peaks of other molecular groups. [44]

The results show, that for a suitable initiator like ITX, low concentrations of initiator (around 1 wt%) suffice to polymerize the MACA500 (around 10 wt%) at affordable laser powers ($\ll 50\text{ mW}$) of DLW systems with no need of high power lasers.

4.3.2 Chemical stability

Reproducibility is at least as important as the threshold. The properties of the resist should not change with new preparations of the same mixture and as well as with time, allowing a long shelf-life and an independence on the preparation.

As the largest changes in the properties of the resist are expected to be caused by the solvents, because of their evaporation and interplay with humidity, resists with the same amount of MACA500, I369 and either acetone (red in Fig. 4.11) or DMSO (blue and cyan

4. Direct laser writing in a bioinspired material

Table 4.5: Fitted parameters to evaluate the reproducibility of different resists or recipes

solvent	Fit	D_{th}	P_{th}	R^2
DMSO	Fig. 4.11 (a) blue	0.74 ± 0.23	5.64 ± 0.88	0.63
	Fig. 4.11 (b) blue	0.45 ± 0.15	5.18 ± 0.82	0.64
	Fig. 4.11 (b) cyan	0.47 ± 0.07	5.62 ± 0.35	0.82
Aceton	Fig. 4.11 (a) red	0.01 ± 0.03	5.64 ± 3.31	0.05
	Fig. 4.11 (b) red	0.02 ± 0.01	2.77 ± 0.85	0.51

in Fig. 4.11) as a solvent are observed. The polymerization threshold is illustrated in Figure 4.11 for (a) different fresh resists (younger than two days) with the same recipe and (b) of three different resist at different points in time.

For negligible changes of the properties of the resist, the power threshold should be constant. Hence, a compensating curve for all measurements of one recipe or resist should have a coefficients of determination $R^2 = 1$. All preparations with the same recipes are summarized in a single compensating curve (Fig. 4.11 (a) blue dashed curve for DMSO and red for acetone) as well as all measurements that where performed with the same resist but at different times (Fig. 4.11 (b) blue, cyan, and red dashed curves). The compensating curves correspond to Equation 4.2 and reveal the values for the threshold dose D_{th} , the Schwarzschild threshold P_{th} , and the coefficient of determination R^2 that are summarized in Table 4.5.

For resists with acetone (red in Fig. 4.11) the identified laser power for the polymerization is low but changes a lot, especially for different preparations ($R^2 = 0.05$; cf. Tab. 4.5). As the resist preparation is not conducted under the exact same circumstances (change in humidity, room temperature or processing time), the amount of solvent changes due to a differing amount of evaporated solvent. This leads to the large discrepancies in the power threshold for different preparations.

Considering the time (cf. Fig. 4.11 (b)), acetone evaporates out of the resist, which is kept in a lockable jar. As these jars are not gas tight and they are opened for the withdrawal of resist, the evaporation can continue and no partial pressure equivalence is reached. This leads to changes in the power threshold over time for a single resist.

Resist with DMSO show a higher threshold but a smaller variation both in preparation and time with correlations of up to $R^2 = 0.82$ (blue and cyan curves). Hence, the power threshold of the resist containing DMSO is reproducible even if a new preparation is used. The reproducibility of the threshold indicates a stability of other properties, too. Hence, only solvents with a low fugacity, like DMSO, enable reproducible structuring.

4.3.3 Resolution in 2D and 3D

After the above mentioned properties focus on the resists themselves, as a first characteristic of the fabricated structures, the achieved resolution and feature size are discussed.

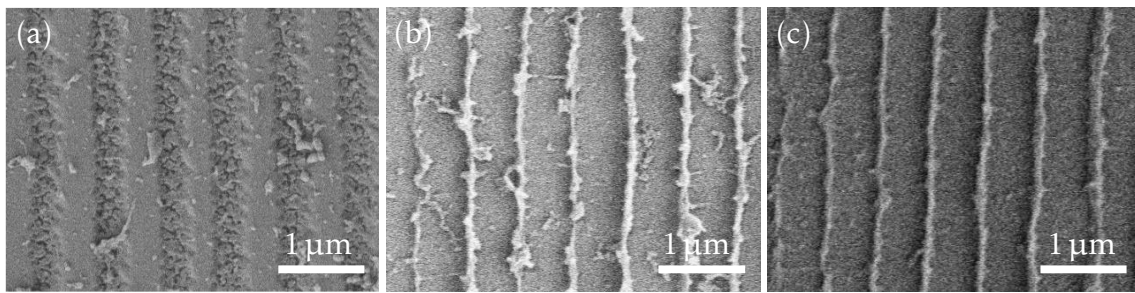


Figure 4.12: 2D resolution of different cellulose-based resists: SEM images of lines with (a) a periodicity of 750 nm and a feature size of 430 nm written with a resist containing MACA500, I369, and acetone; (b) a periodicity of 600 nm and a feature size of 200 nm written with a resist containing MACA500, I369, and DMSO; (c) a periodicity of 600 nm and a feature size of 130 nm written with a resist containing MACA500, ITX, and DMSO.

The features size and resolution define the length scale of possible structures and, hence, the field of application.

The resolution in 2D is defined as the smallest distance between two lines that are clearly separated. In 3D the resolution can be estimated by the periodicity of a written 3D grid or periodic arrangement that shows a separation of vertically neighboring features. Here, the programmed distances of the structure are used as a guide value, because the achieved distance between the lines may deviate from the programmed distances due to shrinkage. Hence, the real resolution is in most cases higher than the programmed distances.

With MACA500 (11.0 wt%), I369 (0.6 wt%) as an initiator, and acetone (88.4 wt%) as a solvent, a resolution of 750 nm and a feature size of around 430 nm is achieved in 2D [115]. The 2D resolution is improved to 600 nm and a feature size of around 200 nm if DMSO (87.0 wt%) is used instead of acetone as a solvent and the initiator concentration is increased (2.2 wt%) [44]. By using ITX (1.0 wt%) and DMSO (88.4 wt%) as further components with the MACA500 (10.6 wt%), the resolution is not further improved (still 600 nm) but the achieved feature size is decreased to around 130 nm (cf. Fig. 4.12 (c)) while the feature quality is improved.

The resolution of the different resists depends on their composition, e.g., the kind and amount of initiator influences the proximity effect due to its diffusivity (cf. Sec. 3.2.3). However, the proximity effect and, thus, the resolution strongly depends on the writing parameters, too. The parameters also co-determine the voxel size and, therefore, the feature size, as the voxel size increases with the used laser power.

The cross-polymerization between neighboring features due to the proximity effect, is reduced by avoiding temporal proximity of written features. The resolution of a resist is improved if the time between the excitation of neighboring volumes is increased [101], e.g., by programming a higher dwell time between the features or using smaller writing speeds. Thus, more radicals are scavenged by oxygen, which could otherwise allow polymerization towards the adjacent features. For a resists with MACA500, the achieved

4. Direct laser writing in a bioinspired material

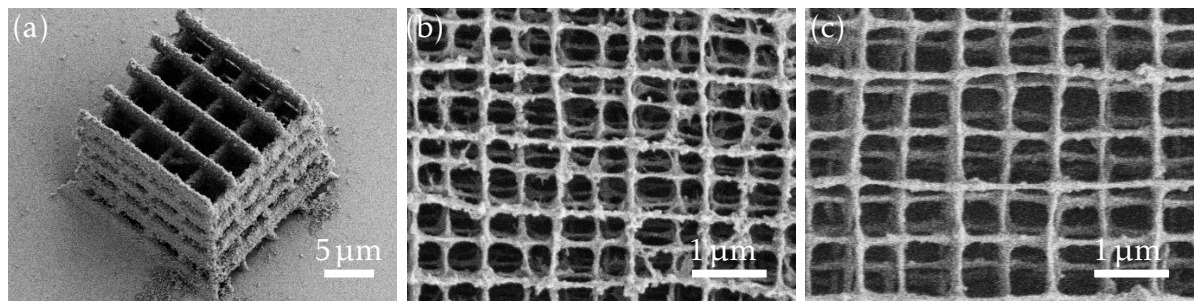


Figure 4.13: 3D resolution of different cellulose-based resists: SEM images of (a) a 3D periodic grid with a periodicity of $4.5\ \mu\text{m}$ in axial and lateral direction written with a resist containing MACA500, I369, and acetone; (b) a woodpile structure with a periodicity of $1.0\ \mu\text{m}$ in lateral and $1.4\ \mu\text{m}$ in axial direction written with a resist containing MACA500, I369, and DMSO; (c) a woodpile structure with a periodicity of $1.5\ \mu\text{m}$ in lateral and $2.1\ \mu\text{m}$ in axial direction written with a resist containing MACA500, ITX, and DMSO.

resolution is improved from above $1\ 000\ \text{nm}$ to $600\ \text{nm}$ by increasing the temporal delay between the excitation of neighboring features from around $70\ \text{ms}$ to around $430\ \text{ms}$ [44].

A high 2D resolution may be achieved by other lithography methods like UV-lithography using 1PA. The realization of nearly arbitrary 3D structures is the remarkable capability of DLW. Hence, a 3D structuring is the distinguishing application of the resist presented here compared to [148].

3D structuring is possible for different resist containing MACA500. The achieved resolution depends on the exact mixture and the writing parameters, as the 2D resolution. A resist using acetone (87.9 wt%) and I369 (1.1 wt%) already allows a 3D structuring with a resolution of $4.5\ \mu\text{m}$ in lateral and axial direction (cf. Fig. 4.13 (a)) [115].

The 3D resolution is improved using resists with DMSO (87.0 wt% and 88.4 wt%) and either I369 (2.2 wt% cf. Fig. 4.13 (b)) or ITX (1.1 wt% cf. Fig. 4.13 (c)). With these resist, woodpile PC structures with a lateral periodicity of $1.0\ \mu\text{m}$ and $1.5\ \mu\text{m}$ and a programmed axial periodicity of $1.4\ \mu\text{m}$ and $2.1\ \mu\text{m}$, respectively, are fabricated. The resulting feature sizes are in the range of the 2D line width, e.g., around $180\ \text{nm}$ for the resist containing ITX (cf. Fig. 4.13 (c)).

As for 2D structures, these 3D structures require an optimization of the writing parameters. In Figure 4.13 (b) and (c), the polymerization threads, which are caused by the proximity effect, are reduced as the writing speed is decreased from $300\ \frac{\mu\text{m}}{\text{s}}$ in (b) to $100\ \frac{\mu\text{m}}{\text{s}}$ in (c). The structure in Figure 4.13 (a) is written with a writing speed of only $20\ \frac{\mu\text{m}}{\text{s}}$, but the capabilities of the resist containing acetone do not include high resolution 3D structures.

The resolution may also be determined by the length of the molecules. With a theoretical length of $250\ \text{nm}$ (cf. Tab. 4.1) for the MACA500 molecules, a distance of less than $500\ \text{nm}$ can theoretically be spanned by two molecules. Hence, an orientation of the molecules out of the writing direction may decrease the resolution. With shorter molecules that allow DLW with suitable parameters the resolution may be further improved.

The achieved resolution of around 600 nm in 2D and around 1 μm in the lateral direction and around 1.4 μm in the axial direction in 3D is encouraging. These resolutions already enable different applications, like the fabrication of certain up-scaled biomimetic structures (cf. Sec. 4.4).

4.3.4 Further properties

One further investigated property of the fabricated structures beside the resolution is the achieved surface roughness of direct laser written structures. The surface roughness is measured with an atomic force microscope over a scanning field of $(5 \times 5) \mu\text{m}$ that is part of a flat structure written with resists containing MACA500, I369, and acetone. Here, the proximity effect improves the surface quality, because cross-polymerization can fill dips between written features. As the proximity effect increases with the initiator concentration, a decrease of the rms roughness [149] of structures from 60 nm to 10 nm, due to an increase of the initiator concentration from 0.6 wt% to 1.1 wt% in resists with MACA500 (11.0 wt% and 11.0 wt%) and acetone (88.4 wt% and 87.9 wt%) [115], is observed.

As in the case of the resolution, the surface roughness depends on the writing parameters, too. In the case of surface quality, the line distance that is used to hatch the structure is a limiting parameter. For large line distances the surface adopts the periodicity of the lines, but for small distances the writing time increases and the overlapping of excited volumes may lead to an overexposure. The achieved surface roughness is a tradeoff between the processing time and the programmed line distance. For the measured samples line distances of 200 nm to 400 nm are programmed leading to a comparable roughness.

The stability of written structures strongly depends on the processing parameters, too, and of course of the composition of the resist. With a laser power of around 12 mW at small writing speeds $20 \frac{\mu\text{m}}{\text{s}}$, large stable structures like the 3D grid in Figure 4.13 (a) are fabricated. These high laser powers, however, disable fine features. With laser powers of around 10 mW and a writing speed of $100 \frac{\mu\text{m}}{\text{s}}$, the features are much smaller, but a written network-like structure may further fractures at weak points in the programmed structure like described in [44].

A last property of the written structure, to estimate applications in the field of optics and photonics, is the refractive index. The cellulose-based resists may show a dependence of the refractive index on the processing, like the used wavelength (1PA with UV or 2PA with visible light) or the laser dose, as it is observed for common resists [150]. Nevertheless, the refractive index of a UV cured cellulose-based resist gives a reference point for future investigations. The refractive index of a UV cured cellulose-based resist is determined in [44] with a Pulfrich refractometer [44, 150] to be $n_{\text{resist}} = 1.502 \pm 0.001$. This refractive index corresponds to the refractive index of cellulose, which is between $n = 1.42$ and $n = 1.53$ [151].

The given properties of the structures written in cellulose-based resist only foreshadow the potential of these resists. With a targeted adaptation of the composition and the

4. Direct laser writing in a bioinspired material

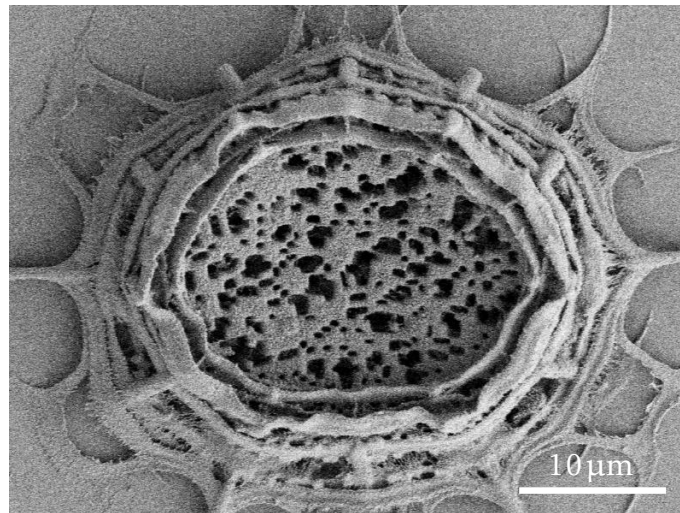


Figure 4.14: SEM image of a fabricated model structure of the *Cyphochillus insulanus* in a cellulose-based resist containing MACA500 (10.3 wt%), ITX (0.5 wt%), and DMSO (89.2 wt%).

processing parameters different application, like scaffolds for cell growth as in [152] or fabrication of biomimetic materials (cf. Sec. 4.4) are possible.

4.3.5 Summary

The cellulose-based resists are suitable for the use at common DLW setups without the need of high power lasers due to their low threshold for the polymerization. Furthermore, they allow for reproducible fabrication of structures. Here, especially the resists with MACA500 (around 10.5 wt%), ITX (around 1.1 wt%), and DMSO (around 88.4 wt%) have performed well. They allow structures with lateral feature sizes of less than 200 nm and resolutions smaller than 1.5 μm in 3D.

These properties of cellulose-based resists give reference points for future resist development, as the exact properties of the fabricated structures depend not only on the composition of the resist but also on the processing parameters. Therefore, the full potential of cellulose-based resists is not yet reached. With further optimization of composition and processing parameters they may find their way into many applications.

4.4 Outlook: Bioinspired structures in a bioinspired photoresist

In Section 5.4.2 the fabricated model, which mimicks the disordered, network like structure within the scales of *Cyphochillus insulanus*, is presented. It is achieved after up-scaling the simulated model to length scales that are accessible to fabrication with DLW. The layers in the fabricated structure are fixed by pillars between neighboring layers and an external framework. During the writing process the laser dose is adjusted to achieve

4.4. Outlook: Bioinspired structures in a bioinspired photoresist

the necessary stability and cross-linking density in the framework and to modulate the thickness within the layers. With this structure (cf. Fig. 5.17) the optical properties of the scales of *Cyphochillus insulanus* are mimicked qualitatively.

The adaptation of the thickness and the stability of the structures with the laser dose is also possible in the cellulose-based resist. A first attempt to fabricate the model system of the *Cyphochillus insulanus* with a round lightweight construction framework with a resist containing MACA500 (10.3 wt%), ITX (0.5 wt%), and DMSO (89.2 wt%) shows promising results (cf. Fig. 5.17). The pixel-like composition of the layers is visible and the framework supports the layers and reduces their bending. However, the structure strongly shrinks and the stability of the support structure is not yet sufficient to completely prevent contact between adjacent layers.

With further optimization of the composition and the writing parameters the cellulose-based resists allow the fabrication of an up-scaled model of *Cyphochillus insulanus* with DLW. This opens up routes to the application of bioinspired structures fabricated out of bioinspired materials.

4. Direct laser writing in a bioinspired material

Chapter 5

Investigated biological systems

The knowledge and understanding of photonic structures that exist in nature are very young compared to the evolutionary development of these structures. At the beginning of the 20th century, scientists discussed the coloration of different animals due to the structuring of normally transparent materials. Among these scientists was Lord Rayleigh [153]. Proving their theories was possible in the middle of the 20th century by high-resolution imaging technologies, like electron microscopy and X-ray tomography. Natural photonic structures that can generate brilliant coloration are nowadays well known to scientists all around the world, some unriddled, others still objects of investigation.

In the course of this work, four of these fascinating structures are examined. These four are found in the animal kingdom or to be more precise on insects. Hence, they mainly consist of chitin, the basic building material of insects cuticle. Chitin is a low refractive index material ($n_c = 1.54$ to $n_c = 1.57$ for the visible spectral range [12, 154]), which, besides cellulose, is the most abundant biopolymer in the world [155, 156].

In this chapter, the optical principles of the four examined structures responsible for their optical properties are explained and scalable, bioinspired models, which mimic the optical properties, are presented. The corresponding structures are fabricated in conventional photoresists (IP-L or IP-Dip by Nanoscribe GmbH) using DLW.

The first examined insect, the Saharan silver ant (cf. Sec. 5.1), which reveals a very simple underlying structure, is investigated in close collaboration with J. Schulz [42] and in cooperation with B. Schwind of Paderborn University. The silver ants exhibit a nearly wavelength-independent reflection for the visible spectral range, which makes them look silver.

The well understood structure of the butterflies of the genus *Morpho* (cf. Sec. 5.2) is on the other hand wavelength selective, while the underlying structure is still relatively simple. A corresponding model for these in principle ordered structures, which theoretically enables fabrication, is developed in close collaboration with D. T. Meiers [43, 157]. With DLW, the structures cannot be fabricated because the dimensions required for blue coloration are too small to be produced precisely.

5. Investigated biological systems

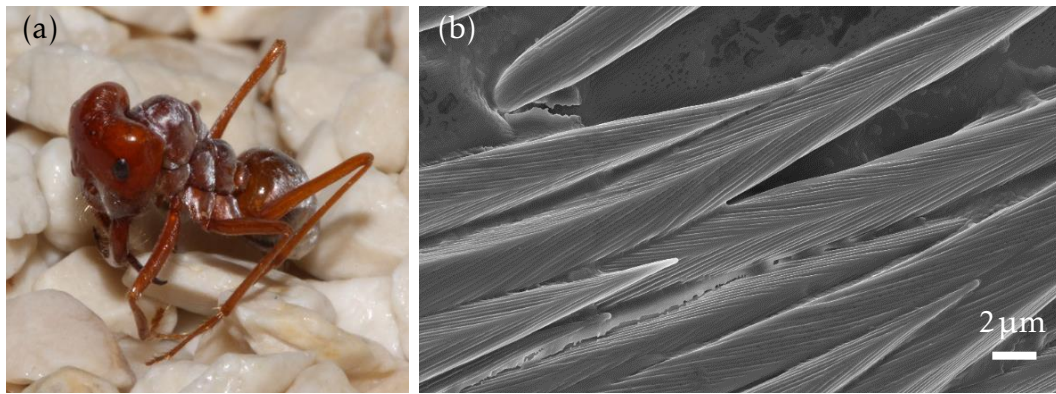


Figure 5.1: Saharan silver ant or *Cataglyphis bombycina*: (a) picture of an ant with its hairs providing a silver appearance; (b) a SEM image of a bundle of hairs. Both images by courtesy of X. Wu.

The still ordered but wavelength- and polarization-dependent structure in the scales of the weevil *Entimus imperialis* is investigated in cooperation with X. Wu [13] and is presented in Section 5.3.

As a last structure, the disordered, wavelength-independent structure found in the scales of the white beetle *Cyphochillus insulanus* is presented in Section 5.4. The adaptable model system of this structure was developed and fabricated in close collaboration with D. T. Meiers [43, 157].

The theses of J. Schulz and D. T. Meiers were supervised and instructed by myself during this project. Already published results are appropriately marked.

5.1 *Cataglyphis bombycina* – the silver ant

The Saharan silver ant lives in the deserts of Africa and the Arabian Peninsula. The workers of a colony get out of their formicary during the day when lizards – their natural enemies – have to hide to escape the enormous heat. To protect themselves from overheating, nature has developed different mechanisms. First, they produce a certain protein which enables normal cell functionality at higher temperatures before they expose themselves to the heat. Second, they have longer legs compared to other ants. These long legs keep them as far away as possible from the hot ground and allow to move faster, which optimizes convection cooling. And finally, their bodies are covered with silver hairs that reflect a large amount of the sunlight, so the absorption that heats the ants up is reduced, while at the same time the hairs allow the body heat radiation to be emitted. [8, 9]

The hairs of the Saharan silver ant or *Cataglyphis bombycina* (see Fig. 5.1(a)) are the first presented example in this work for photonic structures in nature. Here, geometric optics achieve total internal reflection in the hairs that cover the ant's body. After the structure is analyzed in the first section a fabricated model is presented in Section 5.1.2.

5.1.1 The underlying concept of the hairs of *Cataglyphis bombycina*

To understand the silver appearance of the ants, the optics of a single hair as well as a potential interplay have to be considered. Therefore, this section is divided into two parts discussing first the optics of a single hair and subsequently the interplay of the hairs.

Optics of a single hair

A single hair has an isosceles triangular cross section with a flat bottom side and corrugated upper sides [9]. Such a hair is around $3.5\mu\text{m}$ wide at the basal plane and between $1.7\mu\text{m}$ to $2.4\mu\text{m}$ high from the basal plane to the top. This corresponds to a basal angle of $\beta = 45^\circ$ to $\beta = 54^\circ$ and an angle at the top of $\alpha = 90^\circ$ to $\alpha = 72^\circ$.

The corrugation on the upper sides are 50nm to 66nm deep and separated from each other by 204nm to 396nm . They are tilted towards the basal plane of the hair by an angle of 18° .

These data were found by our collaboration partners in Paderborn and Düsseldorf H. Fabritius, X. Wu and B. Schwind as well as in the work of Q. Willot et al [9]. The work of Q. Willot et al, which is the first published work describing the optical properties of the ant by the use of prisms, was published during my joint work on the structures of silver ants with J. Schulz and our collaboration partners.

To understand the optics of a single hair, a simple model is used: an isosceles triangular prism without any surface structure on top. This represents a refracting prism which is explained by geometric optics and Snell's law.

Light that hits the prism with an angle of incidence ι (cf. Fig. 5.2) to the normal of the basal plane has an angle of incidence on the upper side B1 (cf. Fig. 5.2) of the prism of

$$\theta = \iota - \beta. \quad (5.1)$$

This light is refracted (cf. Fig. 5.2) and spreads inside the prism with an angle of

$$\phi = \arcsin\left[\frac{n_a}{n_c} \sin(\theta)\right] \quad (5.2)$$

towards the normal of the surface B1, with the refractive indices for air $n_a = 1$ and chitin $n_c = 1.56$ as in [12]. When light hits the bottom surface A under an angle ζ with

$$\zeta > \zeta_{\text{TIR}} = \arcsin\left(\frac{n_a}{n_c}\right) \quad (5.3)$$

larger than the angle of total internal reflection (short: TIR), with

$$\zeta = \phi + \beta, \quad (5.4)$$

it leaves the prism on the other upper side B2 (cf. Fig. 5.2 (a)).

5. Investigated biological systems

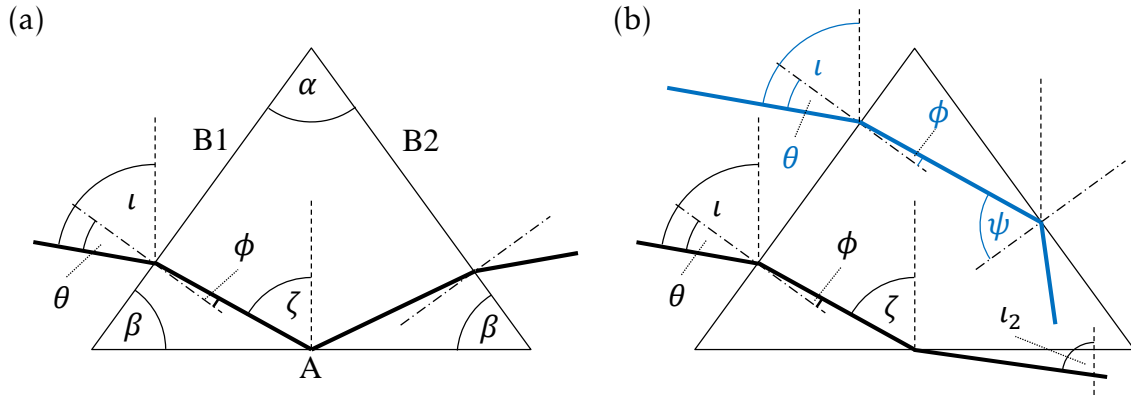


Figure 5.2: Simple model of the hair of a Saharan silver ant: (a) optical path with total internal reflection at the bottom side A; (b) optical paths with total internal reflection at top side B2 (blue) or refraction at the bottom side (black).

With a given angle β of the triangular shape, this also defines a critical angle of total internal reflection for the external incident angle of light:

$$\begin{aligned}
 \iota_{\text{TIR}} &= \beta + \theta_{\text{TIR}}, \\
 &= \beta + \arcsin \left[\frac{n_c}{n_a} \sin(\phi_{\text{TIR}}) \right], \\
 \iota_{\text{TIR}} &= \beta + \arcsin \left\{ \frac{n_c}{n_a} \sin \left[\arcsin \left(\frac{n_a}{n_c} \right) - \beta \right] \right\}.
 \end{aligned} \tag{5.5}$$

For all incident angles ι larger than ι_{TIR} , light that hits the bottom facet is completely reflected. The critical angle for total internal reflection at the bottom facet ι_{TIR} decreases with an increasing basal angle β of the prism (cf. Fig. 5.3 black line). Hence, a larger angular range experiences total reflection at the bottom facet. This indicates an advantage of large basal angles.

However, with large basal angles the amount of light hitting the bottom facet at all decreases (cf. Fig. 5.3 color mapping). Instead light impinges the opposite side facet B2, where it is either refracted or reflected. At the second upper side B2 total internal reflection occurs for all beams with an incident angle $\iota < \iota_C$ with:

$$\begin{aligned}
 \iota_C &= \beta + \theta_C, \\
 &= \beta + \arcsin \left[\frac{n_c}{n_a} \sin(\phi_C) \right], \\
 &= \beta + \arcsin \left[\frac{n_c}{n_a} \sin(\pi - 2\beta - \psi_C) \right], \\
 \iota_C &= \beta + \arcsin \left\{ \frac{n_c}{n_a} \sin \left[\pi - 2\beta - \arcsin \left(\frac{n_a}{n_c} \right) \right] \right\}.
 \end{aligned} \tag{5.6}$$

The dependency of ι_C from the basal angle β is indicated by the white line in Fig. 5.3. For basal angles smaller than 61° , all incident light that hits the second side facet B2 is totally reflected. Light, that is totally reflected at the side facet B2, leaves the prism through the

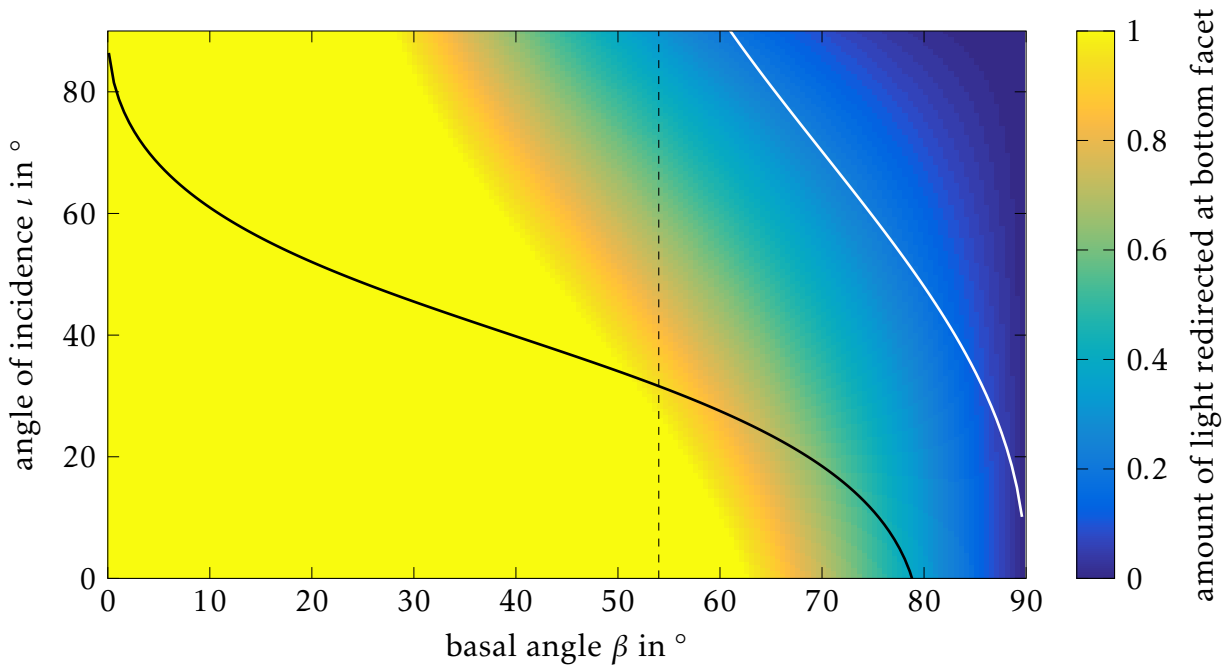


Figure 5.3: Quantitative analysis of a single hair with geometric optics: the critical angle of total internal reflection at the bottom facet A ι_{TIR} (black line) and maximum incident angle for total reflection at the side facet B2 ι_c (white line) of the prism depend on the basal angle β . The color coding describes the amount of light redirected, so refracted or reflected, at the bottom facet A. The dashed black line indicates the basal angle of the Saharan silver ant hairs predicted in [9].

bottom facet A (blue path in Fig. 5.2 (b)). It is directed towards the ant's body and can be absorbed, which heats up the ant.

If the basal angle is increased above 61° , light can be refracted at the second side facet B2, the resulting beam path is then still directed towards the ant's body. Additionally, the amount of light hitting the second side facet B2 is increased with large basal angles, which is indicated by the color coding in Figure 5.3. Therefore, the amount of light being redirected towards the ant's body and heating up the ant rapidly increases with increasing basal angles.

The optimum basal angle, therefore, is a trade off between a small external angle for total internal reflection at the bottom facet ι_{TIR} and a low amount of light reflected and refracted at the second side facet B2. For a basal angle in the range of $\beta = 45^\circ$ to $\beta = 54^\circ$, the external angle for total internal reflection at the bottom is kept between $\iota_{\text{TIR}} = 37.0^\circ$ to $\iota_{\text{TIR}} = 31.6^\circ$, while the amount of light reflected at the side facet B2 is kept below 50.6% to 69.6% for each incident angles, respectively.

The beam paths discussed above explain the optical impression of a single hair of the silver ant, too. They can also explain some results of numerical calculations presented in [9].

In [9] a single hair is illuminated in an experimental setup. The hair appears silver at the edges and transparent in the middle. The transparency, in the middle of the hair, is

5. Investigated biological systems

due to the blue beam path sketched in Figure 5.2 (b). Light that hits the prism at the top corresponding to the middle of the hair is more likely to be reflected at the second side facet B2 especially for large external incident angles. Hence, no reflection can be observed from the top of the prism (the middle of the hair). The hair appears transparent. Light that encounters the prism at the bottom, or as to say the hair at the edges, follows the black beam path in Figure 5.2 (a). It suffers TIR that is suppressed if the hair lies on a copper surface as in [9]. The TIR at the bottom facet leads to the shiny, silver appearance, characterizing the ants.

Furthermore, if an array of hairs is considered, the amount of light hitting the prism at the bottom is further reduced due to the shadow of neighboring hairs, again especially for large incident angles ι . These beams rather hit another hair at the top or middle of the prism, than the observed hair at the bottom. This reduced reflectance for large incident angles is confirmed by the measurement of a 2mm^2 surface of a hairy ant presented in [9]. Here, the radiance decreases for large angles of incidence which is not observed in the simulations of a single prism [9] as this effect is due to the shadowing by neighboring hairs. The interaction of the different hairs of the Sarahan silver ant is further described below.

For the mid-infrared range (MIR), the spectral intensity of the sun is negligible, while the black body radiation reaches its maximum if typical temperatures (-15° to 50° [158]) in the desert are considered [55]. For this wavelength range the prism-shaped hairs work as a gradient refractive index layer, which adapts the refractive index from the ants body slowly to the refractive index of air. Therefore, they enhance the emission of thermal radiation of the ant's body itself. [8]

The optical properties of a single hair in the visible and the MIR range are already well described with this simple model without any surface texture or any features inside the prism. Hence, the effect of these features is small compared to the effect of the prism itself.

Nevertheless, the effect of the corrugations on the upper sides of the hairs of the silver ant are worth mentioning. These corrugations work as a gradient refractive index layer, considering the effective refractive index in the visible spectral range. Therefore, they act as an anti-reflection coating for the visible spectral range according to [9]. The corrugations reduce the reflectance for the incoming light from around 5.4% to 0.5%. For outgoing light – after total internal reflection at the bottom side – the reflectance is reduced to only 2% to 4% [9]. To not reduce or hinder the total internal reflection at the bottom side, this side has no corrugations. In total the corrugations on the upper sides lead to an increasing amount of light leaving the hair through the upper sides.

The influence of interaction

As the ant's body is covered with a number of hairs, which are not arranged in perfect order, interactions between different hairs and tilting of different hairs towards the incident direction of the light influences the optical properties. A detailed investigation of

the different parameters in a periodic arrangement of hairs is found in the Bachelor thesis of J. Schulz [42]. The main results are summarized here.

As mentioned in the above section, the hairs may shadow each other, but they may also favorably redirect the light towards each other. If no total internal reflection occurs at the bottom facets of the prism ($\iota < \iota_{\text{TIR}}$) light is refracted (black path in Fig. 5.2 (b)). It leaves the prism with an angle ι_2 towards the normal of the basal plane:

$$\begin{aligned}\iota_2 &= \arcsin \left[\frac{n_c}{n_a} \sin(\phi + \beta) \right], \\ \iota_2 &= \arcsin \left\{ \frac{n_c}{n_a} \sin \left[\arcsin \left(\frac{n_a}{n_c} \sin(\iota - \beta) \right) + \beta \right] \right\}, \\ \iota_2 &> \iota.\end{aligned}\tag{5.7}$$

Hence, at a second layer of prisms below the first layer, the incident angle can become large enough to allow total internal reflection at the bottom side of a prism in this layer.

For each additional layer a new angle of incidence for total internal reflection at the j th layer $\iota_{j\text{TIR}}$ can be defined as explained in [42]. An additional layer j leads to a significant increase in the reflectance in the angular range between $\iota_{j\text{TIR}}$ and $\iota_{j-1\text{TIR}}$. For basal angles of $\beta = 45^\circ$ to $\beta = 52^\circ$ the maximum effect is achieved with three layers. The mean reflectance increases from 24% for one layer to 45% for three layers. Further layers enhance the reflectance, but the increase per layer decreases (cf. Fig. 5.4 (a)). This corresponds to the optical impression of the ants and the SEM images in different publications. Here only a few hairs (2 or 3) overlap each other [8,9]. The cutoff of the graphs in Figure 5.4 at around 75° is due to the capabilities of the simulation mentioned in [42].

Besides the number of layers, the distance between the different layers has also an influence on the reflectance. If two layers are considered, the largest increase in the reflectance for small angles $\iota < \iota_{\text{TIR}}$ of incidence is observed for direct contact of the two layers due to total reflection at the lower layer. For larger distances the effect of the second layer is still observed but less prominent (cf. Fig. 5.4 (b)).

For the angular range, which experiences total reflection in the first layer, the reflectance is reduced for a direct contact of the layers, while it increases for the intermediate and large distances (cf. Fig. 5.4 (b)). This behavior can be explained by frustrated total reflection, which was also shown for hairs on a copper surface in [9]. The effects for large and small angles of incidence balance. Hence, the mean reflectance over all incident angles is independent of the layer distance and is about $(49 \pm 15)\%$ [42].

5.1.2 Fabrication of prism-shaped hairs with DLW

The simple model of prism-shaped hairs allows fabrication of these structures. In the simulation, the hairs are mimicked by prisms that exhibit a perfect triangular shape with flat surfaces and sharp edges. For all sorts of fabrication methods, the edges exhibit a certain radius of curvature.

5. Investigated biological systems

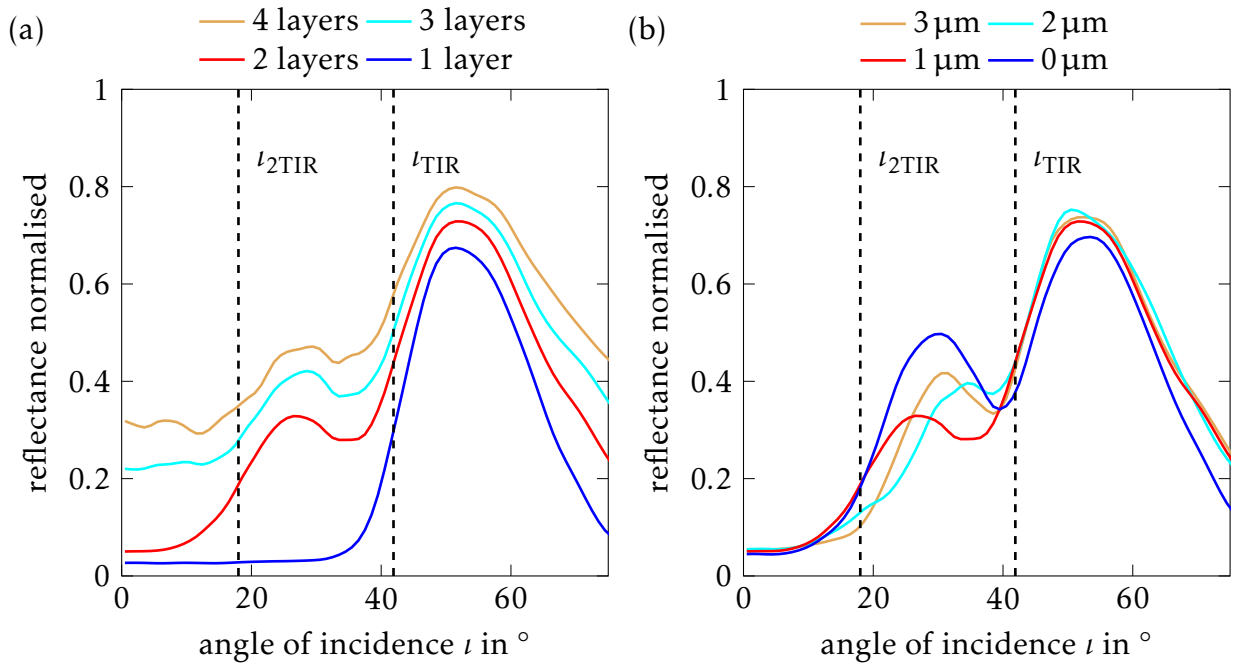


Figure 5.4: The mean reflectance of an arrangement of prism like hairs: for (a) a different number of layers of hairs or prisms and (b) different distances between the bottom of the upper layer and the top of the lower layer of prisms simulated with two layers. Both calculated with FDTD for glass prisms and for a basal angle of $\beta = 45^\circ$. After [42].

With DLW, the radius of curvature is determined by the voxel size in the direction perpendicular to the edge. The edges of the prisms can be orientation parallel or perpendicular the beam propagation of the laser and, hence, the axial direction of the voxel size. If the hairs are written in the axial direction of the DLW setup, parallel to the propagation direction of the laser beam, the lateral voxel size defines the radius of curvature at the edges. As the voxel size in the lateral direction is small compared to the axial direction, this allows relatively sharp edges with a high contour accuracy. The triangular cross section of the hairs in this configuration is seen at the SEM image of the structure in Figure 5.5 (a). However for measurements, we want the prisms aligned parallel to the substrate. Hence, they have to be turned by 90° such, that the bottom side of the prisms is directed towards the substrate.

To allow turning, an articulated joint is added at the bottom. This articulated joint implies a rod that holds the prisms and that is pivot-mounted in two blocks with circular aperture. The turning can be influenced in its direction by small robe-like mounts or neighboring solid structures. One disadvantage of this concept is the bending of the hairs or prisms. They bend in a way that they contact each other (cf. Fig. 5.5 (a)) and, after they have turned in the articulated joint, the substrate surface. The contact with the substrate leads to a frustrated total internal reflection as discussed in Section 5.1.1 and hinders the silver appearance.

The second concepts yields more stability. Here, the edges of the prisms are oriented parallel to the substrate and perpendicular to the propagation direction of the laser beam.

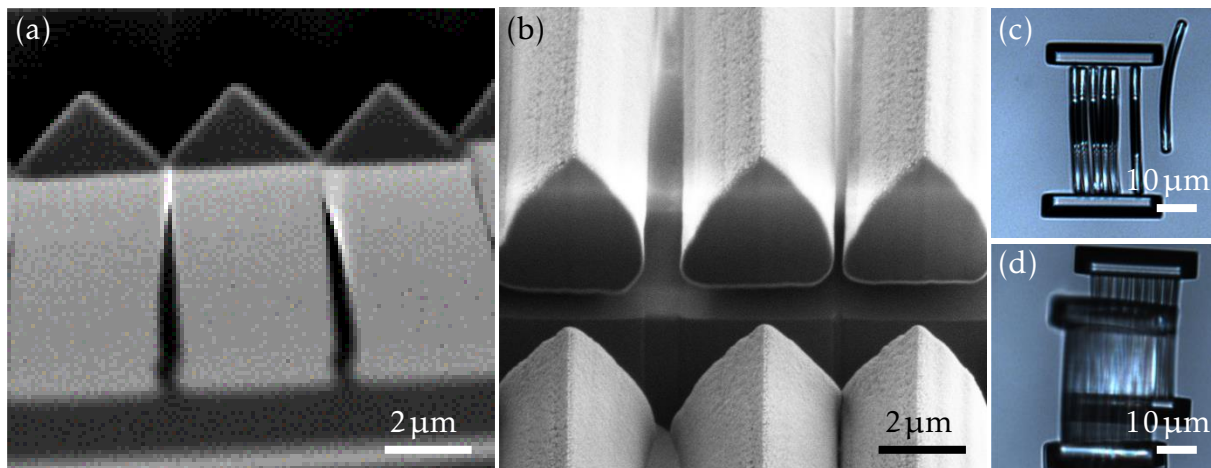


Figure 5.5: Model structures of the *Cataglyphis bombycina* fabricated in conventional photoresists (IP-Dip (a) and IP-L (b-d)): SEM images of (a) the realization with an orientation of the prisms parallel to the beam propagation and (b) the realization with an orientation of the prisms perpendicular to the beam propagation after focused ion beam (short: FIB) cutting. Light microscope images of (c) a single layer of prisms showing frustrated TIR in the middle due to a contact with the substrate and (d) an overlapping of prisms showing enhanced reflection.

To prevent a contact between the prisms and the substrate, the prisms are put on top of spacers. In this concept, the edges are defined by the axial voxel size, which is remarkably larger than in the lateral direction. Hence, the contour accuracy is smaller (cf. Fig. 5.5 (b)).

It turned out, that the lacking contour accuracy is no deal breaker, because the optic of the hairs is defined by the surfaces in between the edges. Light that hits the top of the prisms, i.e., near the upper edge, does not experience TIR in any case as the beams are redirected at the second side facet (cf. Fig. 5.2 (b) blue path). Light that hits the prism near the bottom edges is very likely reflected at the bottom facet, but these bottom edges are shadowed by the neighboring hairs. Hence, the effect of the large curvature radii of the edges is negligible. This observation is confirmed by the deviation of the original hairs from the prism shape [9].

Qualitative observations of the fabricated prisms indicate, that the optical properties of prisms correspond to the predictions in Section 5.1.1. The single hairs show a high reflectance that is reduced if the hairs bend down to the substrate (cf. Fig. 5.5 (c)) due to frustrated TIR. Furthermore, overlapping of two layers of prisms increases the reflectance as predicted above (cf. Fig. 5.5 (d)).

To explain the main aspects of the optical properties of the Saharan silver ant, the simple model of prism shaped hairs is sufficient. Snell's law and geometric optics explain the high reflectance and the silvery appearance. Due to the robustness of the properties against contour inaccuracies, the hairs can be easily mimicked. This robustness shows

5. Investigated biological systems

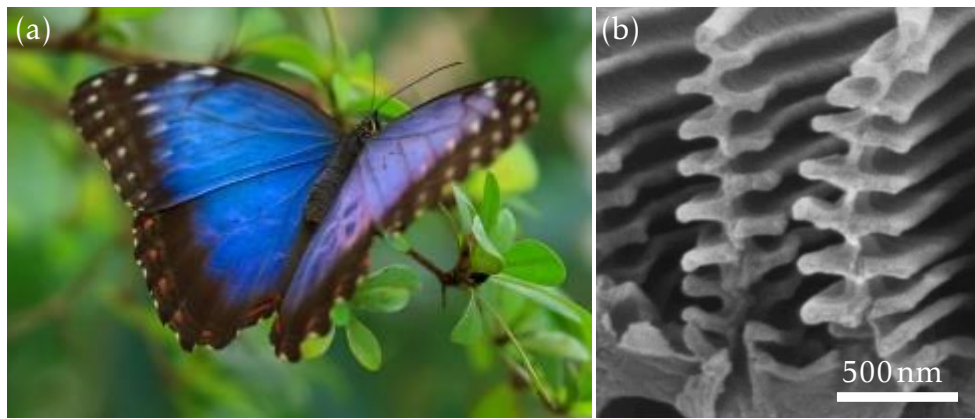


Figure 5.6: (a) Picture of a butterfly of the genus *Morpho* [167] and (b) a SEM picture of the christmas tree like structure on the wings of the butterflies of the genus *Morpho* after [168] licensed under CC by 4.0.

the effectiveness of these structures. Systems inspired by the Saharan silver ant like in [159,160] allow a reflection of visible light even in fabric to reduce the received radiation.

The following examples will illustrate what can be achieved, if deflection and the concept of PCs are considered.

5.2 Genus *Morpho* – the blue butterflies

A more complex structure is found in the butterflies of the genus *Morpho*. These butterflies live in Central and South America. Some of them exhibit a brilliant blue coloration (cf. Fig. 5.6 (a)) which they use for communication and to confound enemies [161]. These Blue *Morphos* have been studied extensively for a long time mainly because of their coloration [12, 153, 162–166]. The blue color cannot be explained by geometric optics, but still the underlying concept is relatively simple.

At the beginning of the 20th century scientists claimed, that the blue coloration is generated by multilayer interference of chitin and air layers. This prediction was motivated by the vanishing of the coloration when the wing is inserted in a liquid, which could fill the potential air layers [153, 162]. With electron microscopy, this assumption was proven in 1942 [169].

The wings of butterflies of the genus *Morpho* are covered with scales. The scales differ depending on their functions, the layer they are in and of course the exact butterfly species. However, their structure is similar.

The scales are covered with ridges in a certain nearly constant distance. A single ridge has a cross section, that looks like a Christmas tree (cf. Fig. 5.6 (b)). A trunk in the middle holds branches, which consist of thin layers and are also distributed nearly periodically. In further analogy to a Christmas tree, the layers or branches become smaller in their width perpendicular to the trunk from the bottom to the top for some sorts of scales [20, 161]. The branches at the different sides of the trunk may be shifted in their position

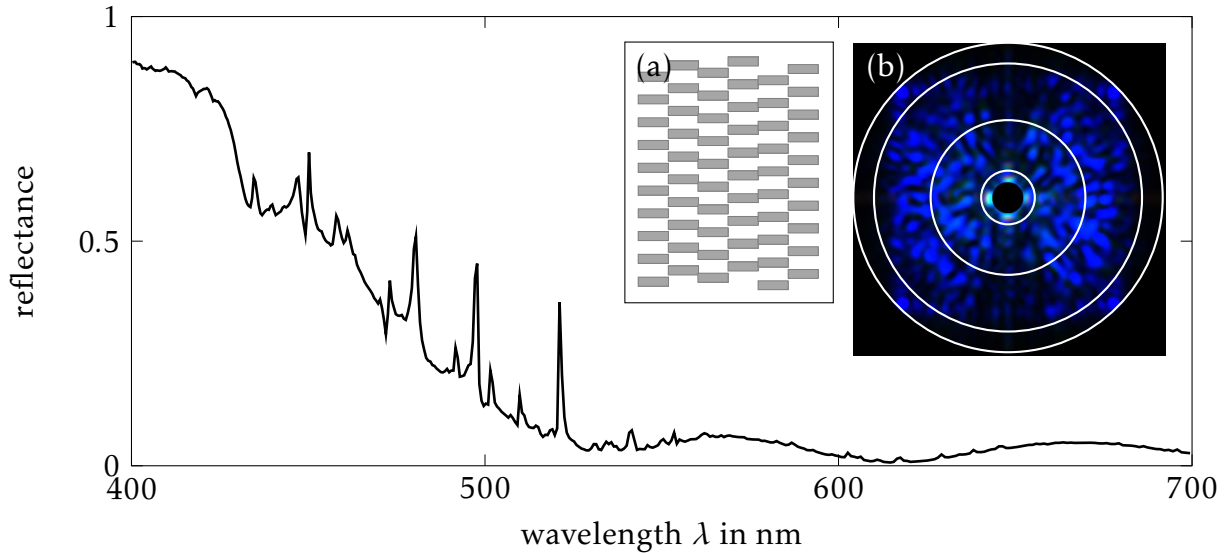


Figure 5.7: The reflectance and (inlet (b)) color impression in the farfield of a model system (cut view shown in inlet (a)) for the butterfly of the genus *Morpho*. The circles in (b) indicate an angle of deflection of 10° (inner circle), 30°, 60°, and 90° (outer circle), respectively. Reconstructed after [43].

by half a period [170]. Furthermore, the layers or branches are tilted towards the ground of the scale along a single ridge. This structure consists of chitin microfibrils and does not contain any pigments. Some scales exhibit pigments in the ground of the scale to absorb complementary colors [161].

The parameters of the Christmas tree structure depend on the exact kind of scale and, therefore, the desired function and coloration. The 4 to 12 [12, 171] chitin layers stacked on top of each other have a refractive index of around $n = 1.56$ due to the chitin microfibrils. These branches are around $d_c = 65\text{ nm}$ to $d_c = 80\text{ nm}$ thick. The intervening air layers are around $d_a = 60\text{ nm}$ to $d_a = 90\text{ nm}$ thick [12, 170–172]. For a strict periodic arrangement of air and chitin without any shifts or variation in width, this arrangement represents a Bragg reflector. It has a first order maximum in reflectance at a wavelength

$$\begin{aligned} \lambda &= 2(n_a d_a + n_c d_c), \\ \lambda &= 322\text{ nm to } 429\text{ nm}. \end{aligned} \quad (5.8)$$

This corresponds to a wavelength in the near UV or blue spectral range.

Such a strictly periodic Bragg reflector represents a 1D PC. It exhibits a high reflectance for a small spectral and angular range. So mainly light with the designated wavelength is reflected under normal incidence. In [170], a periodic Bragg reflector is used as a model system for the butterfly. It exhibits a high reflectance of up to around 90% for a small wavelength range of around 50 nm and an angular width of only 30° [170].

For the real scales, however, the maximum reflectance varies between 30% and 70% with a width of around 100 nm and over a broad angular range of around 90° to 100° [12, 171]. The broadening of the reflectance maximum is achieved by the introduction of disorder

5. Investigated biological systems

in a tailored way. In [173], the tailored disorder is achieved by, first, shifting the branches at each side of the trunk and, second, the offset of different ridges towards each other. FDTD calculation of the optical properties of a Christmas tree like structure with those modifications corresponds to the measurements of the butterflies [173].

Besides the Christmas tree model, a model without the vertical features (trunks) can be used (see inset Fig. 5.7 (a)) as in the work of D. T. Meiers [43,157]. For this model periodic Bragg stacks with a first order stop band in the blue spectral range and a base area of $(300 \times 300) \text{ nm}^2$ are used. Neighboring stacks are shifted towards each other by half a period of the stacks. Afterwards, they are shifted pairwise by a normally distributed offset perpendicular to the layers. A cut through the structure is sketched in the inset of Figure 5.7 (a)).

With this model system the blue coloration (mean reflectance of over 80% for wavelength $\lambda = 400 \text{ nm}$ to $\lambda = 425 \text{ nm}$) is achieved for a broad angular range of around 100° (from -50° to 50° cf. Fig. 5.7 inlet (b)). The angular broadening is comparable to the original scales.

This model shows that the effect of coloration (cf. Fig. 5.7) and broad angular distribution (cf. Fig. 5.7 inlet (b)) arises from the layered structure itself. The pigments in some species only further enhance the coloration by absorbing the other colors and especially the complementary color [161].

The *Morpho* butterflies use 1D PC to achieve their brilliant coloration. Higher dimensional PC allow higher selectivity of the reflected light, as presented in the next section.

5.3 *Entimus imperialis* – polarization effects

The beetle *Entimus imperialis* (cf. Fig. 5.8 (a)) can be found in the neotropic regions of South America and is between 16 mm and 40 mm long [174,175]. Its black elytra are covered with regularly arranged circular depressions colored in yellow-green, when viewed from the distance.

On closer examination, the depressions are covered with scales. These scales show areas, which either reflect turquoise-blue ($\lambda = 480 \text{ nm}$), cyan ($\lambda = 520 \text{ nm}$), green ($\lambda = 540 \text{ nm}$) and yellow-orange ($\lambda = 560$ to $\lambda = 610 \text{ nm}$) light (cf. Fig. 5.8 (b)). They enable a recognition between conspecifics. This coloration originates in a 3D PC structure, which exhibits different maxima in reflectance depending on the orientation of the crystal relative to the incident light. In the far field, these spectral reflectance maxima superimpose to the yellow-green impression, which provides a camouflage in their natural habitat. [175]

In Section 5.3.1 the 3D PC structure is introduced and the polarization-dependent reflectance of these beetles is analyzed. Three simplified models are presented and one of them, the woodpile structure, is fabricated using DLW in Section 5.3.2. Here, the polarization-dependent reflectance is observed, too.

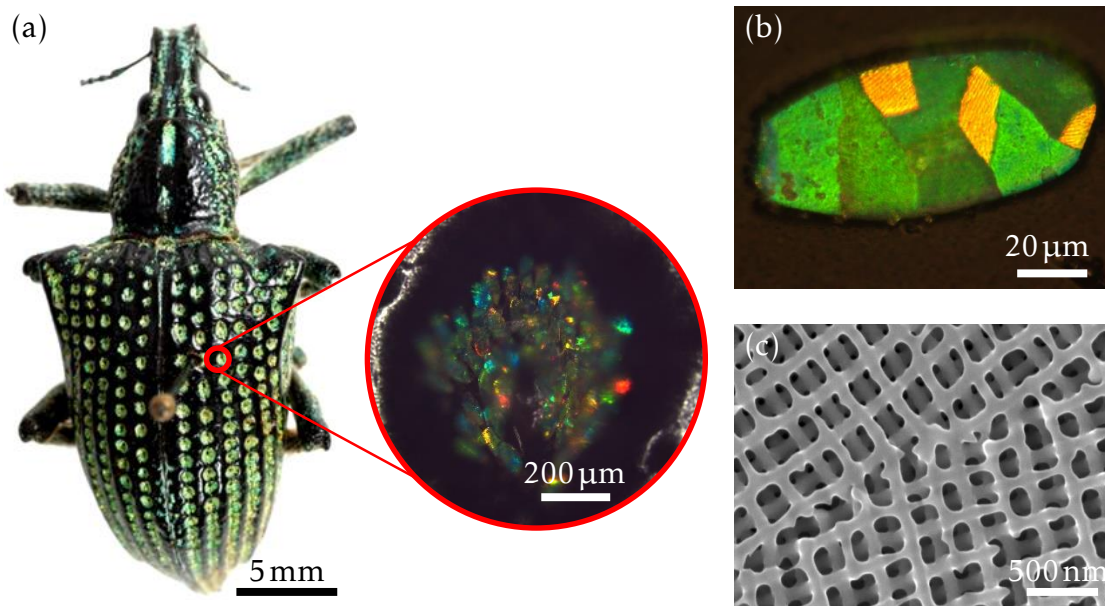


Figure 5.8: Pictures of (a) the beetle *Entimus imperialis* and as an inset a magnified image of a depression on its wing, (b) a single scale, and (c) a SEM image of a green scale. All images by courtesy of X. Wu.

5.3.1 The underlying concept of the reflection at *Entimus imperialis*

The structure inside the scales represents a biological realization of a diamond structure (D-structure) or in other words a face-center-cubic structure with a two atomic basis with identical atoms, which are shifted towards each other by one quarter of the space diagonal. The structure has a lattice constant of $a = 445 \text{ nm}$ [175].

In [176], the structure was described by the concept of stratified media with a 2D PC arrangement with a hexagonal symmetry and a periodicity of $286 \pm 3 \text{ nm}$ in-plane and a layer distance of 234 nm . The layers were arranged in a ABC sequence, which corresponds to an in-plane rotation of 120° between consecutive layers. The reflectance and transmittance of this model is calculated with the transfer matrix method. However, this model is not able to explain all spectral maxima in reflectance of the *Entimus imperialis*. [176]

With FDTD simulations of the D-structure the visible spectral reflectance maxima for all different colors of the *Entimus imperialis* are correlated to different crystallographic planes of the diamond structure in [175]. For most of the orientations of the PC structure, there is no polarization-dependency [175].

The green areas of the scales of the *Entimus imperialis* affect the polarization direction of the light during reflection. These green areas correspond to a crystal orientation, where the $\{001\}$ plane¹ is parallel to the scales surface. In this plane there are the two directions of the equivalence group of the $\langle 100 \rangle$ directions. Green light that is polarized along one of those directions is largely rotated by 90° in its polarization, so the polarization is afterwards parallel to the other direction of $\langle 100 \rangle$ group in this plane. The theoretical

¹See Appendix B for information about the bracket notation in crystallography.

5. Investigated biological systems

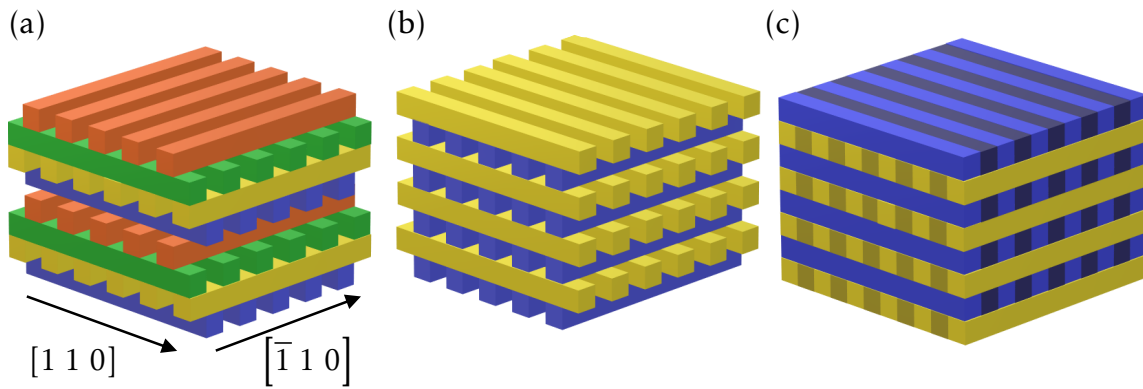


Figure 5.9: Bioinspired models for *Entimus imperialis*: (a) the woodpile structure ($ABA'B'$ sequence), (b) the crossed rods structure (AB sequence), and (c) the structure of crossed anisotropic layers

analysis of our collaboration group [13] shows, that up to 94% of the incident light, which is polarized along the $[0\ 1\ 0]$ direction belonging to the equivalence group of $\langle 1\ 0\ 0 \rangle$, is reflected with a rotated polarization. In the simulations less than 3% are reflected without a change in the polarization direction for a structure with ten unit cells. [13]

On the contrary, simulations for light that is polarized along a $\langle 1\ 1\ 0 \rangle$ direction reveal no cross-polarization reflection at all. This means, light that is polarized parallel to a symmetry plane of the structure, is not affected in its polarization direction during reflection. [13]

This behavior in reflection is analog to that of a wave plate with a phase difference of $\lambda/2$ in transmission, where the polarization of every wave is changed, except the wave is polarized along the fast or slow axis of the crystal. In the case of the beetle or the D-structure the fast and slow axis correspond to the $\langle 1\ 1\ 0 \rangle$ directions parallel to the symmetry planes. The D-structure of the *Entimus imperialis* does not affect the polarization of the incident light during transmission [13].

The effect of polarization conversion is found in model systems as well. The first model system is the woodpile PC (cf. Fig. 5.9 (a)). This structure is a D-structure itself. It consist of rods arranged in layers with a $ABA'B'$ sequence, where the A and B layers are perpendicularly arranged and the A and A' layers are shifted by half an in-plane period with respect to each other. The in-plane periodicity $a_{x,y}$ is constant for all layers and the layer distance is $a_z/4 = a_{x,y}/\sqrt{4}$ resulting in a out-of-plane periodicity of $a_z = \sqrt{2}a_{x,y}$. In the woodpile crystal the $\langle 1\ 1\ 0 \rangle$ directions of the crystal are oriented along the rods of the different layers, in the symmetry planes (cf. Fig. 5.9). In the simulations, the woodpile structures show a strong cross-polarization reflection which increases with the number of unit cells in the propagation direction of light [13].

This corresponds to the functionality of a PC (cf. Sec. 2.2) in general. The propagation properties of certain modes are predicted for an infinite number of unit cells and with a smaller volume or number of unit cells the properties deviate from the predicted properties. To achieve a full stop band for a certain wavelength or polarization direction, a

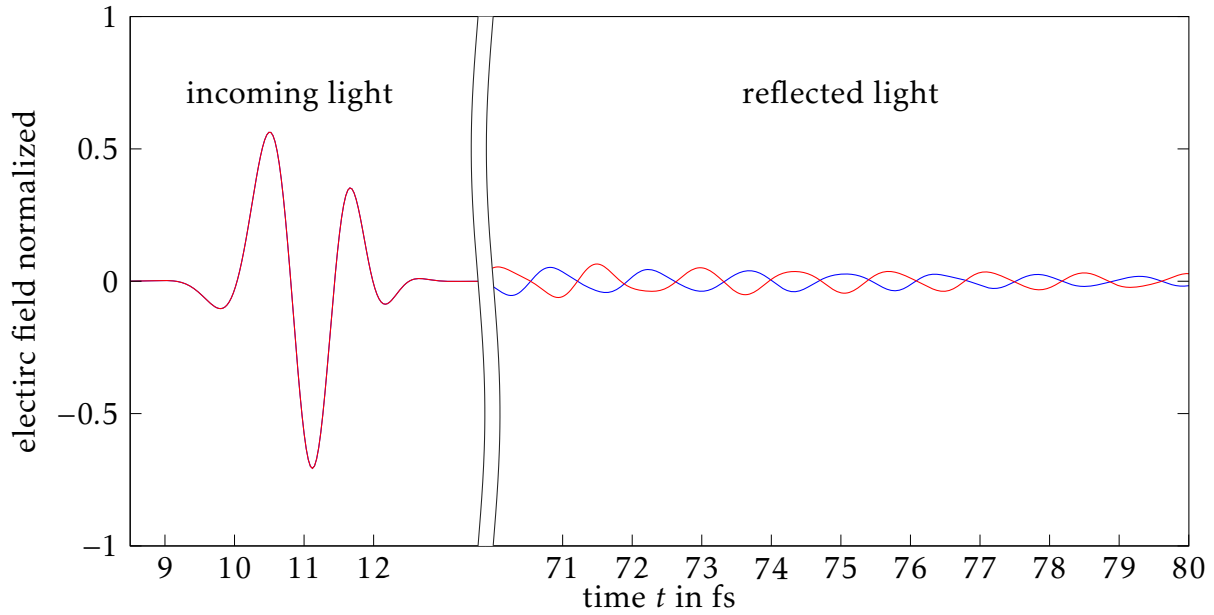


Figure 5.10: Phase shift for different polarization directions at a woodpile structure: Time resolved signal for different components E_x parallel to the $[1\ 1\ 0]$ direction (red) and E_y parallel to the $[1\ \bar{1}\ 0]$ direction (blue) of the electric field on the way towards the structure ($9\text{ fs} < t < 13\text{ fs}$) and back ($55\text{ fs} < t$).

minimum number of unit cells has to be provided [13] depending on the refractive index of the material.

While the woodpile structure is still complex, an even more simplified model system can be used: the crossed rods structure. Here, the rods are arranged in an AB sequence, where the rods of the different layers are oriented perpendicular to each other (cf. Fig. 5.9 (b)). For this model system with a strong simplification, the cross-polarization reflection is still visible. For 16 unit cells the cross-polarization is around 60%. [13]

Another simple model, which may be useful for the fabrication of corresponding structures, contains anisotropic layers with periodic refractive index profiles. Here, consecutive layers are rotated by 90° towards each other leading to the model structure with crossed anisotropic layers as indicated in Figure 5.9 (c)). It still shows cross-polarization if the incident light is polarized 45° towards the optical axis of the different layers and none if polarized along the optical axis. [13]

The simulations of our collaboration group also predict a conservation of the handedness of circular polarized light during reflection [13]. This conservation can be explained with the phase shifts that occur at the D-structure in reflection and in analogy to the phase differences at a half-wave plate in transmission.

In a half-wave plate, light that is polarized along the fast axis and light that is polarized along the slow axis of the crystal experience a phase shift of π which corresponds to an optical path difference of $\lambda/2$ in transmission [51]. For the D-structure, light that is polarized along the $[1\ 1\ 0]$ direction and light that is polarized along the $[1\ \bar{1}\ 0]$ direction

5. Investigated biological systems

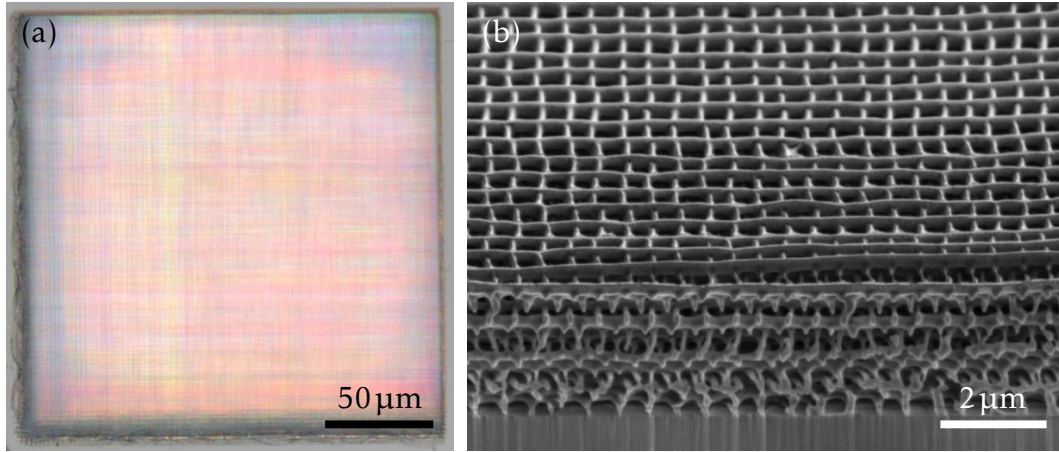


Figure 5.11: Fabricated model structure of the *Entimus imperialis*: (a) a light microscope image of the fabricated structure; (b) a SEM image of the structure after FIB cutting.

experience a corresponding phase shift of π during reflection, which was shown in FDTD simulations for a pulse falling on the structure (cf. Fig. 5.10).

For this simulation, the different components of the electric field are recorded over time at a position between the source of the wave and the structure. Hence, the signal was detected on its way to the structure ($9 \text{ fs} < t < 13 \text{ fs}$) and on its way back ($55 \text{ fs} < t$). While the different components E_x parallel to the $[1 \ 1 \ 0]$ direction (red curve in Fig. 5.10) and E_y parallel to the $[1 \ \bar{1} \ 0]$ direction (blue curve in Fig. 5.10) are in phase at the beginning (cf. left inlet in Fig. 5.10), they show a phase shift of π in the end (cf. right inlet in Fig. 5.10). This phase shift changes the handedness of circular polarized light in transmittance, but it preserves the handedness in reflection due to the reversion of the propagation direction.

The phase shift between the different polarization directions shown in Figure 5.10 corresponds to two times the optical path length of a single layer regarding an effective refractive index. This effective refractive index is in good agreement with an approach for the effective refractive index considering refractive indices of the different materials and their volume fraction ($n_{\text{eff}} = \sum_{i=0}^m n_m \frac{V_m}{V_{\text{ges}}}$). Therefore, the phase difference corresponds to one polarization direction being reflected at the first layer, while the other has to pass back and forth through this layer to be reflected at the second orthogonal layer.

5.3.2 Fabrication of polarization-dependent structures with DLW

After the simulations show the polarization-dependent reflectance for the woodpile structure this model system is chosen for the fabrication with DLW.

For a model system working at the same wavelength range than the original structure, a highly optimized DLW process is needed like in [83]. The small feature size and high resolution hinder the fabrication at the DLW setup presented in Section 3.2.1. These limitations are overcome by up-scaling of the systems to producible length scales. In case of a model system of the *Entimus imperialis*, the up-scaling of photonic structures changes

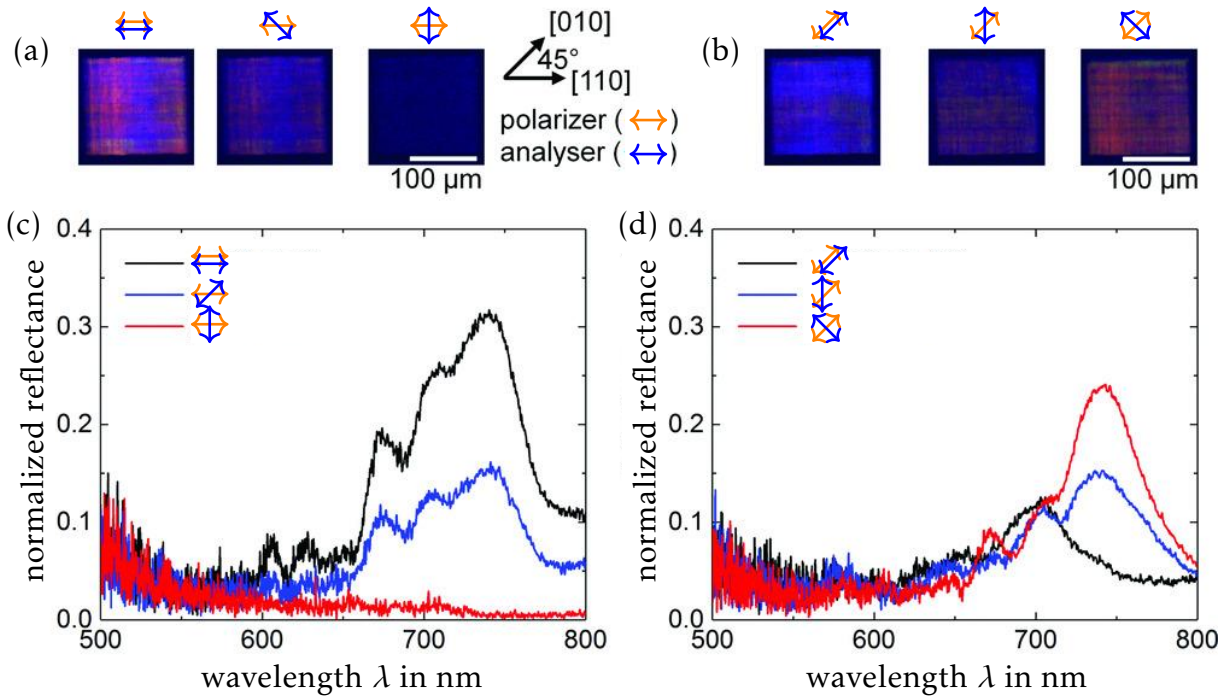


Figure 5.12: Polarization conversion at the model structure of *Entimus imperialis*: The polarization-dependent reflectance is observed (a,b) qualitatively and (c,d) quantitatively. The incident light is polarized with a polarizer (orange arrows), and the analyzer (blue arrows) filters the reflected light. The polarizer is oriented along (a,c) the $[1\ 1\ 0]$ and (b,d) the $[0\ 1\ 0]$ direction. Figure adapted with permission from [13]. ©WILEY-VCH Verlag GmbH & Co. KGaA, Weinheim

the affected wavelength range. However, the polarization conversion is still observed and proves to be robust against fabrication-induced disorder of the structure.

For a periodicity of $1\ \mu\text{m}$ instead of $445\ \text{nm}$, the structures are fabricated with a commercial DLW setup with the common photoresist IP-L (cf. Fig. 5.11). The wavelength range that exhibits a polarization conversion in reflection accordingly shifts from around $470\ \text{nm}$ to around $750\ \text{nm}$.

To observe the polarization conversion in reflection at the woodpile structures, the reflectance is observed with respect to its polarization. Therefore, the incident light is polarized along either the $\langle 1\ 1\ 0 \rangle$ direction parallel to the edges of the structure (cf. Fig. 5.12 (a,c)) or along the $[0\ 1\ 0]$ direction (cf. Fig. 5.12 (b,d)). The definition of the direction refers to the D-structure of the original scales (cf. Sec. 5.3).

For incident light polarized along the $[1\ 1\ 0]$ direction, there is no qualitative change in the polarization direction (cf. Fig. 5.12 (a)) nor a quantitative (cf. Fig. 5.12 (c)). Neither for $750\ \text{nm}$ nor for smaller wavelength, light or part of the light has changed its polarization direction. A large reflectance is observed, if polarizer and analyzer are oriented parallel to each other (left picture in Fig. 5.12 (a) and black curve in Fig. 5.12 (c)).

On the other hand, if light is polarized along the $[0\ 1\ 0]$ direction, i.e., 45° towards the edges of the structure, part of the reflected light at $750\ \text{nm}$ changes its polarization direc-

5. Investigated biological systems

tion (cf. Fig. 5.12 (d) red curve). The amount of light polarized in the incident direction is, by way of comparison, small (cf. Fig. 5.12 (d) black curve).

For smaller wavelengths, there is a negligible change in the polarization direction. Therefore, after the red light is rotated in its polarization direction, the sample appears blue, if analyzer and polarizer are oriented parallel to each other. If analyzer and polarizer are oriented perpendicular to each other, no light with short wavelength is observed, only the red light that changes its polarization direction is observed (cf. Fig. 5.12 (b)).

Thus, the polarization-dependent reflectance of the *Entimus imperialis* has been experimentally shown, though for a different wavelength range than for the natural structure due to the up-scaling of the model. The up-scaling helps to investigate different aspects in natural photonic structures.

The polarization-dependent reflectance observed in the scales of *Entimus imperialis* is explained by a photonic woodpile crystals. The photonic woodpile crystal allows to investigate the effects of the structure in an experimental realization for another wavelength range after up-scaling. While for the weevil *Entimus imperialis* the polarization-dependency of certain areas is limited to a small spectral range, the example of the white beetle *Cyphochillus insulanus* will show how the properties of a structure can be expanded to a broader spectral range and that an up-scaling of the structure does not necessarily mean a change in the affected wavelength range.

5.4 *Cyphochillus insulanus* – the white beetle

As a fourth example for nature's brilliancy concerning photonic structures, the white beetle *Cyphochillus insulanus* (cf. Fig. 5.13 (a)) is examined. The genus *Cyphochillus* is domiciled in Southeast Asia [177] and exhibits a brilliant whiteness. The whiteness arises from a disordered network-like structure within the scales covering the beetle's body (cf. Fig. 5.13 (b)). These scales (cf. Fig. 5.13 (c) and (d)) are around $7\ \mu\text{m}$ thick and consist of a scattering structure within a shell, both consist of chitin ($n_C = 1.55$ [154]). The network-like structure consists of chitin struts arranged in a layer-like way. The struts have a length of around $(1\ 105 \pm 360)$ nm and a diameter of around (230 ± 160) nm [27]. The beetle uses its white coloration to hide itself from its enemies among mushrooms [27].

The whiteness is comparable to that of artificial materials with a comparable refractive index, e.g., paper, although the responsible layer is a magnitude thinner. Accordingly, this structure belongs to the strongest scattering ones made out of a material with low refractive index [24]. This is what made the beetles of genus *Cyphochillus* subject of many investigations [25–28, 177, 178].

Scientists agree, that the layered structure leading to anisotropic optical properties of these beetle's scales is optimized for the highly efficient scattering through thousands of years of evolution [25, 27, 177]. The degree of optimization crystallizes in the fact, that even if the structure was made of a material with higher refractive index ($n = 2.8$), the reflectance would only increase from around 65% (for $n = 1.55$) to around 84% [27].

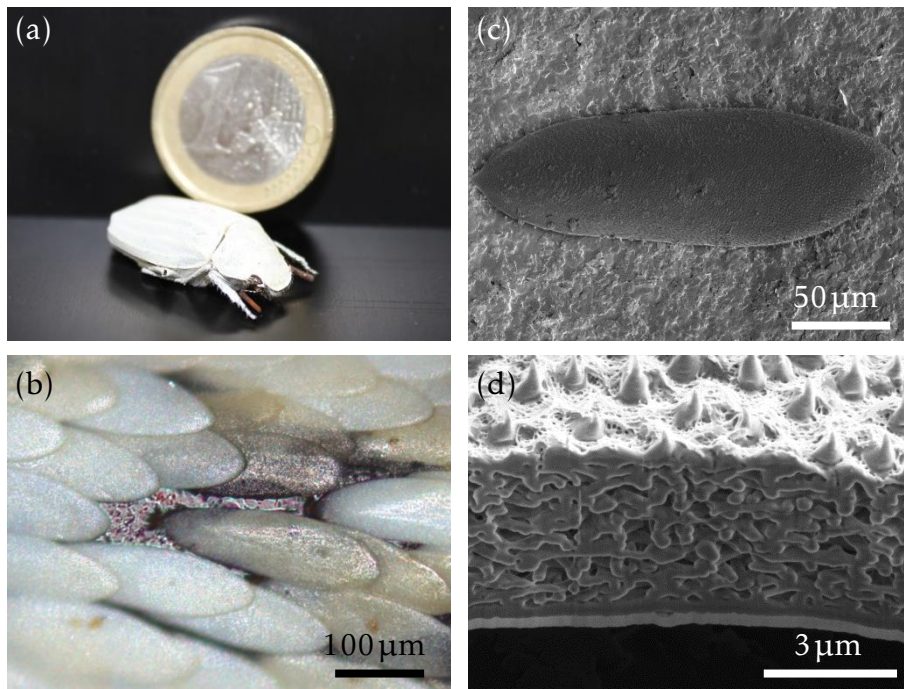


Figure 5.13: The white beetle – *Cyphochilus insulanus*: (a) a photograph of the beetle; (b) a light microscope image of scales; SEM images of (c) a single scale and (d) after FIB cutting.

Different attempts to find a model system describing the optical properties of the scales of these beetles have not led to satisfying agreement with the optical properties of the white beetle [25]. One problem has been that the underlying data for the structural parameters was received from SEM images of dried scales after focused ion beam (short: FIB) cutting. During the processing, the scales deform and, hence, the obtained data exhibits large fluctuations [27, 179]. A structural characterization with less deformations than in former publications is obtained by cryo-ptychographic X-ray computed tomography [27], leading to more reliable structural parameters and an one-to-one-model of the structure.

With these parameters a model of the layers inside the scales of *Cyphochilus insulanus* is developed and analyzed with FDTD simulations (cf. Sec. 5.4.1). The developed structure is adapted to allow a fabrication with DLW as presented in Section 5.4.2.

5.4.1 The underlying concept in the scales of *Cyphochilus insulanus*

Based on the parameters of the structure presented in literature (mainly in [27]) and considering a layered structure, a model system is presented, which has been developed during the diploma thesis of D.T. Meiers [43, 157]. The model system is based on a periodic Bragg stack model imitating the layer-like structure of the beetle's chitin network. It is a similar starting point as for the model describing the *Morpho* butterflies in Section 5.2 but with different results due to different disordered disturbances. In case of the white beetle, the periodicity is disturbed in different steps, depending on the desired degree of accordance with the optical properties of the white beetle. Therefore, different parame-

5. Investigated biological systems

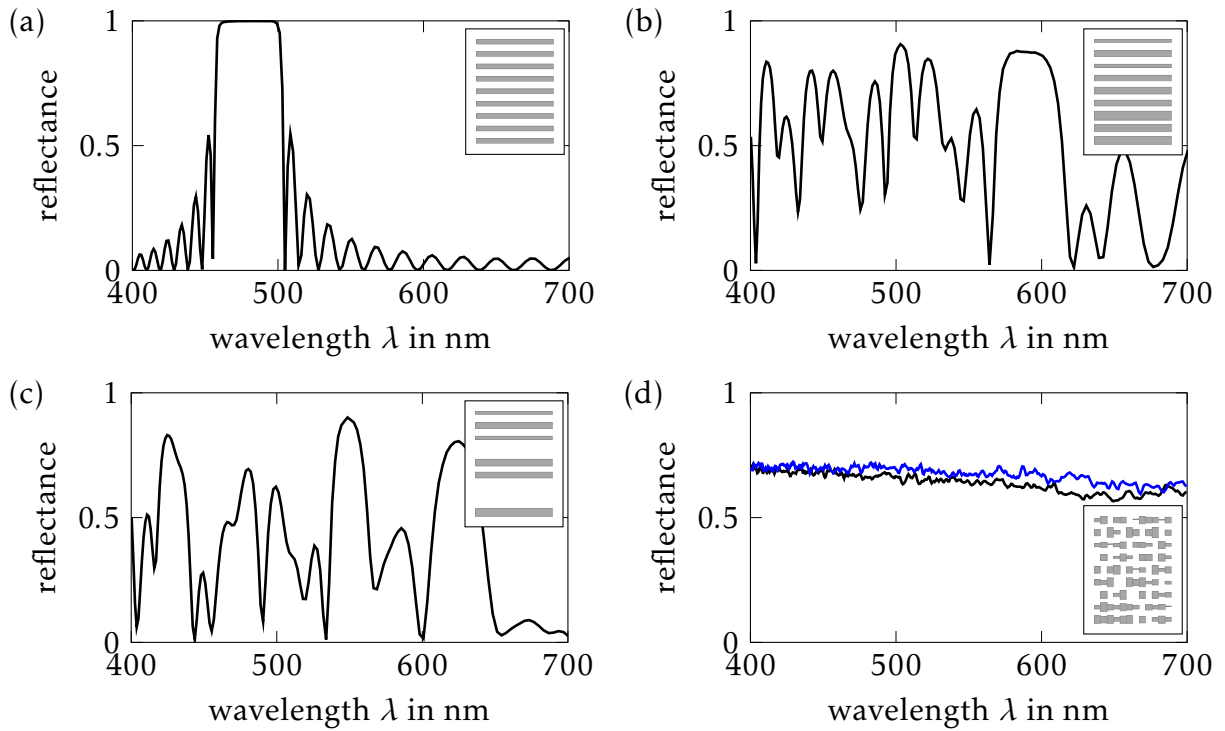


Figure 5.14: Different steps towards a model system for the white beetle and their reflectance: the reflectance of (a) a periodic Bragg stack, (b) a stack with varying layer thickness, (c) as (b) with left out layers, and (d) a composition of different stacks (black) and the one-to-one model from [27] (blue). Corresponding sketches of the cut views of the structures are shown as inlets. Reconstructed after [157].

ters of the structure are varied according to different distributions. These distributions are extracted from the investigations of the exact one-to-one model presented in [27]. All quantities are normally distributed.

The periodic Bragg stack, which serves as a starting point for the model, exhibits a layer thickness of the chitin layers of $d_C = 230\text{nm}$. This thickness is chosen equal to the mean thickness of the chitin struts determined in [27]. The air layers are defined by the condition for an ideal Bragg stack with two layers of the same optical thickness $d_A = n_C d_C = 357\text{nm}$. This Bragg stack reveals a first order stop-band in the infrared range $\lambda_1 = 4d_A = 1426\text{nm}$ and, hence, a second order stop-band at $\lambda_2 = 475\text{nm}$ in the visible spectral range. The corresponding reflectance spectrum for the visible spectral range of a structure with 12 layers, resulting in a total thickness of $d_{\text{tot}} = 6.7\mu\text{m}$, and a sketch of a cut through the structure is presented in Figure 5.14 (a).

The second order stop-band of the periodic Bragg stack in the visible spectral range allows high reflection only for a small spectral range of around $\Delta\lambda = 50\text{nm}$. This higher order stopband is sensible to disturbances and, thus, used for adjusting the properties of the structure. To enhance the overall reflectance of the structure, the layer thickness is modified. Therefore, the chitin layers are adapted in their thicknesses according to the thickness distribution of the struts in the one-to-one-model presented in [27]. The resulting structure is similar to those found in metallic appearing animals like certain beetles

or fishes [19,21–23]. In the reflectance spectrum of the structure the original stop-band in the visible spectral range is decreased, but the overall reflectance is increased (cf. Fig.5.14 (b)).

To take into consideration, that in the exact model the distance between neighboring layers is at some points much higher than at others, one third of the layers are left out randomly. This reduces the filling fraction. The filling fraction of the final structure is around 31% [43], which corresponds to the filling fraction of the original scales (45% to 31% [27, 60, 179]). The smaller filling fraction also prevents optical crowding, hence, there is no spatial correlation that could lead to a reduced scattering. The reduction of layers reduces the reflectance slightly and leads to larger irregularities in the reflectance (cf. Fig. 5.14 (c)) that vanish if the reflectance is averaged over different configurations.

The averaging, over different stacks with different distribution for the layer thickness and different layers left out, smooths the reflectance. Furthermore, it prevents a silver appearance. Therefore, the next modification is to assemble the whole structure out of small stacks. The base area of a single stack is $(300 \times 300) \text{ nm}^2$. This leads to the predicted smooth reflectance shown in Figure 5.14 (d) (black line) for the visible spectral range. This spectrum shows qualitatively the same behavior as the spectrum of the one-to-one model from [27] (Fig. 5.14 (d) blue line), while the overall thickness is comparable ($d_{1:1} = 7 \mu\text{m}$ and $d_{\text{model}} \approx 6.7 \mu\text{m}$).

To prove that there is no silvery appearance as in the structures mentioned in [19,21–23], the optical impression of the presented model system is calculated from the results of the FDTD simulations. Therefore, the intensity distribution in the near field in reflection is transferred into a far field intensity distribution by the used FDTD software FDTD-Solutions from the Ansys Canada Ltd. The software therefore uses Fourier optics by predicting plane wave propagation. With the intensity distribution in the far field for a chosen number of frequencies in the visible spectral range, corresponding RGB values can be calculated with the method presented in [180]. These RGB values demand a normalization of the single values to avoid oversaturation. They are normalized such that the mean value of the overall RGB values is the same for the different calculated color impressions.

For the exact model of a part of a scale from [27], the calculated color impression is presented in Figure 5.15 (a). In the middle of the pattern, the calculation yields white spots due to the slightly higher intensity in the specular reflex. In the periphery, colored spots appear, but no sharp diffraction pattern is recognizable. The colored far field pattern for the developed model system looks qualitatively the same (cf. Fig. 5.15 (b)).

The calculated color pattern derives from small structures of around $(7 \times 7 \times 7) \mu\text{m}^3$. The resolution power of the human eye is not high enough for those small structures. Hence, the noticed color impression corresponds to an averaging about different small structures. For the one-to-one model, this results in a white appearance. As the farfield color impressions and the overall reflectance values agree, the real color impression of the de-

5. Investigated biological systems

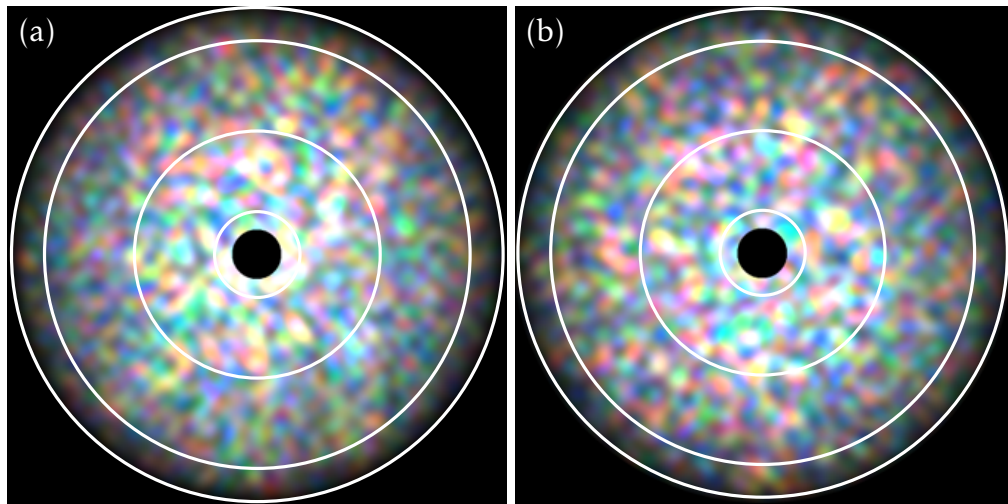


Figure 5.15: Calculated color impression of the farfield of (a) the one-to-one model and (b) the developed model system in the half space of reflection. The circles indicate an angle of deflection of 10° , 30° , 60° , and 90° , respectively. Reconstructed after [43].

veloped model system should qualitatively also agree with the one-to-one-model. Hence, it should appear white, too.

As mentioned above, the undisturbed Bragg stack has its first order stop-band in the infrared range at $\lambda_1 = 1426\text{ nm}$. This first order stop-band is disturbed less by disorder than the higher order stop-bands [181, 182] and, hence, the maximum in reflectance is clearly visible in the spectrum of the developed model in Figure 5.16 (black line). The spectrum of the exact model does not show this feature (cf. Fig. 5.16 blue line). Therefore, if the optical properties of the white beetle in the IR range should be reproduced, further modifications of the model system are necessary.

One possible way is to adapt the distances of the layers. If these distances are varied according to a normal distribution in the range of 350 nm to 800 nm around the mean value of 587 nm with a standard deviation of 100 nm, the sharp maximum at $\lambda_1 = 1426\text{ nm}$ is smoothed (cf. Fig. 5.16 red line). The resulting spectrum resembles the exact model (blue line) more than the model system with constant layer distances, especially for the visible spectral range, but still shows some deviations in the near infrared range.

For an exact agreement in the infrared range, more modifications are needed, but for a bioinspired structure with the same optical properties in the visible spectral range, the spectra and the color impression of the far field show, that the model system with constant layer distances is sufficient. This model system also allows the usage of high reflectance of a certain range in the IR, e.g., to reflect heat radiation. Furthermore, the presented model system exhibits the optical anisotropy observed in [24, 25, 27], which allows strong scattering and reflection perpendicular to the surface of the scale while the reflection in the direction of the layers is smaller in comparison (around 0.1 smaller in the visible spectral range) [43].

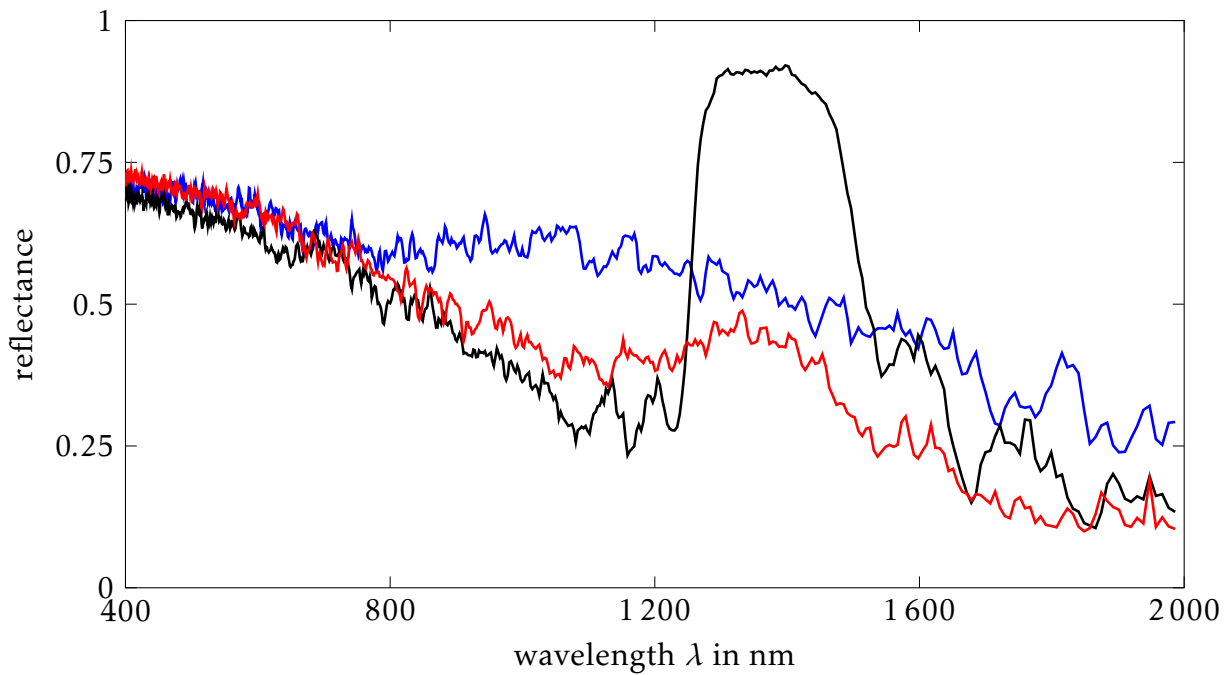


Figure 5.16: The reflectance spectra of the one-to-one model (blue line), the developed model system (black line), and the modified model (red line). Reconstructed after [43].

The strong scattering is also represented in a long lifetime of light inside the structure of around 140 fs and a short transport mean free path of $(1.46 \pm 0.04) \mu\text{m}$ which corresponds to the experimental values in [24] of 140 fs and $(1.47 \pm 0.07) \mu\text{m}$, respectively. [43]

As the underlying principle and the order of magnitude of the features of the model system agrees with the model system used in Section 5.2 to achieve brilliant coloration, this model system proves the transition of brilliant coloration to whiteness due to the amount of disorder predicted by P. Vukusic in [26]. Due to its layered structure the model system enables fabrication with DLW.

5.4.2 Fabrication of white, disordered structures with DLW

The disordered, network-like structure within the scales of *Cyphochillus insulanus* uses the second order stop band of the original Bragg stack that is sensitive to disorder to create the whiteness. It is also possible to use higher order stop bands of the original Bragg stack. This allows up-scaling to length scales that are accessible for fabrication with DLW without changing the effect on the originally effected wavelength range.

While the model is simulated with separated layers, this is not fabricable. Therefore, the fabricated structures need an additional framework for stability. In the scales, the layers are held by the shell of the scales and vertical features inside the network. For the fabrication with DLW, a corresponding support structure is added. Pillars are added between neighboring layers at regularly arranged positions and an additional external framework fixes the layers. For this framework, different concepts are possible, simple

5. Investigated biological systems

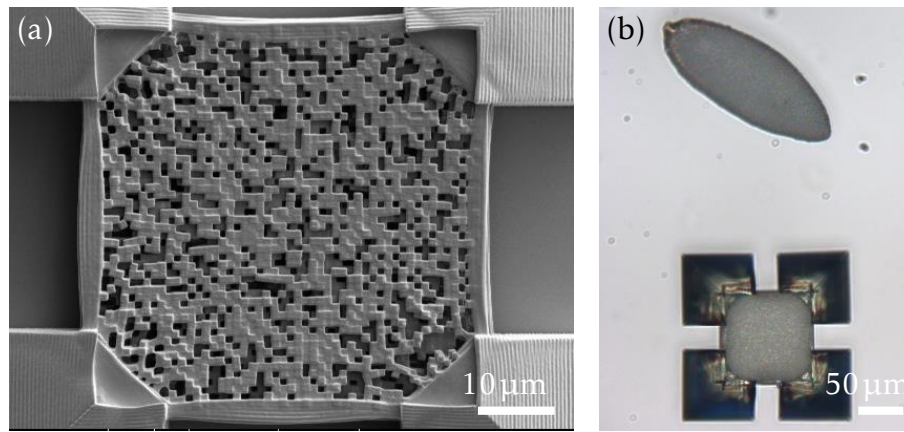


Figure 5.17: Fabricated model structure of the *Cyphochillus insulanus*: (a) SEM image of the structure fabricated in conventional resist (IP-L) and (b) a corresponding structure in comparison with the original scales [43].

solid frames as well as lightweight constructions building a rectangular or round shaped frame.

The fabrication in a conventional photoresist (IP-L; cf. Fig. 5.17 (a)) leads to a qualitative correspondence in the optical properties compared to the original scales as can be seen in the light microscope image in Figure 5.17 (b). The variation in the layer thickness is achieved by a variation in the laser power during the writing process. Because a variation in the laser power leads to a variation in the voxel size and, hence, the feature size, especially in the axial direction. The supporting framework and the structure are written within one step by further adjusting the laser dose, such that the framework achieves the necessary stability and cross-linking density, which is needed to support the layers.

The complex photonic structure of the beetle *Cyphochillus insulanus*, which is optimized by nature through thousands of years of evolution to strongly scatter the light, is mimicked using a model system with a simple underlying concept. This simple model uses only few parameters which can be varied independently. Furthermore, due to the layered structure this concept allows fabrication of bioinspired structures in conventional resist and in cellulose-based resists (cf. Sec. 4.4), which are described in Chapter 4.

Chapter 6

Conclusions

Two aspects of biomimetics in micro- and nano-photonics are addressed in this work, the use of bioinspired materials in the fabrication of micro- and nano-structures and the identification of the underlying concepts of natural photonic structures.

To tackle potential material dependencies of the natural photonic structures in form of a material induced disorder, a cellulose-based photoresist for direct laser writing is developed. For this resist, three kinds of cellulose derivatives are tested in combination with different initiators and solvents. The best performance is achieved for a resist with methacrylated cellulose acetates with a degree of polymerization of $DP = 500$ (MACA500), 2-Isopropyl-9H-thioxanthen-9-one (ITX), and dimethyl sulfoxide (DMSO). MACA500 is a short polymer that takes over the role of the monomers in common resists. It is solved in DMSO and polymerized with the initiator ITX. The methacrylic groups of the MACA500 enable a cross-linking of the molecules with a radical polymerization and the acetate groups allow solving the cellulose derivative in common organic solvents, like DMSO.

The resist with MACA500 allows for reproducible structuring. The reproducibility is only possible if solvents with a low fugacity are used, such that the resist composition does not change between different applications and during the writing process. The molar concentrations of the cellulose derivative and the initiator indicates a poor quantum yield of the reaction process. Despite the poor quantum yield, direct laser writing is possible at affordable laser powers ($\ll 50$ mW).

The written structures exhibit a feature size down to 130 nm. In the lateral direction, perpendicular to the beam propagation, they reach a resolution of the features down to 600 nm and 2.1 μ m in the axial direction. The cross-linking density enables stable 3D structures and, with the achieved resolution, it is possible to fabricate biomimetic structures in this cellulose-based resist.

The results for the cellulose-based resist can be transferred to other polysaccharides, like chitin. With comparable functionalization, these polysaccharides might also be suitable for direct laser writing. Furthermore, the reaction efficiency of the resist using cellulose

6. Conclusions

might be improved if other functional groups, e.g., acrylic groups instead of methacrylic groups, are used. This may enable the use of shorter cellulose derivatives that, due to their smaller size, may enable higher resolutions.

Our cellulose-based resists pave the way for polysaccharides into micro- and nano-structuring. They enable different kinds of structures ranging from fine-featured porous materials for filters to larger solid structures used as cell scaffolds.

Besides the material aspect, the structural aspect of natural photonic structures is investigated. Therefore, models are identified that mimic the optical properties of the different natural photonic nanostructures in the visible spectral range. The photonic structure in the silver ant, *Cataglyphis bombycina*, is reduced to a basic model of prisms: The prism-shaped hairs use total internal reflection to create a silver appearance. This simple model enables the fabrication with direct laser writing.

The diamond structure in the scales of the beetle *Entimus imperialis* can change the polarization direction of light. This effect is mimicked by different models in simulations and it is observed for a fabricated model system of a photonic woodpile crystal. The woodpile crystal is scaled up to allow fabrication. Therefore, the investigated wavelength range shifts to larger wavelengths. The effect of a change in the polarization direction of reflected light remains.

The photonic structures in the blue butterfly of the genus *Morpho* and the structures in the white beetle, *Cyphochilus insulanus*, are both imitated in their optical properties by models based on a periodic Bragg stack. For the butterflies, only an equally distributed offset for pairs of stacks is needed to achieve the blue coloration in a broad angular range. A pair contains two stacks that are shifted towards each other by half a period.

To achieve the whiteness of the *Cyphochilus insulanus*, more disorder has to be introduced compared to the blue butterfly. This disorder includes the equal distribution of the layer thickness, the leaving out of one third of the layers at random positions, and additionally the composition of the whole sample out of small modified Bragg stacks, which differ from each other. The combination of these modifications broadens the effect of the original Bragg stack not only in the angular but also in the spectral range.

The disordered Bragg stack model of the *Cyphochilus insulanus* has the same optical properties as the original scales in the visible spectral range. This is shown in the simulations as well as in a qualitative comparison of the direct laser written structure with the original scale. The developed model is adaptable in its properties by changing the parameters of the introduced distributions.

The analysis of the natural photonic structures has shown material independence of the different effects. The different effects from reflectivity over coloration to scattering, thus, can be generated in different transparent materials. In addition to the visible effects, other effects such as the long lifetime of the photons in the model structures of the white beetle can be used, for example, wherever a long dwell time of the light in the material leads to an increase in efficiency, such as in catalysts for hydrogen production.

Together with the cellulose-based resist, the discussed bioinspired structures might lead to environmentally suitable applications in photonics that make optimal use of these materials.

6. Conclusions

Appendix A

The operator $\hat{\Theta}$

In Section 2.2.1 the operator $\hat{\Theta}$ is introduced to express the master equation for PCs (cf. Eq. 2.20). This operator is defined as:

$$\hat{\Theta}\vec{H}(\vec{x}) = \nabla \times \left[\frac{1}{\epsilon_r(\vec{x})} \nabla \times \vec{H}(\vec{x}) \right]. \quad (\text{A.1})$$

For the solution of the master equation for PCs, it is required that $\hat{\Theta}$ is a linear Hermitian operator. The linearity of the operator $\hat{\Theta}$ is shown in the first section and in Section A.2, it is shown, that $\hat{\Theta}$ is an Hermitian operator.

A.1 A linear operator

In general, an operator \hat{A} is called linear if:

$$\hat{A}(a_1 f_1 + a_2 f_2) = a_1 \hat{A} f_1 + a_2 \hat{A} f_2, \quad (\text{A.2})$$

with f_j elements of the space that the operator is defined upon and a_j scalars.

In the case of the operator $\hat{\Theta}$ (cf. Eq. A.1), the following expression has to be examined:

$$\hat{\Theta} [a_1 \vec{H}_1(\vec{x}) + a_2 \vec{H}_2(\vec{x})] = \nabla \times \left\{ \frac{1}{\epsilon_r(\vec{x})} \nabla \times [a_1 \vec{H}_1(\vec{x}) + a_2 \vec{H}_2(\vec{x})] \right\}. \quad (\text{A.3})$$

$\nabla \times \vec{H}(\vec{x})$ is the rotation of the magnetic field, which is linear (see [183, 184] and comparable basic literature). Therefore, and due to the linearity of a multiplication, the above mentioned equation is rewritten to:

$$\begin{aligned} \hat{\Theta} [a_1 \vec{H}_1(\vec{x}) + a_2 \vec{H}_2(\vec{x})] &= \nabla \times \left\{ \frac{1}{\epsilon_r(\vec{x})} [a_1 \nabla \times \vec{H}_1(\vec{x}) + a_2 \nabla \times \vec{H}_2(\vec{x})] \right\} \\ &= \nabla \times \left[a_1 \frac{1}{\epsilon_r(\vec{x})} \nabla \times \vec{H}_1(\vec{x}) + a_2 \frac{1}{\epsilon_r(\vec{x})} \nabla \times \vec{H}_2(\vec{x}) \right]. \end{aligned} \quad (\text{A.4})$$

In a last step the linearity of the rotation is used for another redraft:

$$\hat{\Theta} [a_1 \vec{H}_1(\vec{x}) + a_2 \vec{H}_2(\vec{x})] = a_1 \nabla \times \frac{1}{\epsilon_r(\vec{x})} \nabla \times \vec{H}_1(\vec{x}) + a_2 \nabla \times \frac{1}{\epsilon_r(\vec{x})} \nabla \times \vec{H}_2(\vec{x}). \quad (\text{A.5})$$

A. The operator $\hat{\Theta}$

This last version of the equation is equivalent to

$$\hat{\Theta} [a_1 \vec{H}_1(\vec{x}) + a_2 \vec{H}_2(\vec{x})] = a_1 \hat{\Theta} \vec{H}_1(\vec{x}) + a_2 \hat{\Theta} \vec{H}_2(\vec{x}) . \quad (\text{A.6})$$

Equation A.6 corresponds to the definition of linearity mentioned in Equation A.2 for the operator $\hat{\Theta}$.

A.2 A Hermitian operator

An operator is an Hermitian operator if:

$$\langle f_1 | \hat{A} f_2 \rangle = \langle \hat{A} f_1 | f_2 \rangle , \quad (\text{A.7})$$

with the inner product $\langle f_1 | f_2 \rangle$. For the operator $\hat{\Theta}$ this means:

$$\langle \vec{H}_1(\vec{x}) | \hat{\Theta} \vec{H}_2(\vec{x}) \rangle = \langle \hat{\Theta} \vec{H}_1(\vec{x}) | \vec{H}_2(\vec{x}) \rangle , \quad (\text{A.8})$$

with

$$\langle \vec{H}_1(\vec{x}) | \hat{\Theta} \vec{H}_2(\vec{x}) \rangle = \int \vec{H}_1^*(\vec{x}) \hat{\Theta} \vec{H}_2(\vec{x}) dV , \quad (\text{A.9})$$

where $\vec{H}_1^*(\vec{x})$ is the complex conjugate wave function $\vec{H}_1(\vec{x})$. If the operator is written out, the integral can be transformed with the help of the relation [183]:

$$\nabla \cdot [\vec{A}(\vec{x}) \times \vec{B}(\vec{x})] = -\vec{A}(\vec{x}) \cdot [\nabla \times \vec{B}(\vec{x})] + [\nabla \times \vec{A}(\vec{x})] \cdot \vec{B}(\vec{x}) \quad (\text{A.10})$$

to:

$$\begin{aligned} \langle \vec{H}_1(\vec{x}) | \hat{\Theta} \vec{H}_2(\vec{x}) \rangle &= \int \vec{H}_1^*(\vec{x}) \hat{\Theta} \vec{H}_2(\vec{x}) dV \\ &= \int \vec{H}_1^*(\vec{x}) \cdot \nabla \times \left[\frac{1}{\epsilon_r(\vec{x})} \nabla \times \vec{H}_2(\vec{x}) \right] dV \\ &= \int \frac{1}{\epsilon_r(\vec{x})} [\nabla \times \vec{H}_1^*(\vec{x})] \cdot [\nabla \times \vec{H}_2(\vec{x})] dV \\ &\quad - \int \nabla \cdot \left\{ \frac{1}{\epsilon_r(\vec{x})} \vec{H}_1^*(\vec{x}) \times [\nabla \times \vec{H}_2(\vec{x})] \right\} dV \\ &= \int \nabla \times \left[\frac{1}{\epsilon_r(\vec{x})} \nabla \times \vec{H}_1^*(\vec{x}) \right] \cdot \vec{H}_2(\vec{x}) dV \\ &\quad - \int \nabla \cdot \left\{ \frac{1}{\epsilon_r(\vec{x})} [\nabla \times \vec{H}_1^*] \times \vec{H}_2(\vec{x}) \right\} dV \\ &\quad - \int \nabla \cdot \left\{ \frac{1}{\epsilon_r(\vec{x})} \vec{H}_1^*(\vec{x}) \times [\nabla \times \vec{H}_2(\vec{x})] \right\} dV \\ &= \langle \hat{\Theta} \vec{H}_1 | \vec{H}_2 \rangle \\ &\quad - \int \nabla \cdot \left\{ \frac{1}{\epsilon_r(\vec{x})} [\nabla \times \vec{H}_1^*] \times \vec{H}_2(\vec{x}) \right\} dV \\ &\quad - \int \nabla \cdot \left\{ \frac{1}{\epsilon_r(\vec{x})} \vec{H}_1^*(\vec{x}) \times [\nabla \times \vec{H}_2(\vec{x})] \right\} dV . \end{aligned} \quad (\text{A.11})$$

The remaining integrals can be transformed with Gauss' theorem to integrals over closed surfaces:

$$\begin{aligned}
\langle \vec{H}_1(\vec{x}) | \hat{\Theta} \vec{H}_2(\vec{x}) \rangle &= \langle \hat{\Theta} \vec{H}_1(\vec{x}) | \vec{H}_2(\vec{x}) \rangle \\
&\quad - \oint \left\{ \frac{1}{\epsilon_r(\vec{x})} [\nabla \times \vec{H}_1^*] \times \vec{H}_2(\vec{x}) \right\} \vec{n} dS \\
&\quad - \oint \left\{ \frac{1}{\epsilon_r(\vec{x})} \vec{H}_1^*(\vec{x}) \times [\nabla \times \vec{H}_2(\vec{x})] \right\} \vec{n} dS,
\end{aligned} \tag{A.12}$$

where \vec{n} is the surface-normal unit vector. These integrals over closed surfaces are equal to zero, due to periodic boundary conditions [185]. The remaining first line proves that $\hat{\Theta}$ is an Hermitian operator.

A. The operator $\hat{\Theta}$

Appendix B

Introduction to the notation in crystallography

Crystallography uses the periodicity of the crystals to describe points, directions and planes inside the crystal. The different notations that are based upon [186, 187] are shortly explained in this appendix.

A point of the grid \vec{x} can be expressed with a linear combination of the grid vectors \vec{a}_j

$$\vec{x} = \sum_j^3 o_j \vec{a}_j, \quad (\text{B.1})$$

if the origin is at a point of the grid, too. Therefore, every point of the grid is well-defined by the triple of numbers o_j . Negative numbers are expressed with a bar over the number $\bar{o}_j = -o_j$. Points are expressed without brackets, e.g., the point 1 1 1 is marked in Figure B.1 (green).

The notation for directions and grid lines bases upon this notation of points. To express a direction, the origin of the system is used as a reference. The point of the grid that is reached from the origin in the wanted direction reveals the notation for this direction. To describe directions and grid lines, the triplet of smallest integers with the same proportion is used in square brackets. For example, [1 0 0] describes all parallel directions or lines that are marked in red in Figure B.1.

If symmetries are considered, some of the directions which are not parallel are still equivalent. This means that they can be transferred into each other by symmetry operations that reproduce the crystal. For example, for a primitive cubic crystal, all edges are equivalent. If the cube is turned, the edges are transferred into each other without changing the crystal. Face diagonals can not be transferred into edges without changing the crystalline structure. These equivalent directions are expressed in angle brackets. So all edges of the cubes (red, blue, and grey lines in Fig. B.1) are part of the $\langle 1 0 0 \rangle$ group.

Planes are described in crystallography by the so-called Miller indices. They represent the inverse of the penetration point of an axis along the grid vector through the plane.

B. Introduction to the notation in crystallography

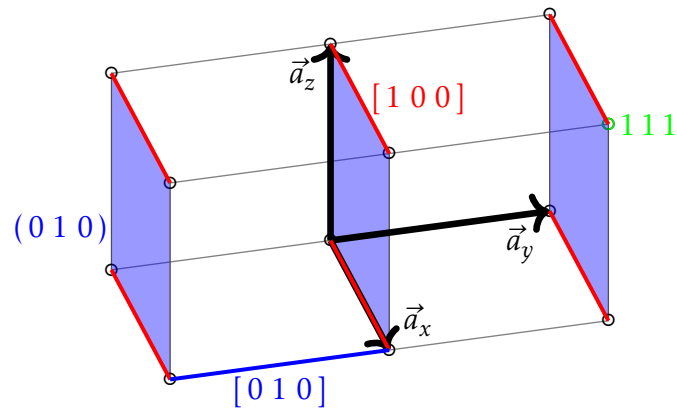


Figure B.1: Illustration of the notation in crystallography with the point 1 1 1 (green), the direction $[1\ 0\ 0]$ (red), and the planes $(0\ 1\ 0)$ (blue).

Considering a plane that is cut by the axes along \vec{a}_j at the points $o_j\vec{a}_j$, the triplet of fractions $\frac{1}{o_j}$ is expanded to the smallest possible integers, while their proportion is kept constant. The resulting integers are the Miller indices. If there is no penetration point, o_j is considered infinite, so the corresponding Miller index is 0. All parallel planes are expressed by the same Miller indices that are put in round brackets. Those planes are perpendicular to directions with the same indices, e.g., the $[1\ 0\ 0]$ directions are surface normals of the $(1\ 0\ 0)$ planes. The $(0\ 1\ 0)$ planes are marked in blue in Figure B.1 with the surface normal $[0\ 1\ 0]$ (blue line, only one marked for clarity) parallel to the y axis.

For planes as for directions, there is another notation that summarizes equivalent groups of planes. For planes, this is expressed with curly brackets $\{0\ 1\ 0\}$. In Figure B.1 the $\{0\ 1\ 0\}$ group contains all side faces of the cubes.

Bibliography

- [1] G. de Mestral. *Velvet type fabric and method of producing same*. U.S. Patent No. 2,717,437, 1955.
- [2] B. Dean and B. Bhushan. Shark-skin surfaces for fluid-drag reduction in turbulent flow: a review. *Philosophical Transactions of the Royal Society A*, 368(1929):4775, 2010.
- [3] B. Bhushan and Y. C. Jung. Natural and biomimetic artificial surfaces for superhydrophobicity, self-cleaning, low adhesion, and drag reduction. *Progress in Materials Science*, 56(1):1, 2011.
- [4] A. Diaz Lantada, S. Hengsbach, and K. Bade. Lotus-on-chip: computer-aided design and 3D direct laser writing of bioinspired surfaces for controlling the wettability of materials and devices. *Bioinspiration & Biomimetics*, 12(6):066004, 2017.
- [5] M. Large, editor. *Optical biomimetics: Materials and applications*, volume 48. Woodhead Publishing Ltd, Oxford, 2013.
- [6] M. Röhrig, M. Thiel, M. Worgull, and H. Hölscher. 3D direct laser writing of nano- and microstructured hierarchical gecko-mimicking surfaces. *Small*, 8(19):3009, 2012.
- [7] O. Tricinci, E. V. Eason, C. Filippeschi, A. Mondini, B. Mazzolai, N. M. Pugno, M. R. Cutkosky, F. Greco, and V. Mattoli. Approximating gecko setae via direct laser lithography. *Smart Materials and Structures*, 27(7):075009, 2018.
- [8] N. N. Shi, C.-C. Tsai, F. Camino, G. D. Bernard, N. Yu, and R. Wehner. Thermal physiology. Keeping cool: Enhanced optical reflection and radiative heat dissipation in Saharan silver ants. *Science*, 349(6245):298, 2015.
- [9] Q. Willot, P. Simonis, J.-P. Vigneron, and S. Aron. Total Internal Reflection Accounts for the Bright Color of the Saharan Silver Ant. *PLOS ONE*, 11(4):e0152325, 2016.
- [10] A. R. Parker and H. E. Townley. Biomimetics of photonic nanostructures. *Nature Nanotechnology*, 2(6):347, 2007.
- [11] C. Q. Cook and A. Amir. Theory of chirped photonic crystals in biological broadband reflectors. *Optica*, 3(12):1436, 2016.

BIBLIOGRAPHY

- [12] P. Vukusic, J. R. Sambles, C. R. Lawrence, and R. J. Wootton. Quantified interference and diffraction in single Morpho butterfly scales. *Proceedings of the Royal Society B: Biological Sciences*, 266(1427):1403, 1999.
- [13] X. Wu, F. L. Rodríguez-Gallegos, M.-C. Heep, B. Schwind, G. Li, H.-O. Fabritius, G. von Freymann, and J. Förstner. Polarization Conversion Effect in Biological and Synthetic Photonic Diamond Structures: 1800635. *Advanced Optical Materials*, 6(24):1800635, 2018. Picture licensed under license number 5050790608339 license date 2021-04-16.
- [14] E. Yablonovitch. Photonic band-gap crystals. *Journal of Physics: Condensed Matter*, 5(16):2443, 1993.
- [15] J. D. Joannopoulos, S. G. Johnson, J. N. Winn, and R. D. Meade. *Photonic Crystals: Molding the Flow of Light*. Princeton University Press, Princeton, 2nd edition, 2011.
- [16] K. Busch. *Photonic crystals: Advances in design, fabrication, and characterization*. Wiley-VCH, Weinheim and Cambridge, 2004.
- [17] M. Deubel, G. von Freymann, M. Wegener, S. Pereira, K. Busch, and C. M. Soukoulis. Direct laser writing of three-dimensional photonic-crystal templates for telecommunications. *Nature Materials*, 3(7):444, 2004.
- [18] M. D. Turner, M. Saba, Q. Zhang, B. P. Cumming, G. E. Schröder-Turk, and M. Gu. Miniature chiral beamsplitter based on gyroid photonic crystals. *Nature Photonics*, 7(10):801, 2013.
- [19] A. R. Parker, D. R. Mckenzie, and M.C.J. Large. Multilayer reflectors in animals using green and gold beetles as contrasting examples. *Journal of Experimental Biology*, 201(9):1307, 1998.
- [20] R. T. Lee and G. S. Smith. Detailed electromagnetic simulation for the structural color of butterfly wings. *Applied Optics*, 48(21):4177, 2009.
- [21] A. R. Parker. 515 million years of structural colour. *Journal of Optics A: Pure and Applied Optics*, 2(6):R15, 2000.
- [22] T. M. Jordan, J. C. Partridge, and N. W. Roberts. Disordered animal multilayer reflectors and the localization of light. *Journal of the Royal Society, Interface*, 11(101):20140948, 2014.
- [23] J. A. Bossard, L. Lin, and D. H. Werner. Evolving random fractal Cantor superlattices for the infrared using a genetic algorithm. *Journal of the Royal Society, Interface*, 13(114):20150975, 2016.
- [24] M. Burresti, L. Cortese, L. Pattelli, M. Kolle, P. Vukusic, D. S. Wiersma, U. Steiner, and S. Vignolini. Bright-white beetle scales optimise multiple scattering of light. *Scientific Reports*, 4:6075, 2014.

- [25] L. Cortese, L. Pattelli, F. Utel, S. Vignolini, M. Burrelli, and D. S. Wiersma. Anisotropic Light Transport in White Beetle Scales. *Advanced Optical Materials*, 3(10):1337, 2015.
- [26] P. Vukusic, B. Hallam, and J. Noyes. Brilliant whiteness in ultrathin beetle scales. *Science*, 315(5810):348, 2007.
- [27] B. D. Wilts, X. Sheng, M. Holler, A. Diaz, M. Guizar-Sicairos, J. Raabe, R. Hoppe, S.-H. Liu, R. Langford, O. D. Onelli, D. Chen, S. Torquato, U. Steiner, C. G. Schroer, S. Vignolini, and A. Sepe. Evolutionary-Optimized Photonic Network Structure in White Beetle Wing Scales. *Advanced Materials*, 30(19):1702057, 2018.
- [28] J. Syurik, G. Jacucci, O. D. Onelli, H. Hölscher, and S. Vignolini. Bio-inspired Highly Scattering Networks via Polymer Phase Separation. *Advanced Functional Materials*, 28(24):1706901, 2018.
- [29] S. Maruo, O. Nakamura, and S. Kawata. Three-dimensional microfabrication with two-photon-absorbed photopolymerization. *Optics Letters*, 22(2):132, 1997.
- [30] H.-B. Sun, S. Matsuo, and H. Misawa. Three-dimensional photonic crystal structures achieved with two-photon-absorption photopolymerization of resin. *Applied Physics Letters*, 74(6):786, 1999.
- [31] C. Barner-Kowollik, M. Bastemeyer, E. Blasco, M. Patrick, G. Delaittre, B. Richter, and M. Wegener. 3D Laser Micro- and Nano-Printing: Challenges for Chemistry. *Angewandte Chemie International Edition*, 2017.
- [32] I. Zergioti, A. Karaiskou, D. G. Papazoglou, C. Fotakis, M. Kapsetaki, and D. Kafetzopoulos. Femtosecond laser microprinting of biomaterials. *Applied Physics Letters*, 86(16):163902, 2005.
- [33] L. Fertier, H. Koleilat, M. Stemmelen, O. Giani, C. Joly-Duhamel, V. Lapinte, and J.-J. Robin. The use of renewable feedstock in UV-curable materials – A new age for polymers and green chemistry. *Progress in Polymer Science*, 38(6):932, 2013.
- [34] Gewerbemuseum. Cellulosehydrat : Materialarchiv. <http://www.materialarchiv.ch/app-tablet/#detail/38/cellulosehydrat->, 2008 (accessed 2019/08/30).
- [35] R. Auras, B. Harte, and S. Selke. An overview of polylactides as packaging materials. *Macromolecular Bioscience*, 4(9):835, 2004.
- [36] S. W. Pattinson and A. J. Hart. Additive Manufacturing of Cellulosic Materials with Robust Mechanics and Antimicrobial Functionality. *Advanced Materials Technologies*, 2(4):1600084, 2017.
- [37] K. Rajagopal and J. P. Schneider. Self-assembling peptides and proteins for nanotechnological applications. *Current Opinion in Structural Biology*, 14(4):480, 2004.
- [38] C. Niemeyer. Self-assembled nanostructures based on DNA: towards the development of nanobiotechnology. *Current Opinion in Chemical Biology*, 4(6):609, 2000.

BIBLIOGRAPHY

- [39] S. D. Wettig, C.-Z. Li, Y.-T. Long, H.-B. Kraatz, and J. S. Lee. M-DNA: a self-assembling molecular wire for nanoelectronics and biosensing. *Analytical Sciences*, 19(1):23, 2003.
- [40] A. D. Q. Li, W. Wang, and L.-Q. Wang. Folding versus self-assembling. *Chemistry - A European Journal*, 9(19):4594, 2003.
- [41] Y. Habibi, L. A. Lucia, and O. J. Rojas. Cellulose nanocrystals: chemistry, self-assembly, and applications. *Chemical Reviews*, 110(6):3479, 2010.
- [42] J. Schulz. *Charakterisierung des Reflexionsvermögens einer durch Silberameisen inspirierten Oberflächenstruktur*. Bachelor's thesis, Technische Universität Kaiserslautern, Kaiserslautern, 2016-09-30.
- [43] D. T. Meiers. *Entwicklung und Analyse eines grundlegenden Modells weißer Käferschuppen*. Diploma thesis, Technical University of Kaiserslautern, Kaiserslautern, 2018.
- [44] A. Koerfer. *Entwicklung und Charakterisierung eines auf Cellulose basierten Photolacks*. Diploma thesis, Technical University of Kaiserslautern, Kaiserslautern, 2019.
- [45] K. Egenolf. *Herstellung und Charakterisierung stark streuender bioinspirierter photonischer Strukturen*. Diploma thesis, Technical University of Kaiserslautern, Kaiserslautern, 2019.
- [46] T. J. Cui, R. Liu, and D. Smith. *Metamaterials: Theory, Design, and Applications*. Springer, Boston, 2010.
- [47] W. Demtröder. *Experimentalphysik 2: Elektrizität und Optik*, volume 2. Springer, Berlin, Heidelberg, 5th edition, 2009.
- [48] M. Born and E. Wolf. *Principles of optics: Electromagnetic theory of propagation, interference and diffraction of light*. Cambridge University Press, Cambridge, 7th edition, 1999.
- [49] A. Lipson, S. G. Lipson, and H. Lipson. *Optical physics*. Cambridge University Press, Cambridge and New York, 4th edition, 2011.
- [50] E. Hecht. *Optik*. De Gruyter Oldenbourg, München, 5th edition, 2009.
- [51] D. Meschede. *Gerthsen Physik*. Springer Spektrum, Berlin, Heidelberg, 25th edition, 2015.
- [52] S. Price and F. Gaillard. Coherent scattering: Radiology Reference Article, Radiopaedia.org. <https://radiopaedia.org/articles/coherent-scattering>, (accessed 2021/02/02).
- [53] Spektrum Verlag. Lexikon der Physik. <https://www.spektrum.de/lexikon/physik>, (accessed 2021/02/02).
- [54] H. Ibach and H. Lüth. *Solid-State Physics*. Springer, Berlin, Heidelberg, 2009.

- [55] W. Demtröder. *Experimentalphysik 3: Atome, Moleküle und Festkörper*. Springer, Berlin, Heidelberg, 4th edition, 2010.
- [56] E. Yablonovitch, T. J. Gmitter, and K. M. Leung. Photonic band structure: The face-centered-cubic case employing nonspherical atoms. *Physical Review Letters*, 67(17):2295, 1991.
- [57] J. G. Fleming and S. Y. Lin. Three-dimensional photonic crystal with a stop band from 1.35 to 1.95 microm. *Optics Letters*, 24(1):49, 1999.
- [58] V. Periyasamy and M. Pramanik. Advances in Monte Carlo Simulation for Light Propagation in Tissue. *IEEE Reviews in Biomedical Engineering*, 10:122, 2017.
- [59] S. E. Skipetrov and S. S. Chesnokov. Analysis, by the Monte Carlo method, of the validity of the diffusion approximation in a study of dynamic multiple scattering of light in randomly inhomogeneous media. *Quantum Electronics*, 28(8):733, 1998.
- [60] S. H. Lee, S. M. Han, and S. E. Han. Anisotropic diffusion in Cyphochilus white beetle scales. *APL Photonics*, 5(5):056103, 2020.
- [61] H. Nahrstedt. *Die Monte-Carlo-Methode: Beispiele unter Excel VBA*. Springer Vieweg, Wiesbaden, 2015.
- [62] K. Yee. Numerical solution of initial boundary value problems involving maxwell's equations in isotropic media. *IEEE Transactions on Antennas and Propagation*, 14(3):302, 1966.
- [63] D. M. Sullivan. *Electromagnetic simulation using the FDTD method*. IEEE Press Wiley-Interscience and IEEE Xplore, New York and Hoboken, NJ and Piscataway, New Jersey, 2000.
- [64] A. Taflove and S. C. Hagness. *Computational electrodynamics: The finite-difference time-domain method*. Artech House, Boston, 3rd edition, 2010.
- [65] D. M. Sullivan. Nonlinear FDTD formulations using Z transforms. *IEEE Transactions on Microwave Theory and Techniques*, 43(3):676, 1995.
- [66] R. M. Joseph and A. Taflove. FDTD Maxwell's equations models for nonlinear electrodynamics and optics. *IEEE Transactions on Antennas and Propagation*, 45(3):364, 1997.
- [67] A. Taflove and M. E. Brodwin. Numerical Solution of Steady-State Electromagnetic Scattering Problems Using the Time-Dependent Maxwell's Equations. *IEEE Transactions on Microwave Theory and Techniques*, 23(8):623, 1975.
- [68] K. L. Shlager and J. B. Schneider. A selective survey of the finite-difference time-domain literature. *IEEE Antennas and Propagation Magazine*, 37(4):39, 1995.
- [69] J.-P. Berenger. A perfectly matched layer for the absorption of electromagnetic waves. *Journal of Computational Physics*, 114(2):185, 1994.

BIBLIOGRAPHY

- [70] R. C. Rumpf. Computational Electromagnetics (CEM): Lecture 8 (CEM) - Perfectly Matched Layer. <https://www.youtube.com/watch?v=FM5dnpHSpz8&t=1486s>, 2013 (accessed 2019/04/17).
- [71] S. Zhang, D. M. Marini, W. Hwang, and S. Santoso. Design of nanostructured biological materials through self-assembly of peptides and proteins. *Current Opinion in Chemical Biology*, 6(6):865, 2002.
- [72] Q. Wang, J. Sun, Q. Yao, C. Ji, J. Liu, and Q. Zhu. 3D printing with cellulose materials. *Cellulose*, 25(8):4275, 2018.
- [73] J. K. Hohmann, M. Renner, E. H. Waller, and G. von Freymann. Three-Dimensional μ -Printing: An Enabling Technology. *Advanced Optical Materials*, 3(11):1488, 2015.
- [74] P. Mueller, M. Thiel, and M. Wegener. 3D direct laser writing using a 405 nm diode laser. *Optics Letters*, 39(24):6847, 2014.
- [75] M. Thiel, J. Fischer, G. von Freymann, and M. Wegener. Direct laser writing of three-dimensional submicron structures using a continuous-wave laser at 532 nm. *Applied Physics Letters*, 97(22):221102, 2010.
- [76] E. H. Waller, M. Renner, and G. von Freymann. Active aberration- and point-spread-function control in direct laser writing. *Optics Express*, 20(22):24949, 2012.
- [77] E. H. Waller and G. von Freymann. Independent spatial intensity, phase and polarization distributions. *Optics Express*, 21(23):28167, 2013.
- [78] C. Jörg. *Erste Schritte in Richtung optischer topologischer Isolatoren durch direktes Laserschreiben*. Diploma thesis, Technical University of Kaiserslautern, Kaiserslautern, 2015.
- [79] M. Thiel. *Design, Fabrication, and Characterization of Three-Dimensional Chiral Photonic Crystals*. Ph.D. thesis, Institute of Technology, Karlsruhe, 2010-02-05.
- [80] Nanoscribe GmbH. Photonic Professional (GT): User Manual, 2017.
- [81] A. Grushina. Direct-write grayscale lithography. *Advanced Optical Technologies*, 8(3-4):163, 2019.
- [82] J. Fischer and M. Wegener. Three-dimensional optical laser lithography beyond the diffraction limit. *Laser & Photonics Reviews*, 7(1):22, 2013.
- [83] J. Fischer. *Three-dimensional optical lithography beyond the diffraction limit*. Ph.D. thesis, Institute of Technology, Karlsruhe, 2012.
- [84] M. Göppert-Mayer. Über Elementarakte mit zwei Quantensprüngen. *Annalen der Physik*, 401(3):273, 1931.
- [85] W. Kaiser and C. G. B. Garrett. Two-Photon Excitation in Ca F₂ : Eu²⁺. *Physical Review Letters*, 7(6):229, 1961.

- [86] D. L. Andrews, editor. *Fundamentals of photonics and physics*, volume 1. Wiley, Hoboken, NJ, 2015.
- [87] K. D. Belfield, Y. Liu, R. A. Negres, M. Fan, G. Pan, D. J. Hagan, and F. E. Hernandez. Two-Photon Photochromism of an Organic Material for Holographic Recording. *Chemistry of Materials*, 14(9):3663, 2002.
- [88] R. W. Boyd. *Nonlinear optics*. Academic Press, Amsterdam, 3th edition, 2008.
- [89] P. Chandra Jha, Y. Wang, and H. Agren. Two-photon absorption cross-sections of reference dyes: a critical examination. *ChemPhysChem*, 9(1):111, 2008.
- [90] E. H. Waller. *Structured light in direct laser writing*. Ph.D. thesis, Technical University of Kaiserslautern, Kaiserslautern, 2015.
- [91] W. M. McClain. Two-photon molecular spectroscopy. *Accounts of Chemical Research*, 7(5):129, 1974.
- [92] G. Hohlneicher and B. Dick. Two-photon spectroscopy of dipole-forbidden transitions. II. Calculation of two-photon cross sections by the CNDO-CI method. *The Journal of Chemical Physics*, 70(12):5427, 1979.
- [93] S. R. Marder and Lee K.-S., editors. *Photoresponsive polymers I*, volume 213. Springer, Berlin, Heidelberg, 2008.
- [94] K. J. Schafer, J. M. Hales, M. Balu, K. D. Belfield, E. W. van Stryland, and D. J. Hagan. Two-photon absorption cross-sections of common photoinitiators. *Journal of Photochemistry and Photobiology A: Chemistry*, 162(2-3):497, 2004.
- [95] E. H. Waller and G. von Freymann. From photoinduced electron transfer to 3D metal microstructures via direct laser writing. *Nanophotonics*, 7(7):1259, 2018.
- [96] E. H. Waller, S. Dix, J. Gutsche, A. Widera, and G. von Freymann. Functional Metallic Microcomponents via Liquid-Phase Multiphoton Direct Laser Writing: A Review. *Micromachines*, 10(12), 2019.
- [97] C. Decker. Photoinitiated crosslinking polymerisation. *Progress in Polymer Science*, 21(4):593, 1996.
- [98] F. R. Wight. Oxygen inhibition of acrylic photopolymerization. *Journal of Polymer Science: Polymer Letters Edition*, 16(3):121, 1978.
- [99] Y. Yagci, S. Jockusch, and N. J. Turro. Photoinitiated Polymerization: Advances, Challenges, and Opportunities. *Macromolecules*, 43(15):6245, 2010.
- [100] K. Schwarzschild. On the Deviations from the Law of Reciprocity for Bromide of Silver Gelatine. *The Astrophysical Journal*, 11:89, 1900.
- [101] E. H. Waller and G. von Freymann. Spatio-Temporal Proximity Characteristics in 3D μ -Printing via Multi-Photon Absorption. *Polymers*, 8(8):297, 2016.

BIBLIOGRAPHY

- [102] S. W. Hell and J. Wichmann. Breaking the diffraction resolution limit by stimulated emission: stimulated-emission-depletion fluorescence microscopy. *Optics Letters*, 19(11):780, 1994.
- [103] J. Fischer, G. von Freymann, and M. Wegener. The materials challenge in diffraction-unlimited direct-laser-writing optical lithography. *Advanced Materials*, 22(32):3578, 2010.
- [104] J. Hering. *Von der STED inspirierten Zwei-Photonen Laserlithographie zur industriellen Metrologie*. Ph.D. thesis, Technical University of Kaiserslautern, Kaiserslautern, 2020-02-18.
- [105] J. Hering, E. H. Waller, and G. von Freymann. Automated aberration correction of arbitrary laser modes in high numerical aperture systems. *Optics Express*, 24(25):28500, 2016.
- [106] L. Li and J. T. Fourkas. Multiphoton polymerization. *Materials Today*, 10(6):30, 2007.
- [107] D. Klemm, B. Heublein, H.-P. Fink, and A. Bohn. Cellulose: fascinating biopolymer and sustainable raw material. *Angewandte Chemie International Edition*, 44(22):3358, 2005.
- [108] P. Anastas and N. E. Green chemistry: principles and practice. *Chemical Society Reviews*, 39(1):301, 2010.
- [109] A. K. Mohanty, M. Misra, and G. Hinrichsen. Biofibres, biodegradable polymers and biocomposites: An overview. *Macromolecular Materials and Engineering*, 276-277(1):1, 2000.
- [110] P. Pospiech. Kunststoffe: Teil 4: Prothesenkunststoffe: Technik | ZTM-aktuell.de. https://www.ztm-aktuell.de/technik/werkstoffe/story/kunststoffe--teil-4-prothesenkunststoffe__8011.html, (accessed 2019/10/10).
- [111] W. M. Cheng, G. A. Miller, J. A. Manson, R. W. Hertzberg, and L. H. Sperling. Mechanical behaviour of poly(methyl methacrylate). *Journal of Materials Science*, 25(4):1917, 1990.
- [112] R. A. Jacobson, J. A. Wunderlich, and W. N. Lipscomb. The crystal and molecular structure of cellobiose. *Acta Crystallographica*, 14(6):598, 1961.
- [113] C. E. Mortimer and U. Müller. *Chemie: Das Basiswissen der Chemie*. Thieme, Stuttgart, 10th edition, 2010.
- [114] M. Rothhammer. *in preparation*. Ph.D. thesis, Technical University of Munich, Straubing.
- [115] M. Rothhammer, M.-C. Heep, G. von Freymann, and C. Zollfrank. Enabling direct laser writing of cellulose-based submicron architectures. *Cellulose*, 25(10):6031, 2018.

- [116] M. Rothhammer. Cellulose derivatives, their properties and synthesis, personal communication, 2018-2021.
- [117] Y. Teramoto. Functional thermoplastic materials from derivatives of cellulose and related structural polysaccharides. *Molecules*, 20(4):5487, 2015.
- [118] H. Staudinger. Viscosity investigations for the examination of the constitution of natural products of high molecular weight and of rubber and cellulose. *Transactions of the Faraday Society*, 29(140):18, 1933.
- [119] O. Nuyken, H. Samarian, and I. Wurdack. Viskosimetrie. <http://www.chemgapedia.de/vsengine/vlu/vsc/de/ch/9/mac/charakterisierung/d3/viskos/viskosmol.vlu.html>, (accessed 2020/08/07).
- [120] Thermo Fisher Scientific Inc. Thermo Scientific Evolution 201 & 220 UV-Visible Spectrophotometers. <https://assets.thermofisher.com/TFS-Assets/MSD/brochures/BR51944-evolution-201-220.pdf>, 2019 (accessed 2020/07/26).
- [121] M. Sheik-Bahae, A. A. Said, and E. W. van Stryland. High-sensitivity, single-beam $n(2)$ measurements. *Optics Letters*, 14(17):955, 1989.
- [122] M. Sheik-Bahae, A. A. Said, T.-H. Wei, D. J. Hagan, and E. W. van Stryland. Sensitive measurement of optical nonlinearities using a single beam. *IEEE Journal of Quantum Electronics*, 26(4):760, 1990.
- [123] A. Eibel, D. E. Fast, and G. Gescheidt. Choosing the ideal photoinitiator for free radical photopolymerizations: predictions based on simulations using established data. *Polymer Chemistry*, 9(41):5107, 2018.
- [124] J. S. Oakdale, J. Ye, W. L. Smith, and J. Biener. Post-print UV curing method for improving the mechanical properties of prototypes derived from two-photon lithography. *Optics Express*, 24(24):27077, 2016.
- [125] MOLBASE. Encyclopedia. <http://www.molbase.com>, (accessed 2020/09/12).
- [126] NIST. NIST Chemistry WebBook, SRD69. <https://webbook.nist.gov/chemistry/>, 2018 (accessed 2020/09/06).
- [127] J. Fischer, J. B. Mueller, J. Kaschke, T. J. A. Wolf, A.-N. Unterreiner, and M. Wegener. Three-dimensional multi-photon direct laser writing with variable repetition rate. *Optics Express*, 21(22):26244, 2013.
- [128] S. C. Ligon, R. Liska, J. Stampfl, M. Gurr, and R. Mülhaupt. Polymers for 3D Printing and Customized Additive Manufacturing. *Chemical Reviews*, 117(15):10212, 2017.
- [129] T. J. A. Wolf. *Ultrafast photophysics and photochemistry of radical precursors in solution*. PhD thesis, Institute of Technology, Karlsruhe, 2012.
- [130] R. Houbertz, G. Domann, J. Schulz, B. Olsowski, L. Fröhlich, and W.-S. Kim. Impact of photoinitiators on the photopolymerization and the optical properties of inorganic-organic hybrid polymers. *Applied Physics Letters*, 84(7):1105, 2004.

BIBLIOGRAPHY

- [131] M. Malinauskas, A. Zukauskas, G. Bickaускаite, R. Gadonas, and S. Juodkazis. Mechanisms of three-dimensional structuring of photo-polymers by tightly focussed femtosecond laser pulses. *Optics Express*, 18(10):10209, 2010.
- [132] M. Malinauskas, M. Farsari, A. Piskarskas, and S. Juodkazis. Ultrafast laser nanostructuring of photopolymers: A decade of advances. *Physics Reports*, 533(1):1, 2013.
- [133] K. Obata, A. El-Tamer, L. Koch, U. Hinze, and B. N. Chichkov. High-aspect 3D two-photon polymerization structuring with widened objective working range (WOW-2PP). *Light: Science & Applications*, 2(12):e116, 2013.
- [134] C. M. B. Ho, A. Mishra, K. Hu, J. An, Y.-J. Kim, and Y.-J. Yoon. Femtosecond-Laser-Based 3D Printing for Tissue Engineering and Cell Biology Applications. *ACS Biomaterials Science & Engineering*, 3(10):2198, 2017.
- [135] L. Pooza, M. Gottschaldt, E. Markweg, N. Hauptmann, G. Hildebrand, D. Pretzel, M. Hartlieb, C. Reichardt, J. Kübel, U. S. Schubert, O. Mollenhauer, B. Dietzek, and K. Liefelth. Optimized Photoinitiator for Fast Two-Photon Absorption Polymerization of Polyester-Macromers for Tissue Engineering. *Advanced Engineering Materials*, 19(3):1600686, 2017.
- [136] F. Zhang, Q. Hu, A. Castañón, Y. He, Y. Liu, B. T. Paul, C. J. Tuck, R.J.M. Hague, and R. D. Wildman. Multi-branched benzylidene ketone based photoinitiators for multiphoton fabrication. *Additive Manufacturing*, 16:206, 2017.
- [137] N. Shirakbari, S. Ghaffarian, and M. Mohseni. Fabrication and simulation of inverse poly(ferrocenylmethylvinylsilane)/silica opal structures and their optical properties. *Journal of Composite Materials*, 2016.
- [138] R. Reeves, A. Ribeiro, L. Lombardo, R. Boyer, and J. B. Leach. Synthesis and Characterization of Carboxymethylcellulose-Methacrylate Hydrogel Cell Scaffolds. *Polymers*, 2(3):252, 2010.
- [139] R. F. Pereira and P. J. Bártolo. 3D bioprinting of photocrosslinkable hydrogel constructs. *Journal of Applied Polymer Science*, 132(48):42458, 2015.
- [140] J. Stampfl, R. Liska, and A. Ovsianikov, editors. *Multiphoton lithography: Techniques, materials and applications*. Wiley-VCH, Weinheim, 2017.
- [141] S. Li, H. S. Chung, A. Simakova, Z. Wang, S. Park, L. Fu, D. Cohen-Karni, S. Averick, and K. Matyjaszewski. Biocompatible Polymeric Analogues of DMSO Prepared by Atom Transfer Radical Polymerization. *Biomacromolecules*, 18(2):475, 2017.
- [142] C. A. Yeates, H. M. Krieg, and J. C. Breytenbach. Hydroxypropyl- β -cyclodextrin induced complexation for the biocatalytic resolution of a poorly soluble epoxide. *Enzyme and Microbial Technology*, 40(2):228, 2007.
- [143] Sicherheitsdatenblatt: Aceton $\geq 99,5\%$, zur Synthese: gemäß Verordnung (EG) Nr. 1907/2006 (REACH), geändert mit 2015/830/EU, 2018/06/28.

- [144] F. Mayer, S. Richter, J. Westhauser, E. Blasco, C. Barner-Kowollik, and M. Wegener. Multimaterial 3D laser microprinting using an integrated microfluidic system. *Science Advances*, 5(2):eaau9160, 2019.
- [145] Sicherheitsdatenblatt: Dimethylsulfoxid $\geq 99,5$ %, BioScience-Grade, für die Molekularbiologie: gemäß Verordnung (EG) Nr. 1907/2006 (REACH), geändert mit 2015/830/EU, 2018/06/28.
- [146] L. Yang, A. Münchinger, M. Kadic, V. Hahn, F. Mayer, E. Blasco, C. Barner-Kowollik, and M. Wegener. On the Schwarzschild Effect in 3D Two-Photon Laser Lithography. *Advanced Optical Materials*, 7(22):1901040, 2019.
- [147] J. B. Mueller. *Exploring the Mechanisms of Three-Dimensional Direct Laser Writing by Multi-Photon Polymerization*. Ph.D. thesis, Institute of Technology, Karlsruhe, 2015-05-22.
- [148] A. Wolfberger, A. Petritz, A. Fian, J. Herka, V. Schmidt, B. Stadlober, R. Kargl, S. Spirk, and T. Griesser. Photolithographic patterning of cellulose: a versatile dual-tone photoresist for advanced applications. *Cellulose*, 22(1):717, 2015.
- [149] Nanosurf AG. Topography and surface roughness measurements. <https://www.nanosurf.com/en/support/afm-modes-overview/topography-and-surface-roughness-measurements>, (accessed 2021/04/04).
- [150] T. Gissibl, S. Wagner, J. Sykora, M. Schmid, and H. Giessen. Refractive index measurements of photo-resists for three-dimensional direct laser writing. *Optical Materials Express*, 7(7):2293, 2017.
- [151] J. T. Woollney. Refractive Index of Soybean Leaf Cell Walls. *Plant Physiology*, 55(2):172, 1975.
- [152] J. K. Hohmann and G. von Freymann. Influence of Direct Laser Written 3D Topographies on Proliferation and Differentiation of Osteoblast-Like Cells: Towards Improved Implant Surfaces. *Advanced Functional Materials*, 24(42):6573, 2014.
- [153] J. W. S. Rayleigh. The Iridescent Colours of Birds and Insects. *Proceedings of the Royal Society A: Mathematical, Physical and Engineering Sciences*, 128(808):624, 1930.
- [154] H. L. Leertouwer, B. D. Wilts, and D. G. Stavenga. Refractive index and dispersion of butterfly chitin and bird keratin measured by polarizing interference microscopy. *Optics Express*, 19(24):24061, 2011.
- [155] D. E. Azofeifa, H. J. Arguedas, and W. E. Vargas. Optical properties of chitin and chitosan biopolymers with application to structural color analysis. *Optical Materials*, 35(2):175, 2012.
- [156] N. Berezina. Production and application of chitin. *Physical Sciences Reviews*, 1(9):4393, 2016.

BIBLIOGRAPHY

- [157] D. T. Meiers, M.-C. Heep, and G. von Freymann. Invited Article: Bragg stacks with tailored disorder create brilliant whiteness. *APL Photonics*, 3(10):100802, 2018.
- [158] J. A. Gritzner and R. F. Peel. Sahara. <https://www.britannica.com/place/Sahara-desert-Africa>, 1999 (accessed 2021/05/13).
- [159] N. N. Shi, C.-C. Tsai, F. Camino, G. D. Bernard, R. Wehner, and N. Yu. Radiative Cooling Nano-Photonic Structures Discovered in Saharan Silver Ants and Related Biomimetic Metasurfaces. In *2016 Conference on Lasers and Electro-Optics (CLEO)*, page FTh3B.1, Piscataway, NJ, 2016. IEEE.
- [160] S. Shang, Y. Wang, K.-l. Chiu, and S. Jiang. Solar heat shielding performance of potassium titanate whisker coated polypropylene fabric based on a bionic method. *Composites Part B: Engineering*, 177:107408, 2019.
- [161] S. Kinoshita, S. Yoshioka, and J. Miyazaki. Physics of structural colors. *Reports on Progress in Physics*, 71(7):076401, 2008.
- [162] C. W. Mason. Structural Colors in Insects. II. *The Journal of Physical Chemistry*, 31(3):321, 1926.
- [163] S. Kinoshita, S. Yoshioka, and K. Kawagoe. Mechanisms of structural colour in the Morpho butterfly: cooperation of regularity and irregularity in an iridescent scale. *Proceedings of the Royal Society B: Biological Sciences*, 269(1499):1417, 2002.
- [164] K. Watanabe, T. Hoshino, K. Kanda, Y. Haruyama, and S. Matsui. Brilliant Blue Observation from a Morpho -Butterfly-Scale Quasi-Structure. *Japanese Journal of Applied Physics*, 44(1):L48, 2005.
- [165] F. Liu, Y. Liu, L. Huang, X. Hu, B. Dong, W. Shi, Y. Xie, and X. Ye. Replication of homologous optical and hydrophobic features by templating wings of butterflies Morpho menelaus. *Optics Communications*, 284(9):2376, 2011.
- [166] G. Zyla, A. Kovalev, M. Grafen, E. L. Gurevich, C. Esen, A. Ostendorf, and S. Gorb. Generation of bioinspired structural colors via two-photon polymerization. *Scientific Reports*, 7(1):17622, 2017.
- [167] V. Kratochvil. Blue Morpho-Schmetterling: Kostenloses Stock Bild - Public Domain Pictures. <https://www.publicdomainpictures.net/de/view-image.php?image=7275&picture=blue-morpho-schmetterling>, 2020 (accessed 2020/01/21).
- [168] R. A. Potyrailo, R. K. Bonam, J. G. Hartley, T. A. Starkey, P. Vukusic, M. Vasudev, T. Bunning, R. R. Naik, Z. Tang, M. A. Palacios, M. Larsen, L. A. Le Tarte, J. C. Grande, S. Zhong, and T. Deng. Towards outperforming conventional sensor arrays with fabricated individual photonic vapour sensors inspired by morpho butterflies. *Nature Communications*, 6:7959, 2015. Picture licensed under CC by 4.0 see <https://creativecommons.org/licenses/by/4.0/>.

- [169] T. F. Anderson and A. G. Richards. An Electron Microscope Study of Some Structural Colors of Insects. *Journal of Applied Physics*, 13(12):748, 1942.
- [170] R. H. Siddique, S. Diewald, J. Leuthold, and H. Hölscher. Theoretical and experimental analysis of the structural pattern responsible for the iridescence of Morpho butterflies. *Optics Express*, 21(12):14351, 2013.
- [171] S. Yoshioka and S. Kinoshita. Wavelength-selective and anisotropic light-diffusing scale on the wing of the Morpho butterfly. *Proceedings of the Royal Society B: Biological Sciences*, 271(1539):581, 2004.
- [172] M. Srinivasarao. Nano-Optics in the Biological World: Beetles, Butterflies, Birds, and Moths. *Chemical Reviews*, 99(7):1935, 1999.
- [173] Y. Chen, G. Dai, H. Li, H. Xia, S. Ma, J. Gu, and D. Zhang. Influence of disorders on the optical properties of butterfly wing: Analysis with a finite-difference time-domain method. *The European Physical Journal B*, 86(11), 2013.
- [174] J. J. Morrone. The Neotropical Weevil Genus *Entimus* (Coleoptera: Curculionidae: Entiminae): Cladistics, Biogeography, and Modes of Speciation. *The Coleopterists Bulletin*, 56(4):501, 2002.
- [175] B. D. Wilts, K. Michielsen, J. Kuipers, H. de Raedt, and D. G. Stavenga. Brilliant camouflage: photonic crystals in the diamond weevil, *Entimus imperialis*. *Proceedings of the Royal Society B: Biological Sciences*, 279(1738):2524, 2012.
- [176] O. Deparis and J. P. Vigneron. Modeling the photonic response of biological nanostructures using the concept of stratified medium: The case of a natural three-dimensional photonic crystal. *Materials Science and Engineering: B*, 169(1-3):12, 2010.
- [177] S. M. Luke, B. T. Hallam, and P. Vukusic. Structural optimization for broadband scattering in several ultra-thin white beetle scales. *Applied Optics*, 49(22):4246, 2010.
- [178] J. Syurik, R. H. Siddique, A. Dollmann, G. Gomard, M. Schneider, M. Worgull, G. Wiegand, and H. Hölscher. Bio-inspired, large scale, highly-scattering films for nanoparticle-alternative white surfaces. *Scientific Reports*, 7:46637, 2017.
- [179] S. L. Burg, A. Washington, D. M. Coles, A. Bianco, D. McLoughlin, O. O. Mykhaylyk, J. Villanova, A. J. C. Dennison, C. J. Hill, P. Vukusic, S. Doak, S. J. Martin, M. Hutchings, S. R. Parnell, C. Vasilev, N. Clarke, A. J. Ryan, W. Furnass, M. Croucher, R. M. Dalgliesh, S. Prevost, R. Dattani, A. Parker, R. A. L. Jones, J. P. A. Fairclough, and A. J. Parnell. Liquid-liquid phase separation morphologies in ultra-white beetle scales and a synthetic equivalent. *Communications Chemistry*, 2(1):383, 2019.
- [180] T. Smith and J. Guild. The C.I.E. colorimetric standards and their use. *Transactions of the Optical Society*, 33(3):73, 1931.

BIBLIOGRAPHY

- [181] R. Biswas, M. M. Sigalas, G. Subramania, C. M. Soukoulis, and K.-M. Ho. Photonic band gaps of porous solids. *Physical Review B*, 61(7):4549, 2000.
- [182] S. Zarei, M. Shahabadi, and A. Zarei. Demonstration of wide higher-order stopbands in two-dimensional photonic crystals using a real-valued genetic algorithm. In *2008 IEEE Photonics Global Singapore*, page 1. IEEE, 2008.
- [183] H.-J. Korsch. *Mathematische Ergänzungen zur Einführung in die Physik*. Binomi, Barsinghausen, 4th edition, 2007.
- [184] K. Burg, H. Haf, and F. Wille. *Vektoranalysis: Höhere Mathematik für Ingenieure, Naturwissenschaftler und Mathematiker*. B.G. Teubner Verlag / GWV Fachverlage GmbH Weisbaden, Wiesbaden, 2006.
- [185] G. von Freymann. *Applied Physics III*. Lecture notes, Technical University Kaiserslautern, Kaiserslautern, 2017.
- [186] W. Borchardt-Ott. *Kristallographie: Eine Einführung für Naturwissenschaftler ; mit 47 Tabellen*. Springer, Berlin, Heidelberg, 7th edition, 2009.
- [187] H. Föll. *Einführung in die Materialwissenschaft I*. Lecture notes, Christian-Albrecht-University, Kiel, 2019.

Publications

Parts of this thesis have been published in scientific journals and presented on international conferences.

Publications in scientific journals (peer-reviewed):

- [115] M. Rothhammer*, M.-C. Heep*, G. von Freymann, and C. Zollfrank. Enabling direct laser writing of cellulose-based submicron architectures. *Cellulose*, **25** (10), 6031-6039, 2018.
- [157] D. T. Meiers*, M.-C. Heep*, and G. von Freymann. Invited Article. Bragg stacks with tailored disorder create brilliant whiteness. *APL Photonics* **3** (10), 100802, 2018.
- [13] X. Wu*, F. Rodríguez-Gallegos, M.-C. Heep, B. Schwind, G. Li, H.-O. Fabritius, G. von Freymann, J. Förstner. Polarization Conversion Effect in Biological and Synthetic Photonic Diamond Structures. *Advanced Optical Materials* **6** (24), 1800635, 2018.

Conference contributions (as speaker/presenter):

Talks

- M.-C. Heep, D.T. Meiers, and G. von Freymann: Mimicking the optics of white beetles. SPIE Photonics West 2019, San Francisco, CA, USA
- M.-C. Heep, A. Koerfer, M. Rothhammer, C. Zollfrank, and G. von Freymann: Capabilities of photoresists based on polysaccharides for direct laser writing. DPG spring meeting 2019, Regensburg, Germany
- M.-C. Angermann, D. T. Meiers, and G. von Freymann: A simple model mimicking the white beetles. EOS Topical Meeting on Waves in Complex Photonics Media 2018, Anacapri, Italy
- M.-C. Angermann, M. Rothhammer, C. Zollfrank, and G. von Freymann: Cellulose-based photoresist for Two-Photon-Lithography. DPG spring meeting 2018, Berlin, Germany

*Leading author

Publications

- M.-C. Angermann, M. Rothhammer, C. Zollfrank, and G. von Freymann: Towards a cellulose-based photoresist. SPIE Photonics West 2018, San Francisco, CA, USA

Posters

- M.-C. Angermann, M. Rothhammer, C. Zollfrank, and G. von Freymann: Towards a structural blueprint of strongly scattering networks in beetle scales. Spring School of SPP 1839 2017, Karlsruhe, Germany
- M.-C. Angermann and G. von Freymann: Biomimetic imitation of strongly scattering beetle scales. DPG spring meeting 2017, Dresden, Germany
- M.-C. Angermann and G. von Freymann: Biomimetic imitation of strongly scattering beetle scales. 634. WE-Heraeus-Seminar: Merging Micro- and Nano-Optics 2017, Bad Honnef, Germany

Curriculum vitae

Education and professional experience

Since 01/2016	Research assistant and Ph.D. student in the physics department at Technical University of Kaiserslautern in the group for optical technologies and photonics
12/2019-01/2021	Maternity and subsequent parental leave
09/2015-12/2015	Research assistant in the physics department at Technical University of Kaiserslautern
10/2009-08/2015	Academic studies in physics with a specialization in technical physics with a diploma degree from Technical University of Kaiserslautern
11/2013-03/2014	Internship at Robert Bosch GmbH in Bamberg in department for laser material processing
10/2013	Internship at Harmonic Drive AG in Limburg a.d. Lahn
06/2009	General qualification for university entrance

Erklärung

Hiermit versichere ich, Marie-Christin Heep, dass ich die vorliegende Dissertation selbstständig und ohne unzulässige fremde Hilfe verfasst habe. Sämtliche verwendeten Quellen und Hilfsmittel sind angegeben. Wörtlich oder sinngemäß übernommene Gedankengänge sowie ganz oder annähernd übernommene Grafiken und Tabellen sind durch entsprechende Angaben kenntlich gemacht.

Außerdem versichere ich, dass die vorgelegte digitale mit der analogen Version der Dissertation übereinstimmt und dass diese Abhandlung weder in dieser noch in ähnlicher Form als Promotionsleistung vorgelegt wurde.

Kaiserslautern, 12. Oktober 2021

Marie-Christin Heep

Thanks to all of you

At the very end of my work, I want to express my thanks to those wonderful people, who supported me and accompanied me. There is no chance to name all of them here in the way they deserve it.

Let me start with the person, who offered me the chance to work on such a great and inspiring topic: my thesis supervisor Prof. Dr. Georg von Freymann. Thanks for believing in my ability to cope with a completely new topic and for all the productive feedback.

Furthermore, I thank Prof. Dr. Cordt Zollfrank for co-refereeing my thesis and for the productive cooperation in the priority program “Tailored disorder”.

This leads me to my fellow PhD students and colleagues. I want to thank Maximilian Rothhammer from the group in Straubing as well as my colleagues in the group of “Optische Technologien und Photonik” at the Technical University of Kaiserslautern. Special thanks go to the former students which did their theses in the course of my work and whose results made their way into my work, too.

Thanks, to all the proofreaders! Thank you, for your feedback on all the small and big issues of my work.

I also have to thank the team of the Nanostructuring Center for their support and especially Thomas Löber for all the FIB cuts.

Thank you to my family and friends, too: for your patience and your understanding and for the motivation you gave me. Three persons, I have to name here, because they motivated me more than all others and they kept me from giving up:

Thank you Christina, for your motivation and your expertise on how to survive my PhD.

Thank you Steffen, for taking care of me and for supporting me.

And Lena, thank you, for cheering me up when I needed it.